FACULTY OF SCIENCES

CHARACTERISATION OF ANTARCTIC UNMELTED MICROMETEORITES USING SYNCHROTRON-BASED X-RAY ANALYSIS

Flore Van Maldeghem
Student number: 01302775

Promotor: Dr. Steven Goderis
Copromotor: Prof. dr. Philippe Claeys

Jury: Prof. dr. Veerle Cnudde, Prof. dr. Laszlo Vince

Master's dissertation submitted in partial fulfilment of the requirements for the degree of master in geology

Academic year: 2017-2018

GHENT UNIVERSITY

KU LEUVEN

Acknowledgements

This master dissertation is the result of five years of studying, one year of hard work, a lifetime of scientific interest and the guidance, help and support of many people. Here, I would like to take a moment to thank all these wonderful human beings.

First of all, I would like to say thank you to dr. Steven Goderis and Prof. dr. Philippe Claeys from the Vrije Universiteit Brussel for being my promotors and guiding me through this year full of new knowledge and helping me find answers to all my questions. You showed me the way in the scientific community through unique opportunities like the project at the ESRF in Grenoble and the poster presentation at the EGU in Vienna. Thank you to Prof. dr. Luigi Folco for providing the particles from the TAM collection. Also, a special thanks to Bastien Soens for reading (and re-reading) my drafts and help to improve this project. The same goes for Matthias Van Ginneken. Your input was very helpful. I also have to thank Brecht Laforce and Ella De Pauw for the chemical knowledge and joining us at the ESRF, where we were assisted by our great beamline scientist Jussi-Petteri Suuronen and frankly, it was a good thing he was around. And thank you to the whole AMGC group, for accepting me and treating me like one of your own.

I would also like to express my gratitude towards my parents, who kindly financed my studies and were also always interested in everthing I did and learned. They were always there behind the scenes and put up with my nonsense during exams and deadlines. You were a great support in every possible way. And of course, my little brother, who was more than once my punch ball in times of stress. I would not have been where I am today without all of your help.

A big thank you, for my geological friends, for all the shared moments of laughter, entertaining field trips and decent geology jokes. For my Erasmus friends, for keeping in touch and providing an escape from all the work every once in a while. For my scout friends, for reminding me there is more in the world than just rocks. Thank you to my boyfriend, for tolerating the many hours of absence and listening to my complains. I promise 'working on my dissertation' will no longer be an excuse.

There is much more behind one dissertation than you might think and I couldn't have done it without all of you.

The Story of my Research

My greatest interest was (and still is) everything that has to do with outer space, planets and stars. Ever since I was a kid, I've been intrigued by the endlessness of space and for a while I thought about doing a bachelor in physics and astronomy. However, since theoretical approaches are not my specialty, I was recommended to start with the bachelor in geology. So, in September 2013 I met my fellow geology students on the introduction day at S8, our habitat for the next five years. For a while, I had to store my passion for the extra-terrestrial away, because these topics are not treated very extensively in bachelor courses. I was already preparing myself to explore another field until the dissertation topics came online. One of the first items on the list was 'working on Antarctic micrometeorites' and I was sold. I barely looked at the other options and mailed Philippe. My enthusiasm only got fired up more and in June, only two days after I got back from my Erasmus in Tromsø, we decided on a specific subject and set up a plan of attack. I would work on unmelted micrometeorites and use some methods never used before. For this, I went to the ESRF in Grenoble in October where we used the synchrotron power to perform our analyses. Just being in this 'Walhalla' of science was already quite the experience. I got emerged in the scientific world. Despite the long and tiring days, the company was good and the results looked very promising. In barely 5 days we obtained all the data (the full 5 TB) I needed for my project. Almost immediately, the processing of this huge amount of data started and this still isn't completely finished.

In January, we decided I would present my first results at the European Geoscience Union (EGU) General Assembly in Vienna. So, in addition to writing, I created a poster, which I presented in April in Vienna to the big public. Almost the whole AMGC group went there together and again I was introduced to a part of the academic world. Of course, writing my dissertation was my main occupation this semester and I must admit, I kind of liked it. Just like anyone else, some days I couldn't get anything on paper and I was just staring at a blank page. On the other hand, this was the phase where all the results come together and you look for the bigger picture hidden in all the tiny details.

I'm happy that I was able to find my way through the forest of data, questions and answers (which lead to more questions). This dissertation is the final result and I must admit, I'm quite proud of it. I can only hope this opinion is shared by others. Many more questions remain to be answered and I'm very excited to continue the search. I'm pretty sure that I'm not finished yet with micrometeorites and the AMGC group won't easily get rid of me in the near future.

Table of Contents

1. Introduction

1.1. State-of-the-art

Every year, the Earth accretes approximately 40,000 metric tons of extra-terrestrial material, mostly in the form of micrometeorites (Love and Brownlee, 1993) (Figure 1). These particles range in size from 10 – 2000 µm (Rubin and Grossman, 2010). Since they form the main fraction of extra-terrestrial material reaching the Earth's surface and they are thought to originate from different parent material than meteorites (Genge et al., 2008), it is important to study these particles. Micrometeorites are generally recovered from deep-sea sediments, seasonal lakes in Greenland, Greenland and Antarctic ice and snow, or from deserts (Akulov et al., 2014; Badjukov et al., 2010; Duprat et al., 2007; Hutzler et al., 2016; Maurette et al., 1991, 1987; Murray and Renard, 1891).

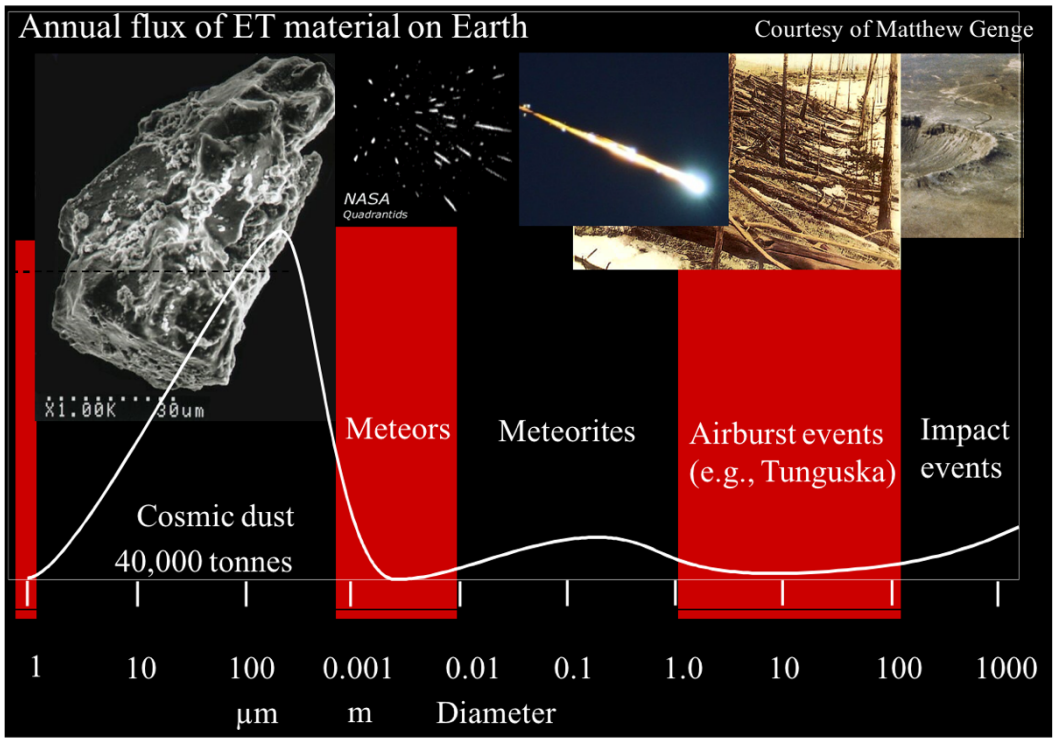

Figure 1: Annual flux of extra-terrestrial material accreted on Earth. On the y-axis, the amount of material is represented. The x-axis shows the diameter of the material (courtesy of Matthew Genge).

More recently, they have also been found concentrated in sedimentary traps near mountain summits in the Transantarctic (Rochette et al., 2008) and Sør Rondane Mountains (Soens et al., 2017; van Ginneken et al., 2017; Goderis et al., 2018 submitted). The sedimentary traps in the Transantarctic Mountains (TAM) and Sør Rondane Mountains (SRM) have proven to be among the most proficient deposits in the world, since large micrometeorites (400 – 1000 µm) are more frequently observed relative to other collections (van Ginneken et al., 2012). The collections of the Transantarctic and Sør Rondane Mountains contain well-preserved and relatively large specimens compared to more conventional micrometeorite deposits, providing a unique

opportunity to study the characteristics of a set of micrometeorites from distinct locations across the Antarctic continent. The excellent preservation of micrometeorites on Antarctica is the result of multiple causes, (i) including the cold and dry Antarctic climate, which slows down weathering processes. (ii) The sedimentary deposits have been subjected to direct infall for time periods in the order of 1 – 3 Ma (Rochette et al., 2008), which is far longer than most other Antarctic (e.g., SPWW, Dome C) and non-Antarctic collections (e.g., deep-sea sediments, ice and snow, deserts). (iii) The TAM and SRM collections are essentially unbiased compared to the pristine SPWW (Suavet et al., 2009; Taylor et al., 1998), and (iv) the identification of micrometeorites is significantly more straightforward due to the lack of anthropogenic contaminants.

Most of the particles entering the Earth's atmosphere are either vaporised or molten, destroying primary petrographic, geochemical and isotopic characteristics (e.g., Cordier et al., 2011; Engrand et al., 2005; Herzog et al., 1999; Taylor et al., 2005). The degree of fusion is mainly influenced by the following parameters: the physico-chemical properties of the particle (e.g., size, composition, density) and the atmospheric entry conditions (e.g., velocity, entry angle) (Love and Brownlee, 1991). Larger and faster micrometeoroids will melt and vaporise, while smaller and slower particles will survive atmospheric entry. For example, cosmic spherules will often be formed from micrometeoroids of approximately 100 – 200 μm diameter (Folco and Cordier, 2015). On the basis of their textural properties, which can be linked to the degree of atmospheric entry heating, micrometeorites are classified in three different groups, i.e. unmelted micrometeorites, scoriaceous micrometeorites and cosmic spherules (Genge et al., 2008). Cosmic spherules are fully melted, (sub)spherical particles formed during atmospheric entry. The primary phases have suffered large degrees of fusion and the particles behave as low viscosity melts. Scoriaceous micrometeorites are particles with a large number of vesicles sometimes exceeding 50% of the particle volume, irregular in shape but with a smooth surface. Another characteristic is the presence of a magnetite rim surrounding scoriaceous micrometeorites. Often, they contain regions of relict fine-grained matrix with Mg-rich pyroxene and olivine grains. Unmelted micrometeorites are divided into two groups based on the grain size. Unmelted fine-grained micrometeorites consist of a fine-grained porous groundmass of micrometre-sized mineral grains with mostly chondritic compositions. These particles may contain subspherical vesicles and show rims of redeposited amorphous material (Genge, 2006). Unmelted coarse-grained micrometeorites are dominated by anhydrous silicates with grain sizes larger than 1 micrometre in a glassy mesostasis (Genge et al., 2008).

Over the last few decades, cosmic spherules have been studied extensively (Cordier et al., 2011; Engrand et al., 1999; Soens et al., 2017; van Ginneken et al., 2017a), while unmelted micrometeorites have received limited attention due to their rarity and small size. Yet, they represent unique material that largely preserved the original petrographic, mineralogical and geochemical properties of the precursor (van Ginneken et al., 2012). Often, they are enclosed by a thin shell of magnetite formed during atmospheric entry. Fine-grained unmelted particles share strong textural and mineralogical similarities with more primitive meteorites like CI and CM chondrites (Genge et al., 1997, 2005). According to Genge et al. (1997), they may contain

tochinilite-like phases, a high-Fe and low-Fe group of relict olivine and pyroxene. There is also a positive correlation between Ca, Na and K, elements sensitive to alteration, which suggests that variations inherited from the precursor might be more significant than those related to alteration. However, the fine-grained micrometeorites often show a depletion in Ni, Mg, Cr and most volatile elements compared to the CM chondrites. Coarse-grained micrometeorites could be linked to a variety of meteorite classes including ordinary chondrites (OC). They may include chondrules, chondrule fragments or minerals found in the matrix of all chondrite types (Genge et al., 1997; Taylor et al., 2012). A cometary origin is ascribed to ultracarbonaceous micrometeorites, a class belonging to the group of unmelted micrometeorites, because of their high D/H ratio, their high carbon content which is in the range of particles originating from the comet 1P/Halley, and the crystalline and amorphous silicates present in this rare type of micrometeorite, which are comparable to the silicates present in the dust of different comets, such as the comet Wild-2 (Dobrică et al., 2009; Duprat et al., 2010; Taylor et al., 2012).

Unmelted micrometeorites thus form a direct window on the cosmic dust present in the Solar System and may be used to complement costly asteroid and comet sample-return missions, such as the NASA Stardust mission to comet Wild-2. This NASA mission focused on the collection of solid samples from the comet Wild-2 of the Jupiter family and the collection of samples from the contemporary interstellar dust stream. Cometary and interstellar particles were trapped in aerogel cells over an exposure time of 195 days in 2000 and 2002 (Westphal et al., 2014). The recovered particles have been characterised, both chemically and mineralogically, by a wide variety of analytical techniques in which non-destructive synchrotron radiation-based X-ray diffraction (XRD) and X-ray fluorescence (XRF) analyses played an important role (Brenker et al., 2014; Flynn et al., 2014; Simionovici et al., 2014; Westphal et al., 2010, 2014). Considering the dense magnetic rim surrounding unmelted micrometeorites, these methods may represent the only analytical tools capable of mapping and imaging the mineralogical and chemical variations in micrometeorites found on the surface of the Earth and tracing their parent body materials without having to destroy them. Previous analysis of a SRM micrometeorite at the European Synchrotron Radiation Facility (ESRF) ID16B beamline provided detailed information on its elemental composition, but not on its mineralogical composition. XRD analysis has been performed on an unmelted micrometeorite at the BM8 beamline of the ESRF, but not in combination with CT or XRF analyses (van Ginneken et al., 2012). Beamline ID16B of the ESRF is a state-of-the-art nanoprobe, ideal for non-destructive hard X-ray nano-analysis and 2D/3D X-ray imaging at submicrometre scale. It offers a wide range of X-ray based methods at nanometre-scale spatial resolutions. The combination of high-performance focusing optics, reliable high-precision scanning stages and efficient detection schemes, all within a stable temperature environment, has proven ideal for a multimodal approach (Martinez-Criado et al., 2015). CT images with nanometre resolution can be obtained, providing more detail and possibilities than a laboratory-based setup. The ability to detect both refractory and volatile components combined with XRD to identify associated mineral phases will provide an accurate representation of the geochemical composition and will allow coupling of the elemental information to the crystallographic data to constrain the primary nature and origin of these micrometeorites. The required detection limits coupled to the high spatial resolution

requirement (~100 nm) for the analysis of trace-level elemental distributions in the samples coupled to the diffraction data, cannot be provided using even the most sensitive, state-of-the-art laboratory-based scanning micro-XRF instruments.

1.2. Research question

The goal of this project is threefold. First, the aim is to create a set of analytical tools for the non-destructive, geochemical and structural characterisation of micrometeorites. At present, there are some difficulties with the analysis of the different types of micrometeorites. The samples are very small (100 – 400 μm) and the magnification in laboratory-based setups is not always adequate. The micrometeorites often have a thick magnetite rim, causing the iron signal to block the signal of other elements in laboratory-based micro-XRF instruments. Here, a synchrotron-based set up is used to examine the samples and assess whether the resolution and sensitivity is more effective to image and analyse the micrometeorites. The second objective is to improve the distinction between scoriaceous and unmelted micrometeorites. Following the classification proposed by Genge et al. (2008), there is still a lack of absolute values for the number of vesicles or chemical abundances to distinguish between the different micrometeorites. The defining arguments are now mainly petrographic descriptions. The studied samples belong to two different collections, the TAM collection and the SRM collection. The comparison between these two collections forms the third objective of this study.

It is expected that the results from the ID16B beamline at the ESRF are more satisfactory than those from a laboratory-based setup and that this experiment will provide a way to non-destructively analyse and image micrometeorites. Based on these results it might be possible to find a way to classify micrometeorites according to their different physico-chemical properties or add on to the existing classification scheme. Also, a difference is expected between the two collections, since the micrometeorites found in the Transantarctic mountains are significantly older (cf. below) and thus have been subjected to the Earth's atmosphere and Antarctic climate conditions for a longer period of time.

2. Geological setting

The unmelted micrometeorite particles studied in this work derive from 2 different sites in Antarctica, the Sør Rondane Mountains and the Transantarctic Mountains (Figure 2).

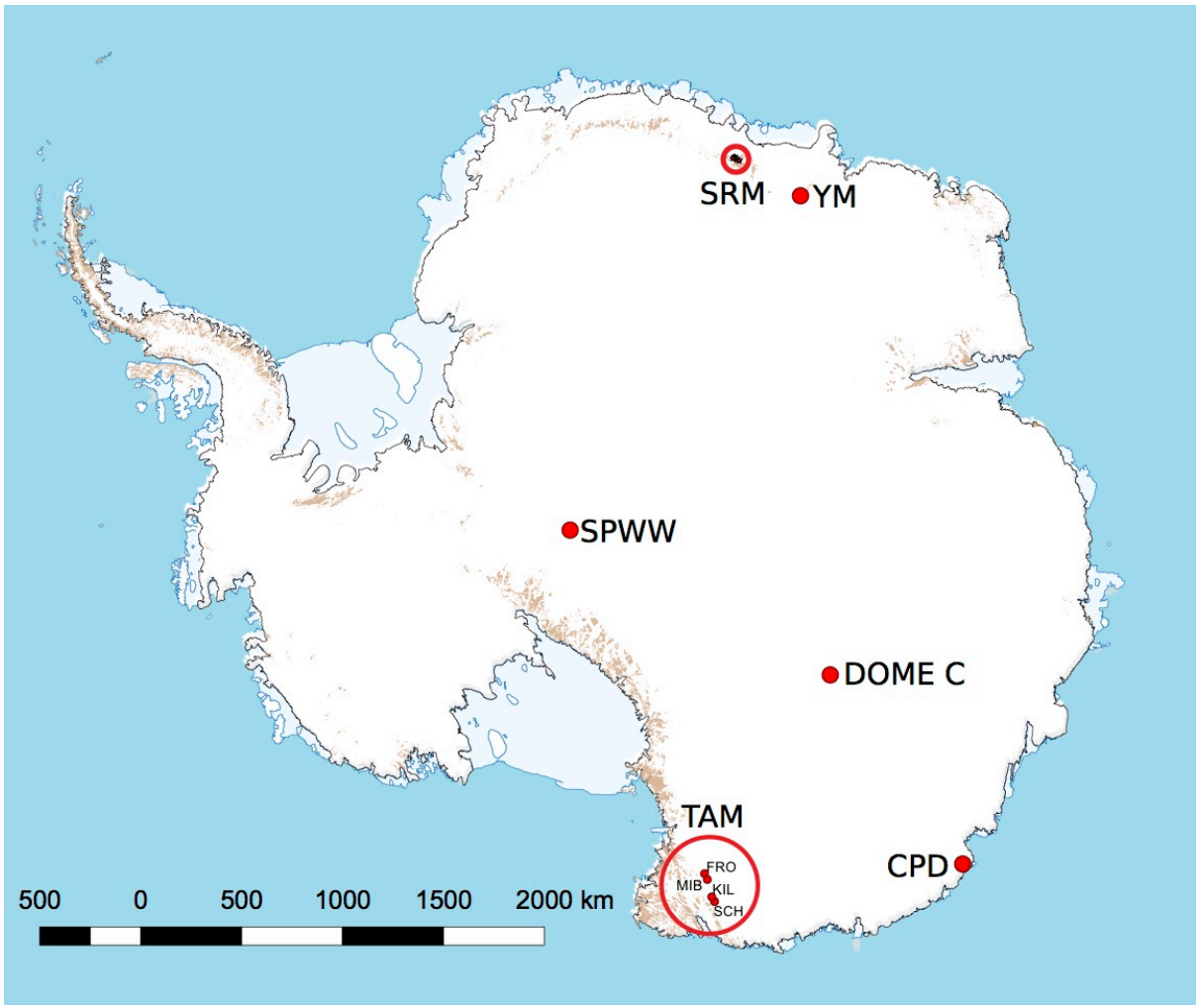

Figure 2: Location of the collection sites of Antarctic micrometeorites. SRM (Sør Rondane Mountains), YM (Yamato Mountains; Yada et al., 2005), SPWW (South pole water well; Taylor et al., 1998), Dome C (Concordia collection; Duprat et al., 2007), CPD (Cap Prud'homme; Maurette et al., 1991), TAM (Transantarctic Mountains); Rochette et al., 2008). The locations marked with a red circle are the sites where the samples for this study were collected.

The Transantarctic Mountains are located in Victoria Land, East Antarctica and the samples were collected in the northern part of the mountain range. They consist of glacially eroded granitic summits. Weathering pits and eroded granitic joints are scattered across the surface and can function as micrometeorite traps. During the Italian 2003 and 2006 Programme Nazionale delle Ricerche in Antartide (PNRA) expeditions, a large number of micrometeorites was discovered in these kind of traps on Frontier Mountain, Miller Butte, a nunatak in the Timber Peak area (Pian delle Tectiti) and Mistake Peak (Rochette et al., 2008). Based on cosmogenic nuclide measurements, the exposure age of the granitic surface on Frontier Mountain is in the range of

4.4 Myr. During this period, the only source of allochtonous material deposited here since the exposure of the surfaces is atmospheric infall (e.g., tephra, micrometeorites and microtektites). Australasian microtektites, i.e. distal microscopic impact glass spheres, recovered from these traps have been dated at ~0.8 Myr, validating that these structures have collected micrometeorites for an extended period of time, i.e., at least during the last 1 Myr (Folco et al., 2009).
The collection from the Transantarctic Mountains (TAM collection) has been shown to be essentially unbiased and contains a wide variety of extraterrestrial materials. It holds a large number of micrometeorites with diameters larger than 500 µm, as well as unmelted micrometeorites compared to other collections (Suavet et al., 2009; van Ginneken et al., 2012).

The Sør Rondane Mountains are located in eastern Dronning Maud Land, East Antarctica. The mountain range consists of low- to high- grade metamorphic rocks and various kinds of plutonic rocks that intruded the metamorphic basement. Based on the different constituent rock types and metamorphic conditions, two terranes are identified: the NE terrane, dominated by granulite-facies metamorphose and the SW terrane, dominated by amphibolite- to greenschist-facies metamorphic basement (Osanai et al., 2013). The large group of nunataks is distant from any coastal outlet and shows geomorphological evidence that a large part of this 2000 km^2 area used to be covered by an expanded ice sheet. Based on cosmic-ray exposure, the mountain range has been exposed for 1.9 Myr. Today, the elevation of the ice sheet surface is 1000 m in the north, rising to 2500 m in the south (Suganuma et al., 2014). Based on sensitive high-resolution ion microprobe U-Pb zircon ages, the last tectonothermal event occurred 500-650 Myr ago and the area has been geologically stable ever since (Shiraishi et al., 2008).
This area has a similar potential for the retrieval of micrometeorites in the same kind of traps as in the Transantarctic Mountains (Figure 3). During the joint expedition between Belgium and Japan, a large number of micrometeorites was collected in the 2012 – 2013 field season, to set up a collection similar to the TAM collection. The samples used in this study are all part of the Widerøefjellet deposit 2A.

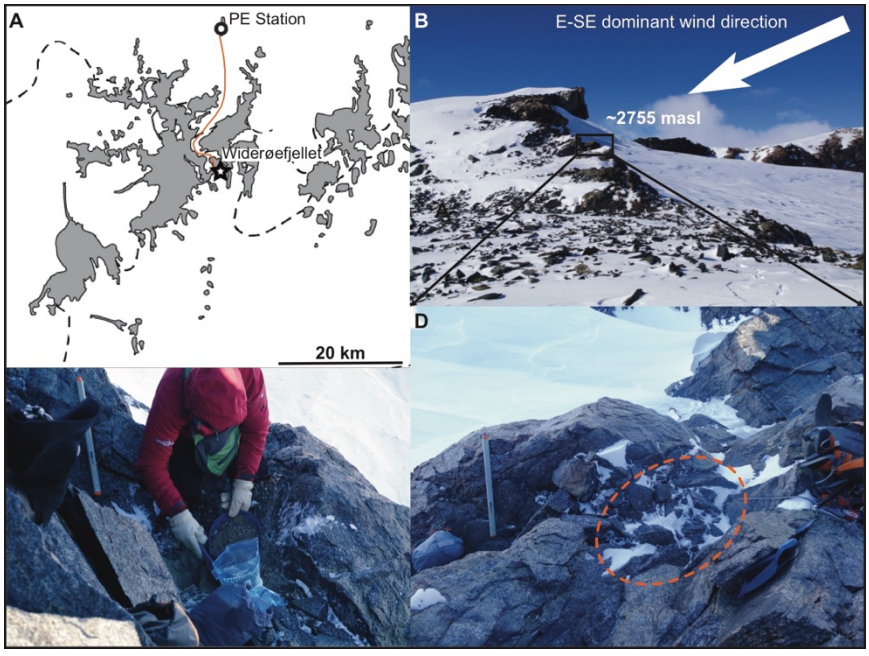

Figure 3: A) Location of Widerøefjellet in the SRM opposed to the Princess Elisabeth station (PE station). B-D) Example of micrometeorite trap with the dominating wind direction.

The sediment trapping mechanism (Figure 4) has been proposed to mainly take place in joints and weathering pits of 10 – 30 cm in diameter and 5 – 15 cm in depth of the bed rock. After some time of weathering and host rock disaggregation, a sufficient depression for accumulation is formed. Most depressions are empty, but some are filled with host rock detritus and show a local magnetic maximum (Rochette et al., 2008). During periods with strong winds, there is no deposition. During calm periods, vertically falling particles are most likely captured in the gravel layer. When the trap is covered in snow, there is no accumulation because particles will be windblown unless the snow can make its way to the gravel level (Rochette et al., 2008). However, the mechanism may differ from deposit to deposit and remains the topic of ongoing studies (Genge et al., 2018).

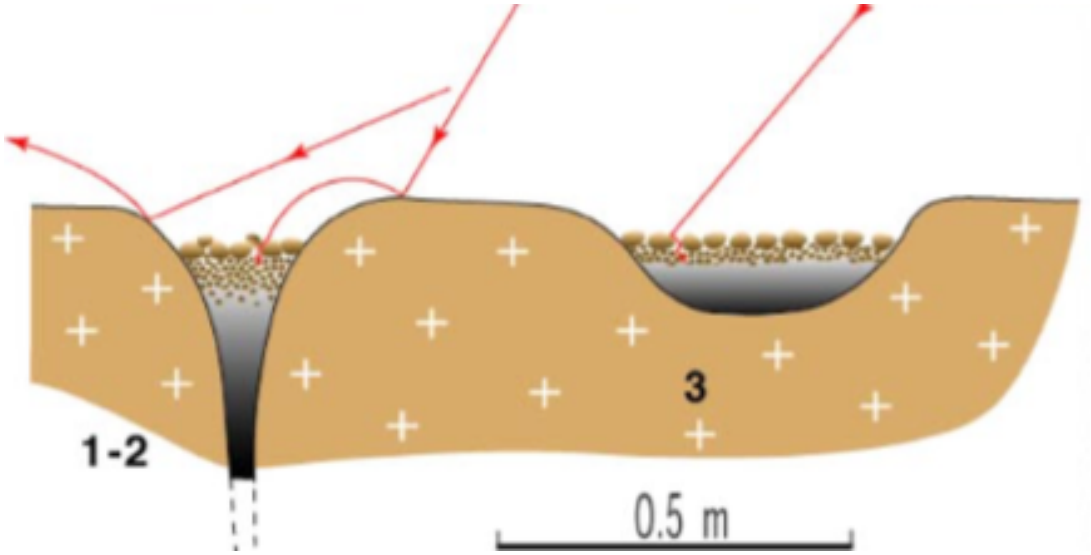

Figure 4: Proposed mechanism for the two types of sediment traps (Rochette et al., 2008).

3. Material and methods

3.1. Extraction of SRM micrometeorites

For the extraction of micrometeorites from the Sør Rondane Mountains, a quarter of the Widerøefjellet 2A deposit was separated and weighed. The sediment was wet-sieved to remove the finest fraction and divided into different size fractions: >2000 μm, 2000-800 μm, 800-400 μm, 400-200 μm, 200-125 μm and <125 μm. The different fractions were subsequently placed in a drying oven for approximately one day. To extract the micrometeorites from the sediment fractions, a hand magnet was used. Micrometeorites are commonly enriched in magnetite, which is magnetic, formed during the oxidation of iron (Fe) during atmospheric entry. Afterwards, the different size fractions were examined with a binocular microscope to pick out potential cosmic spherules. The remaining sediment was analysed using the microXRF instrument Bruker M4 Tornado at the Vrije Universiteit Brussel and scanned for Ni and Cr. Black, angular particles that contained these two elements, were identified as possible unmelted micrometeorites. About 70 particles were hand-picked and form the foundation for this study.

The samples from the Transantarctic Mountains were provided by Prof. dr. Luigi Folco of the University of Pisa, Italy.

3.2. Scanning Electron Microscopy (SEM)

First, a scanning electron microscope (SEM) (Figure 5) was used to produce back-scattered electron (BSE) images. Electrons are accelerated in the electron gun and hit the sample. The electron beam reacts through elastic and inelastic scattering on the atoms making up the sample. From these interactions, various signals are produced such as secondary electrons (SE), back-scattered electrons (BSE) and Auger electrons (AE). The BSE are produced as a result of the deceleration of electrons caused by scattering. They form near the surface of the sample and cover a broad spectrum of energy (Figure 6). The intensity of the signal is related to the atomic number of the material (Z) and the relative orientation of the incident electron beam relative to the lattice planes (Reimer, 1998).

The selected micrometeorites from the Sør Rondane collection were characterized using a JEOL JSM IT-300 scanning electron microscope – energy dispersive spectrometer (SEM-EDS) system at the Vrije Universiteit Brussel. The samples from the TAM collection were analysed using the FEI Quanta 200 scanning electron microscope (SEM) at the Royal Belgian Institute of Natural Sciences (RBINS). The extra-terrestrial nature of the particles was confirmed based on their textural (e.g., presence of magnetite rim, vesicularity) and chemical properties (e.g., presence of Ni, chondritic major element ratios).

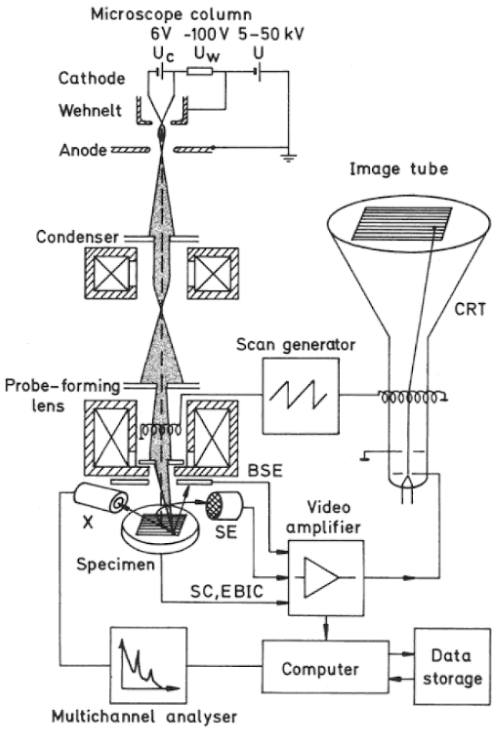

Figure 5: Principle of a scanning electron microscope (SEM). BSE = backscattered electrons, SE = secondary electrons, SC = specimen current, EBIC = electron-beam-induced current, X = X-rays, CRT = cathode-ray tube (Reimer, 1998).

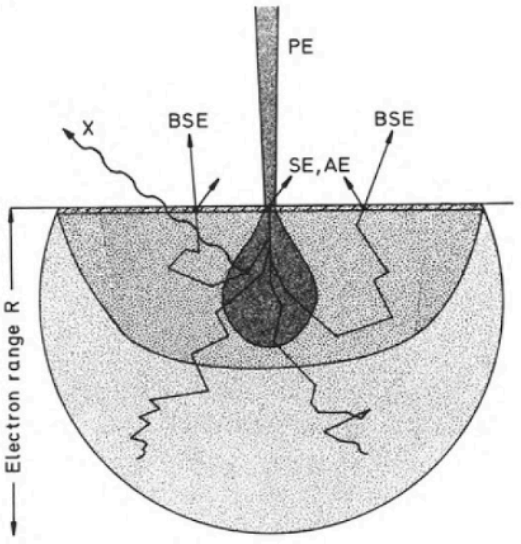

Figure 6: Origin and formation depth of the reaction products in a SEM. SE = secondary electrons, BSE = backscattered electrons, AE = Auger electrons, X = X-ray quanta (Reimer, 1998).

During a later stage of this study, 5 particles were examined again using the SEM-EDS system at the Vrije Universiteit Brussel. First, the samples were polished sequentially with sandpaper SiC 2000 (9 μm) and 4000 (3 μm) and with diamond polishing powder with a grain size of 3 μm and 1 μm on a rotating disk at a speed of 300 rpm. This way, the micrometeorites were sectioned, leaving a clean transect which was scanned with the SEM to characterise and measure the structures and determine the mineralogical composition.

3.3. Analytical X-ray based techniques

Several analytical techniques were applied in this study. First, an overview of these techniques is presented with some general information. Then, the different instruments and facilities are presented in more detail.

X-ray computed tomography (CT) is a method in which a volume of material is reconstructed in a non-destructive way. This method is based on Beer's law (Eq. (1)), which links the measured intensity I to the initial X-ray energy I_0, path length x and the linear attenuation coefficient of the material μ (Cnudde and Boone, 2013; Ketcham and Carlson, 2001).

$$I = I_0 exp\left[\sum_i (-\mu_i x_i)\right] \quad (1)$$

X-ray attenuation is related to the density of the object through the linear attenuation coefficient and often density transitions can be linked to differences in materials or phases. This makes CT imaging an excellent method to apply in geosciences. A large number of radiographs are acquired at different angles (0-360°) and these radiographs are then combined to form a 3D volume of the selected object. In laboratory setups, a standard cone beam is used (Figure 7). This allows geometrical magnification by placing the object at different positions between the source and detector. At synchrotron facilities, a parallel beam configuration is used (Figure 7). Here geometrical magnification is impossible, but the high X-ray flux allows a high spatial resolution (Baruchel et al., 2006; Cnudde and Boone, 2013).

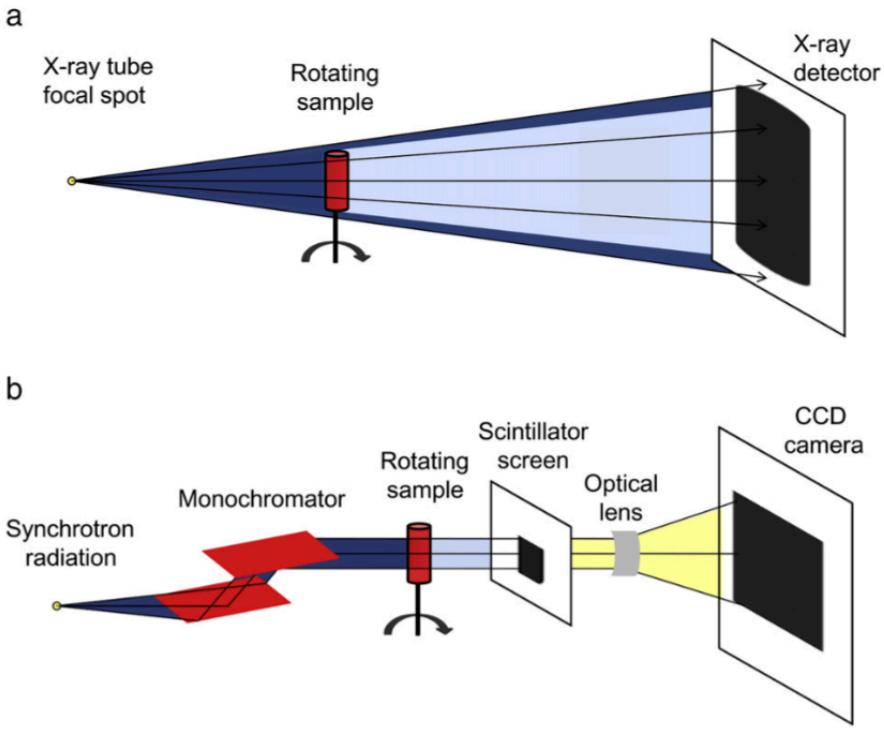

Figure 7: Schematic diagram of the setups for CT scanning. a) Laboratory-based setup with a cone beam. b) Synchrotron-based setup with a parallel beam. This beam is formed due to the long propagation distance. The monochromator selects an energy with a certain bandwidth. The beam is attenuated by the sample and converted to visible light by the scintillator screen. With optics, this image can be magnified onto a visible light detector (Cnudde and Boone, 2013).

X-ray fluorescence (XRF) is a method used to obtain elemental information. High energy X-rays interact with the electrons in the sample. The incident energy is transferred to an electron from an inner-shell which is subsequently ejected as a photoelectron. This process, called the photoelectric effect (Figure 8), leaves a vacancy. The empty spot is filled in by an electron from a higher shell, re-emitting its excess energy as a characteristic X-ray. The energy is equal to the energy difference between the excited electron and the energy of the shell with the vacancy. The emitted energy is characteristic for the given element and can be used to identify this element in the sample (Beckhoff et al., 2006).

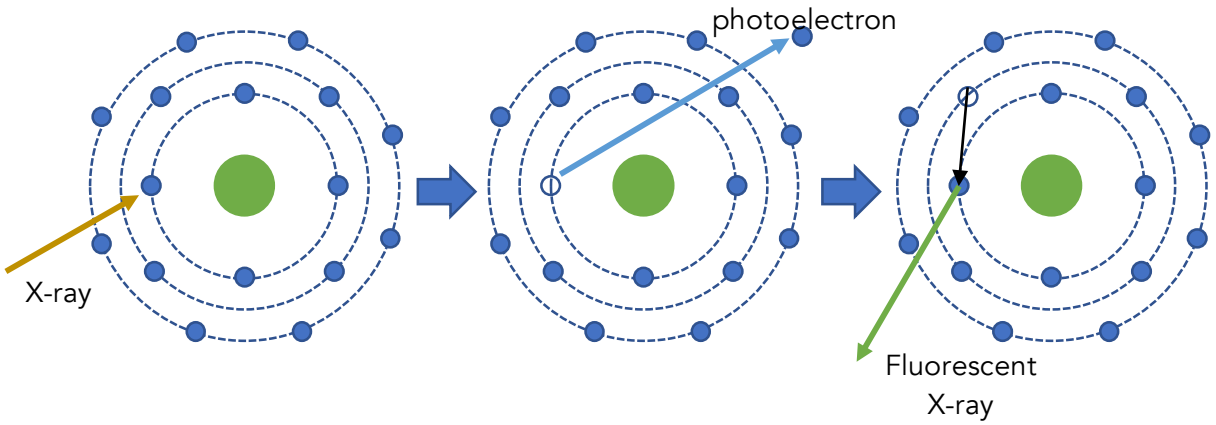

Figure 8: Photoelectric effect: the incident X-ray creates a vacancy by emitting a photoelectron. The empty spot is filled in by an electron from a higher shell. This action is paired with the emission of characteristic, secondary X-rays (fluorescent X-ray).

X-ray diffraction (XRD) (Figure 9) provides a way to acquire information about the crystallinity of a material. Incident X-rays are scattered by interaction with crystallographic planes, which occur following a regular spacing (d) characteristic for the type of crystal. Most scattered waves are cancelled out by destructive interference, but in some specific directions, determined by Bragg's law (Eq. (2)), there is constructive interference. These reflections form the foundation for the diffraction pattern, which is characteristic for each crystal structure or mineral (Suryanarayana and Grant Norton, 1998).

$$n\lambda = 2d\sin\Theta \qquad (2)$$

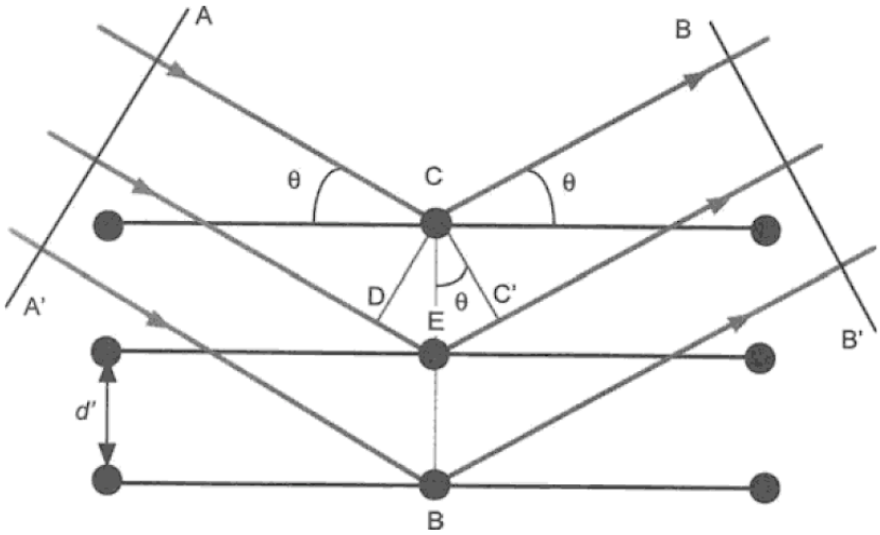

Figure 9: Illustration of Bragg's Law. The diffraction pattern is created based on the constructive interference of the X-rays reflected by the crystal planes. (Suryanarayana and Grant Norton, 1998).

3.3.1. Herakles

Herakles is a 3D laboratory-based X-ray scanner (Figure 10) in which high-resolution X-ray transmission tomography (μCT), confocal X-ray fluorescence (cXRF) and X-ray fluorescence tomography (XRF-CT) are combined. The device was developed and built at Ghent University. The data from the different imaging end-stations is coupled through a high-precision motor stage in order to actively link the data obtained using the different techniques (Laforce et al., 2017). The confocal XRF setup consists of a 50 W (50 kV) Mo anode tube with polycapillary optics that generate a focused X-ray beam with a working distance of 3.6 mm and a spot size of 10 μm x 13 μm (H x V) at the Mo Kα-line energy (17.48 keV). The fluorescent photons are collected with two large area SDD detectors (100 mm^2 crystal area) positioned on either side of the source under a 90° angle. One of the detectors is used in conventional 2D XRF modelling (RadEye detector), the other uses polycapillary optics for 3D confocal XRF experiments.

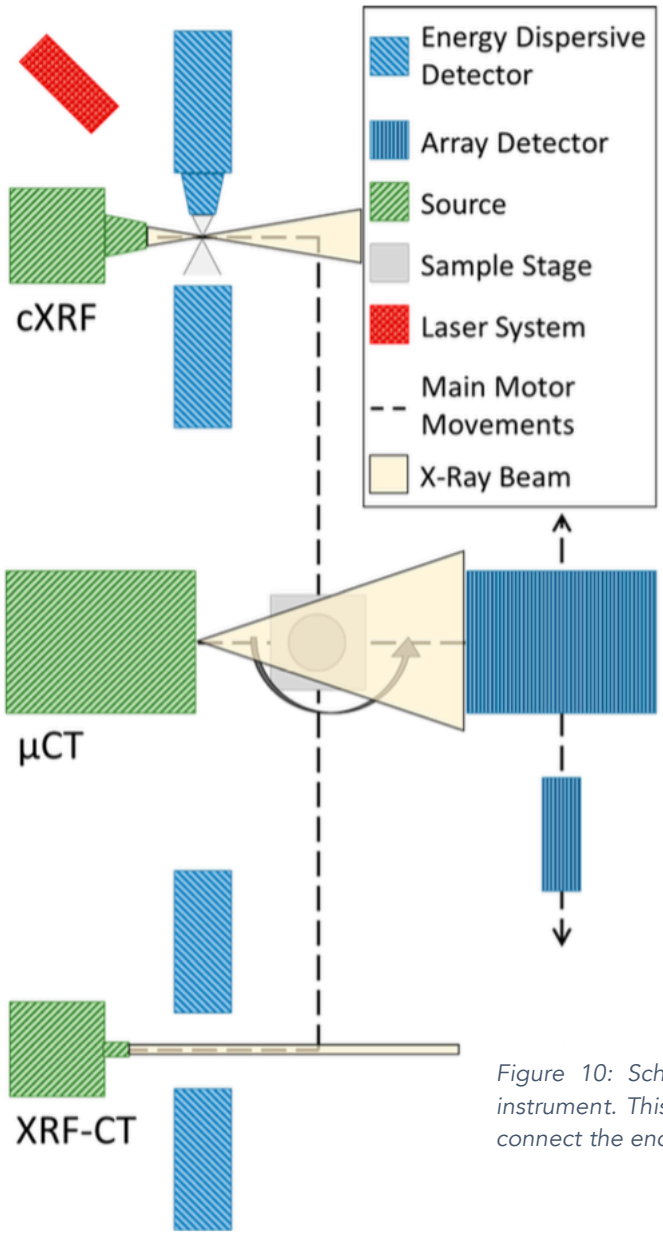

Figure 10: Schematic overview of the setup of the Herakles instrument. This image shows how the motor system movements connect the end stations (Laforce et al., 2017).

The µCT setup has as X-ray source an open transmission-type microfocus X-ray tube (X-RAY WorX, Garbsen, Germany) with a high-resolution tungsten target. The smallest spot size is 700 nm. The applied voltage is between 20 and 100 kV, with a maximum target power of 10 W. To reduce thermal dimension changes, the tube head is cooled with water. The photons are detected by means of 2 different X-ray detectors: the Photonic Science VHR CCD sensor (Photonic Science, Millham, UK) for imaging low-attenuating samples or the RadEye CMOS detector (Teledyne DALSA Inc., Ontario, Canada), which is better for the analysis of high-attenuating samples, such as geological and meteoritic materials (Laforce et al., 2017). The motor system consists of 13 independent motors on a mafic table. The sample stage is moved with an ultra-high precision air-bearing motor system, which provides a good reproducibility of ca. 100 nm (Laforce et al., 2015). In this way, the measurements can be carried out in the same coordination system for all three measuring stations and the data of the different techniques can be easily coupled.

The laboratory-based analysis of the micrometeorite samples was performed with both the µCT and cXRF end-station of the Herakles scanner. µCT scans used the tube at 70 kV and 3 W in combination with the RadEye detector. The selected voxel size was 2.2 µm, while a 360° scan was performed using 501 projections at 0.5 s measuring time per point. XRF scans at the cXRF end-station employed the conventional (2D) SDD detector. The tube was at 40 kV and 0.6 mA, while 20 µm steps were taken with 5 s live time per point.

3.3.2. ESRF Beamline ID16B

The selected samples were studied at the ID16B beamline of the ESRF in Grenoble, France, through non-destructive analysis by synchrotron source X-ray fluorescence (XRF) and X-ray diffraction (XRD) and imaged by computed tomography (CT). The experiments for this research were executed during the experiment ES-676 consisting of 8 successive shifts of 12 hours each.

The ESRF ID16 beamline (Figure 11) consists of two branches: ID16A is equipped for nano-imaging applications down to approximately 10 nm resolution, while ID16B is a hard X-ray nanoprobe for nano-analysis dedicated to 2D or 3D analysis of nano-scaled material. It combines X-ray fluorescence and diffraction (XRF and XRD), X-ray absorption spectroscopy (XAS), X-ray optical luminescence and phase contrast imaging with an X-ray beam size down to 50 nm. The ID16B nano-analysis end station is located 165 m from the source. Close to the source, in the optics hutch, a double white beam mirror (DWM) and double-crystal monochromator (DCM) are placed to ensure the beam coherence and minimise beam instabilities. Three different beam operation modes are possible based on the elements present in the optics hutch: the low-energy monochromatic mode; the high-energy monochromatic mode; and the pink beam mode. Due to the long distance between the X-ray source and the working station, the system has a high spatial resolution resulting from a high source demagnification. In combination with the Kirkpatrick – Baez (KB) mirror nanofocusing optics placed closely to the sample, the setup yields spot sizes of approximately 50 nm. At the end-station (Figure 12), the KB optics, sample stage, visible-light microscope and XRF detectors are mounted on a mafic block. For the scintillator screen cameras

used for XRD and X-ray imaging, two additional stages are present. The sample stage is a combination of three-axis, motorized translation stages with an air-bearing nano-spindle rotation stage (Laforce et al., 2014, 2016; Martinez-Criado et al., 2016).

Depending on the analysis, several detection schemes are possible. The X-ray beam comes in perpendicular to the sample positioning system. For XRF experiments, silicon drift detectors (SDD) are used to measure the XRF signals. Here, two identical detectors from SGX Sensortech, each containing three-element SDD array modules with beryllium windows, were mounted at an angle close to 90° with respect to the incoming X-ray beam and in the plane of polarization (Martinez-Criado et al., 2015). During the experiments described in this work, one element of these detector array modules was failing, so only five detector elements of the six could be used. Due to the inherent characteristics of XRF spectroscopy performed in an ambient environment, only elements with an atomic number Z larger than 14 (Si) can be detected. This detection limit is defined by the concentration value at which the detected peak intensity can be distinguished from random fluctuations of the corresponding background. The detection limit for Ca (Z = 20) is 150 ppm. This value decreases with an increasing atomic number and for elements like Cu and Zn this is 1 ppm (Laforce et al., 2014).

When performing XRD, the fiber-optic taper version of the FReLoN F_4320T camera is installed in transmission geometry. Here, the X-rays are converted into visible-light photons by a scintillator screen. Then, the photons are guided by a tapered fiber-optic bundle that is bonded to a Kodak CCD sensor. In the beamstop support, a photodiode has been integrated to measure the transmitted beam intensity simultaneously with the camera exposures (Martinez-Criado et al., 2015). The XRD data was obtained but is not presented in this study due to memory storage problems to process the data. To compare, the XRD data size is a couple 100 GB per sample, while the XRF data size is only a couple MB per sample.

For magnified imaging, a FReLoN 4M F_4320 camera system is used, equipped with a x3.1 magnification eyepiece leading to a pixel size of 7.6 μm^2 with a field of view of 2048x2048 pixels. A scintillator screen converts the X-rays into a visible-waveband image, which is magnified by optics onto a CCD sensor camera. The microscope includes a motorized, triple scintillator mount, motorized triple objective lenses (4x/0.16 - 10x/0.30 - 10x/0.40) and a motorized camera rotation to ensure perfect angular alignment of the CCD pixel array with the sample scan axes (Martinez-Criado et al., 2015).

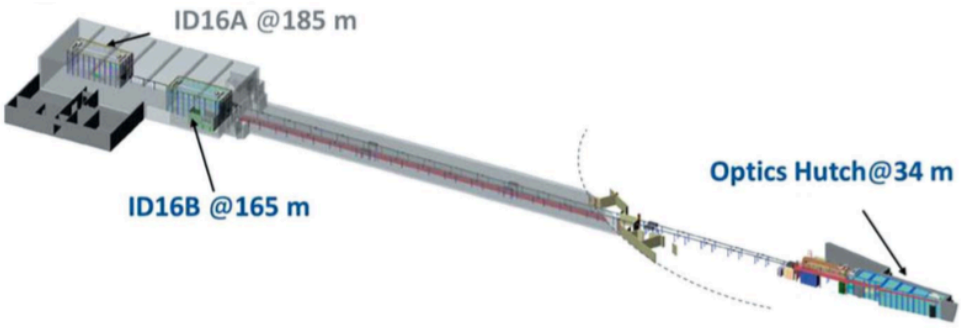

Figure 11: Schematic representation of the general layout of the ID16 beamline at the ESRF (Martinez-Criado et al., 2015).

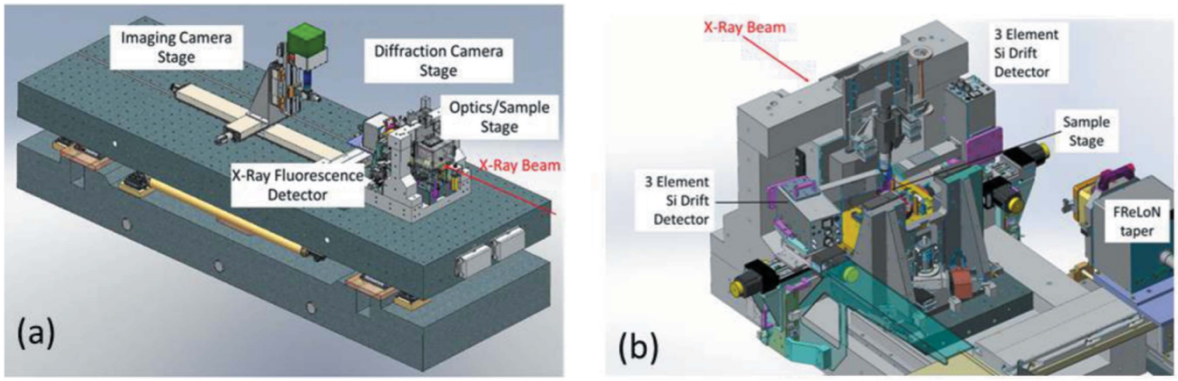

Figure 12: a) Schematic close-up of the ID16B end station. b) Detailed view of the detection stage, with the FReLoN camera parallel to the incoming X-ray beam and the Si Drift Detectors (SDD) perpendicular to the incoming X-ray beam on both sides of the sample (Martinez-Criado et al., 2015).

The micrometeorite particles were mounted on polymer tips using epoxy glue (Figure 13). These tips were attached to brass pins suitable for the sample mounting system at beamline ID16B. Previous experiments using these mounting tips have shown that they do not contain impurities which interfere with the XRF signal.

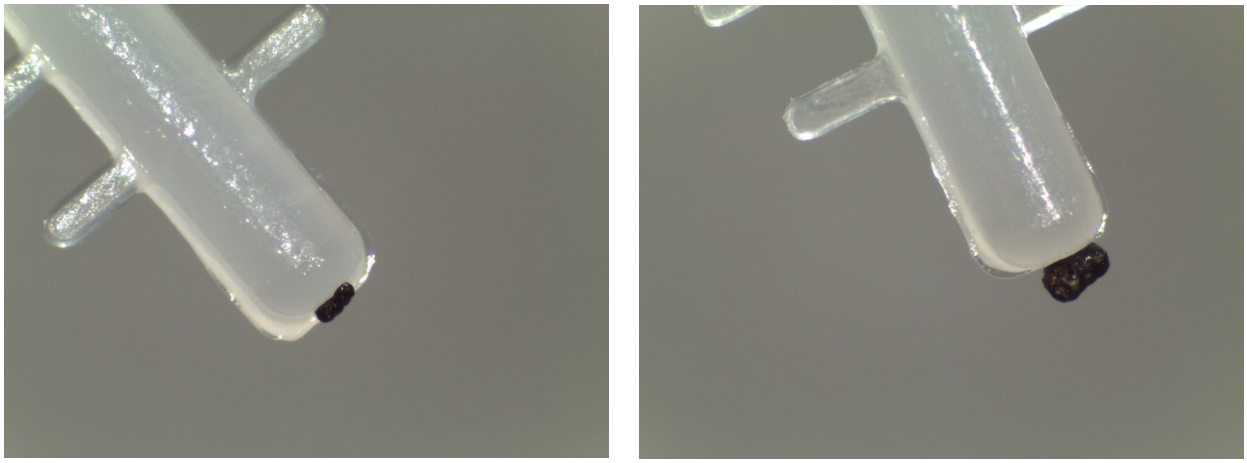

Figure 13: Sample Sc3 (left) and sample TAM2 (right) mounted with epoxy glue on polymer tips with a diameter of 1.5 mm.

The scans at ID16B were performed using pink beam mode (at 17.5 keV), optimal for high-sensitive XRF experiments, but suboptimal for XRD measurements, which would benefit from monochromatic radiation. Step sizes ranged from 50 to 400 nm and measurement times per point were between 0.05 and 1 s, these settings being optimized for each individual scan. Several scans on reference materials were performed to characterize the setup. Two MPI DING reference glasses (ML3B-G, GOR132-G) and NIST SRM 1832 were used as reference for quantification. Upon arrival at the beamline, a piece of sample Uc2 appeared to have broken off during transport.

3.4. XRF analysis

The XRF spectra are analysed using the software package AXIL (Analysis of X-rays by Iterative Least Squares; Van Espen et al., 1986; Vekemans et al., 1994). It allows the elemental identification of XRF spectra and the determination of background-subtracted line intensities. The program extracts information such as peak shapes, peak overlap and background from the spectral data. First, a model file is constructed for every sample by adapting the region of interest, the background type and the fluorescence lines. AXIL evaluates the XRF data using a non-linear least-squares fitting of a mathematical model to minimise the difference between the experimental data and the constructed model. From AXIL, a model file and report file can be saved. This report file contains the peak areas of the fluorescence lines and will be used for the quantification. Afterwards, elemental maps are created with the in-house developed MICROXRF2 package. This software allows the user to fit multiple files with the model file constructed in AXIL and to create 2D plots with the intensities of all elements defined in the model file.

The fundamental parameter method is a quantification method that takes into consideration various parameters, such as the differences in density, thickness, geometry and the type of matrix that may influence the X-rays on their radiation path. The fundamental parameter equation (Eq. (3)) is used to calculate the concentrations (Rousseau and Boivin, 1998; Schoonjans et al., 2012).

$$\frac{I_{i,s}}{I_{i,r}} = \frac{c_{i,s}.\rho_s.T_s.A_{i,s}}{c_{i,r}.\rho_r.T_r.A_{i,r}} \qquad (3)$$

with i the given element, s the sample, r the reference material, I the intensity, c the concentration or weight fraction, ρ the density, T the thickness and A the correction factor.
In order to calculate the concentration of the element in the sample, Eq. (3) has to be rewritten:

$$c_{i,s} = \frac{I_{i,s}.c_{i,r}.\rho_r.T_r.A_{i,r}}{I_{i,r}.\rho_s.T_s.A_{i,s}} \qquad (4)$$

Most of the parameters can be found in literature or derived from the experimental setup. The absorption correction factor is more difficult to estimate, because it depends on different parameters itself: the mass attenuation coefficient, the geometry of the setup (angle of the incoming X-rays and angle of the detector), the incident and fluorescent radiation, the geometry of the sample and the concentration of the element of interest in the reference material and sample (Schoonjans et al., 2012). The starting values for the calculation are equal to the concentrations in the reference material. New concentration values are obtained after calculation. These new values can be used to calculate the absorption correction factor of the unknown sample. This process is iterative and is repeated until the difference between successive concentrations for each element is less than 5% in the unknown sample.

3.5. CT analysis

Using the Fiji (Fiji is just ImageJ) freeware package, the raw CT image stacks are first reduced in memory size. Black images are removed and the images are cropped. The stacks are converted to tiff-files for further analysis with Octopus analysis and Octopus View (Octopus Imaging Software). Octopus is a software package used to analyse and visualize CT data and results in high quality constructed 3D volumes, which enables the extraction of useful parameters (e.g. porosity, size parameters) (Brabant et al., 2011; Vlassenbroeck et al., 2007). For every sample, the same workflow is applied in Octopus Analysis (Figure 14). First, a mask is created, by setting a threshold on the colours of the image stack and applying binary operations. This mask is then set as the volume of interest (VOI). Next, the vesicles inside the VOI or micrometeorite are segmented, first by using the threshold function and then fine-tuned with binary operations. The inverted mask of this result is saved as an image stack for following steps. Afterwards, a labelling operation is used to identify the different objects in the selection. Each object is treated individually, and various parameters could be measured or the objects, in this case the vesicles, could be visualised in Octopus Visualisation (Figure 15). Octopus Analysis also provides an excel file with the measured parameters for each object as output. The same steps are performed for the image stack with the inverted mask to reconstruct and analyse the volume of the micrometeorite.

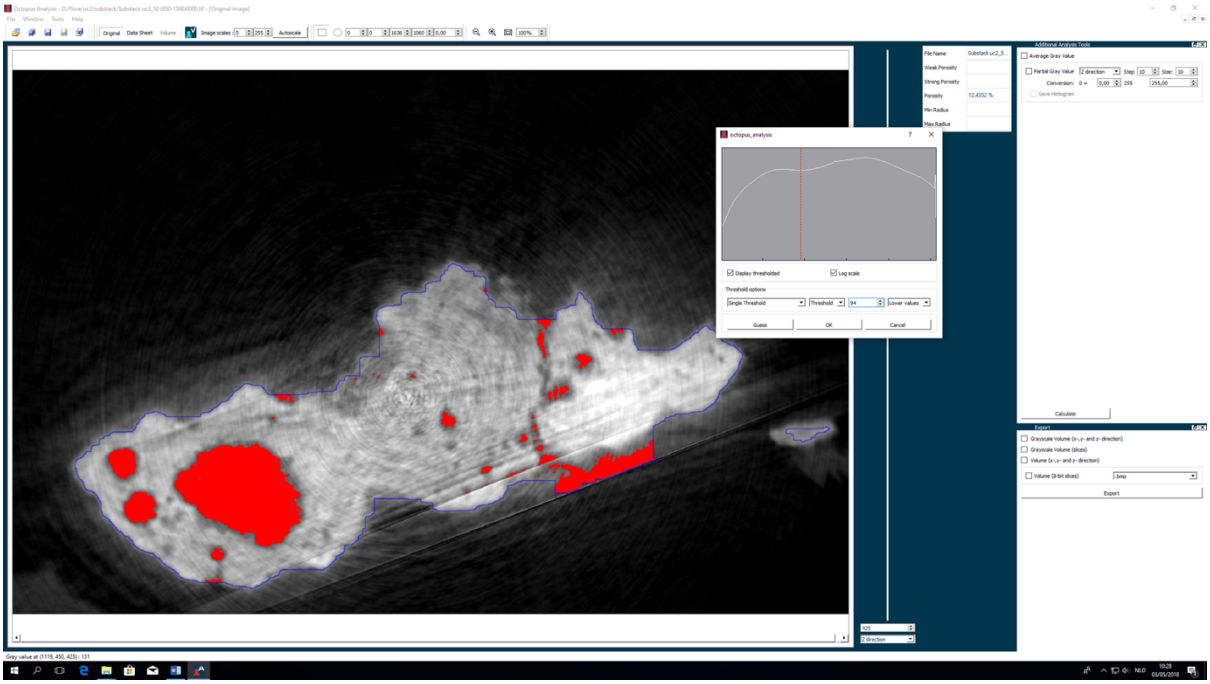

Figure 14: Work space in Octopus Analysis for the thresholding step of sample Uc2.

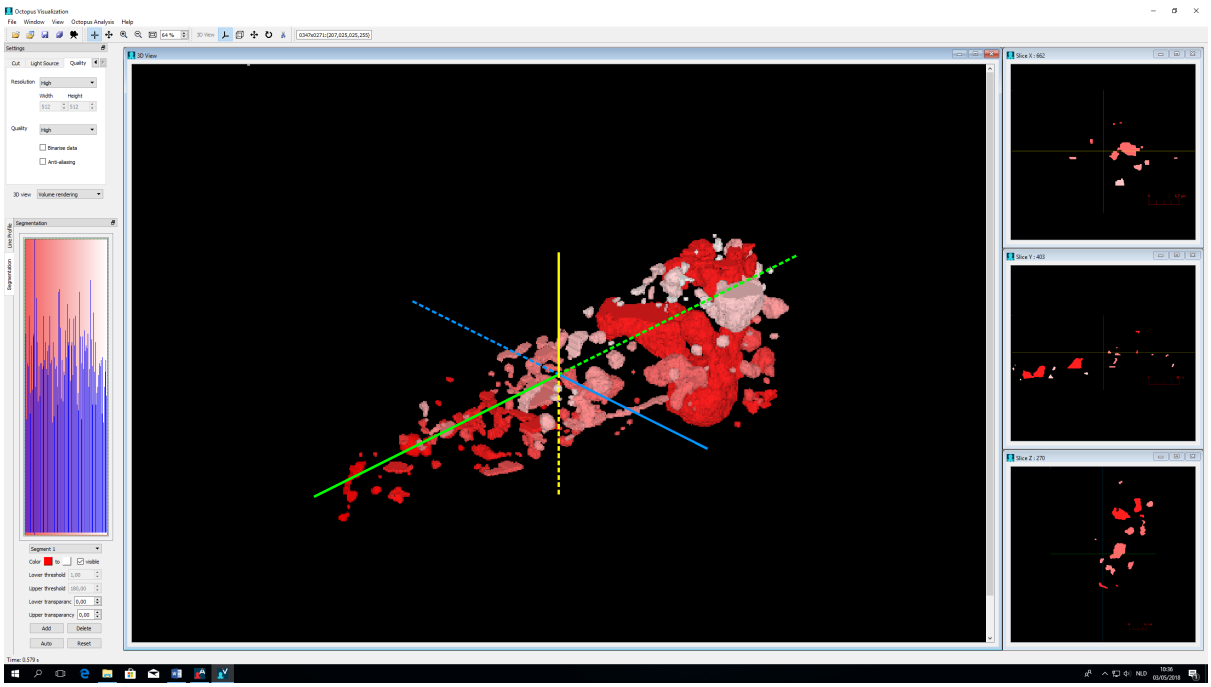

Figure 15: Work space in Octopus Visualisation for the 3D volume rendering of the pores of sample Uc2.

4. Results

4.1. Scanning Electron Microscopy

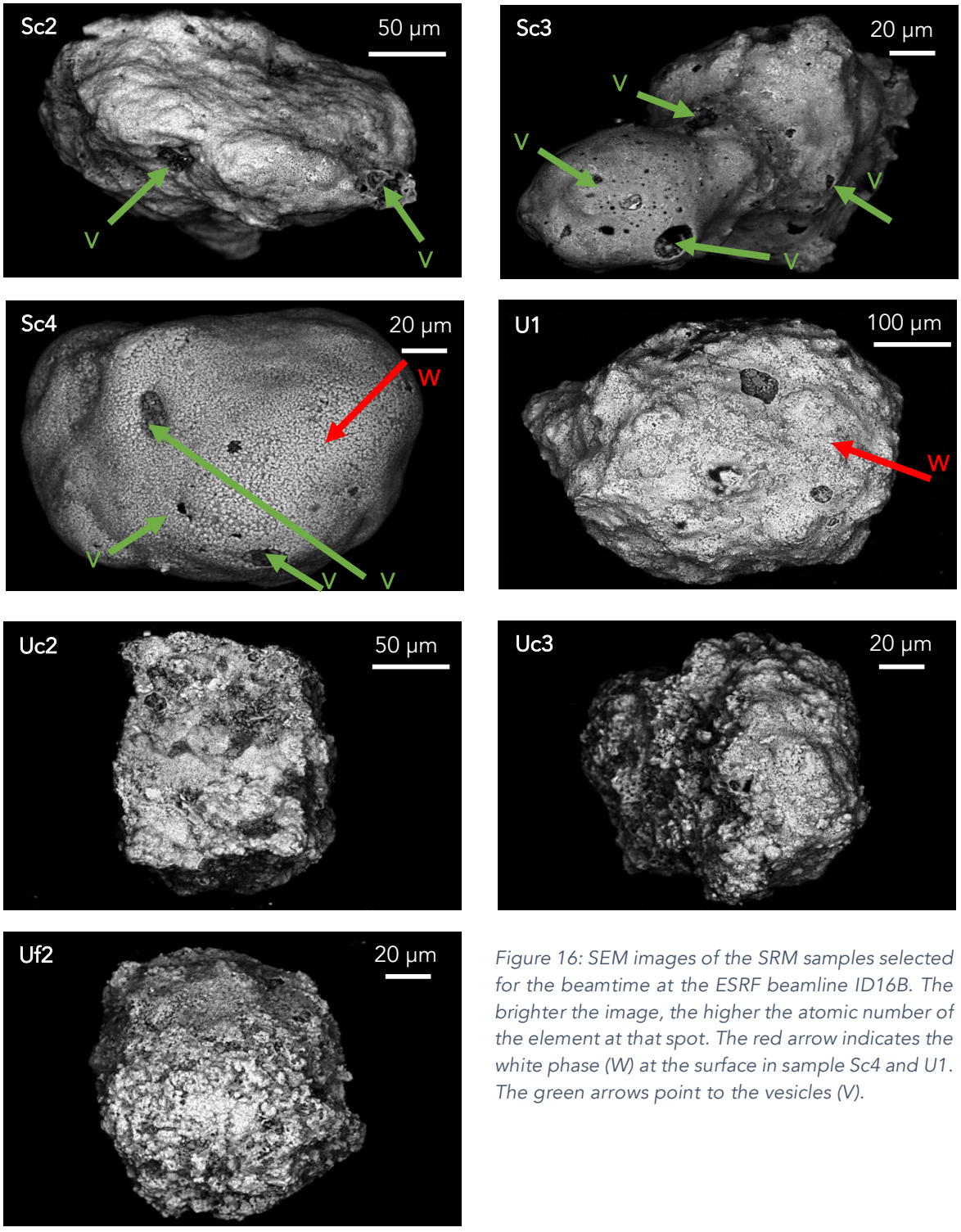

Figure 16: SEM images of the SRM samples selected for the beamtime at the ESRF beamline ID16B. The brighter the image, the higher the atomic number of the element at that spot. The red arrow indicates the white phase (W) at the surface in sample Sc4 and U1. The green arrows point to the vesicles (V).

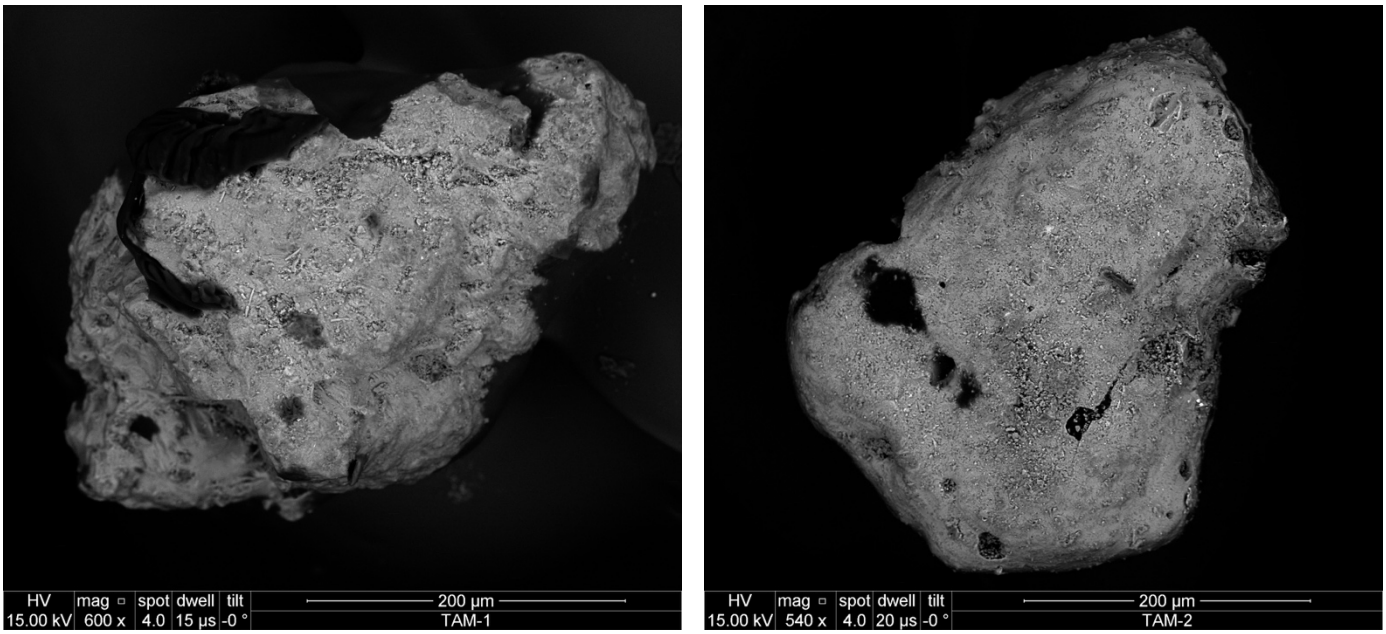

Figure 17: SEM images of the samples from the TAM collection selected for the beamtime at the ESRF beamline ID16B.

In Figure 16, the SEM images in BSE mode from all the samples from the SRM collection used for the analysis at the ID16B beamline are presented. The SEM images from the samples from the TAM collection are presented in Figure 17. Based on these images, the statistical diameter for each particle is determined (Figure 18). Since the particles are not completely round, the diameter is determined in the same way as for cosmic spherules (Suavet et al., 2009). The statistical diameter SD is calculated using Eq. (5).

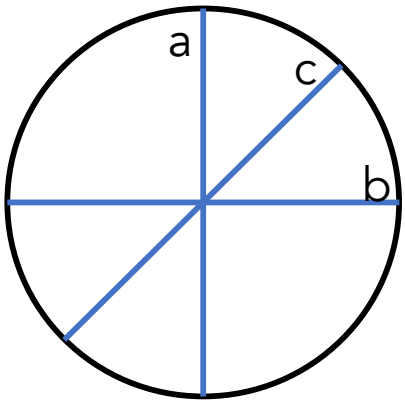

Figure 18: Illustration of the axes used to calculate the statistical diameter.

$$SD = \sqrt[3]{a.b.c} \quad (5)$$

It is assumed that the axes a>b=c which means that Eq. (5) can be rewritten as

$$SD = \sqrt[3]{a.b^2} \quad (6)$$

The values are given in Table 1. All micrometeorites range in size between 138 and 408 µm. Samples from the TAM collection are ~300 µm, while all samples from the SRM collection are approximately 138 – 185 µm in size, except for sample U1, which is 408 µm.

The outer part of the micrometeorites is covered with a white, high-density phase as indicated in samples Sc4 and U1. This white layer is spread uniformly across the surface of samples Sc4 and

U1. For samples Sc2, Uc2, Uc3 and Uf2 this layer is discontinuous, while it is absent for sample Sc3. In the samples from the TAM collection (Figure 17) this white layer is also absent. For samples Sc2, Sc3 and Sc4 several vesicles can be observed at the surface and these are accompanied by more rounded surface features. Samples U1, Uc2, Uc3 and Uf2 have more angular surface features, as well as the samples from the TAM collection.

Based on the petrographic features observed in the SEM images (Figure 16), the samples of the Sør Rondane collection were roughly classified after their discovery and named accordingly. The main criteria are (i) the presence of a magnetite rim, visible as a white, denser outer layer in backscatter electron (BSE) mode, (ii) the morphology, and (iii) the presence, abundance and size of vesicles (visually estimated). Samples Sc2, Sc3 and Sc4 are thus labelled as scoriaceous micrometeorites. These have a rounded shape, many vesicles and a white magnetite rim in BSE mode. Samples U1, Uc2, Uc3 and Uf2 are categorized as unmelted micrometeorites. They have a more angular shape, little to no vesicles and a more irregular magnetite rim. This group has preliminarily been further divided into coarse grained (Uc2 and Uc3) and fine grained (Uf2) unmelted micrometeorites. One of the main goals of this study is to confirm and refine this working classification by further analyses. Based on these observations, regions of interest for further study were selected. These regions of interest are mostly concentrated on areas where the magnetite rim is visually thinner and the possibility of obtaining elemental and mineralogical information from deeper within the particle is higher.

4.2 CT scans

In Figure 19, one CT slice of every sample from the ultrahigh resolution scans performed at the ID16B beamline is displayed. The denser the object, the brighter it looks in a CT image. In each sample, multiple vesicles are observed. These are indicated by green arrows in the figure. The red arrow in sample Sc4 points at the outer, white rim of a few microns thickness that surrounds the entire micrometeorite. The uniform core of sample Uf2 is surrounded by a vesicular structure which is brighter and thicker in the lower right corner. This phase is marked by a green square. The blue arrows mark white, highly dense phases in samples TAM1 slice a, U1 and Uf2. In TAM1, this phase has an angular shape, while in samples U1 and Uf2 it has a rounded aspect. In sample TAM1, another phase can be observed: a rectangular less dense shape in slice b, pinpointed by a red square. In sample U1, individual crystals can be distinguished.

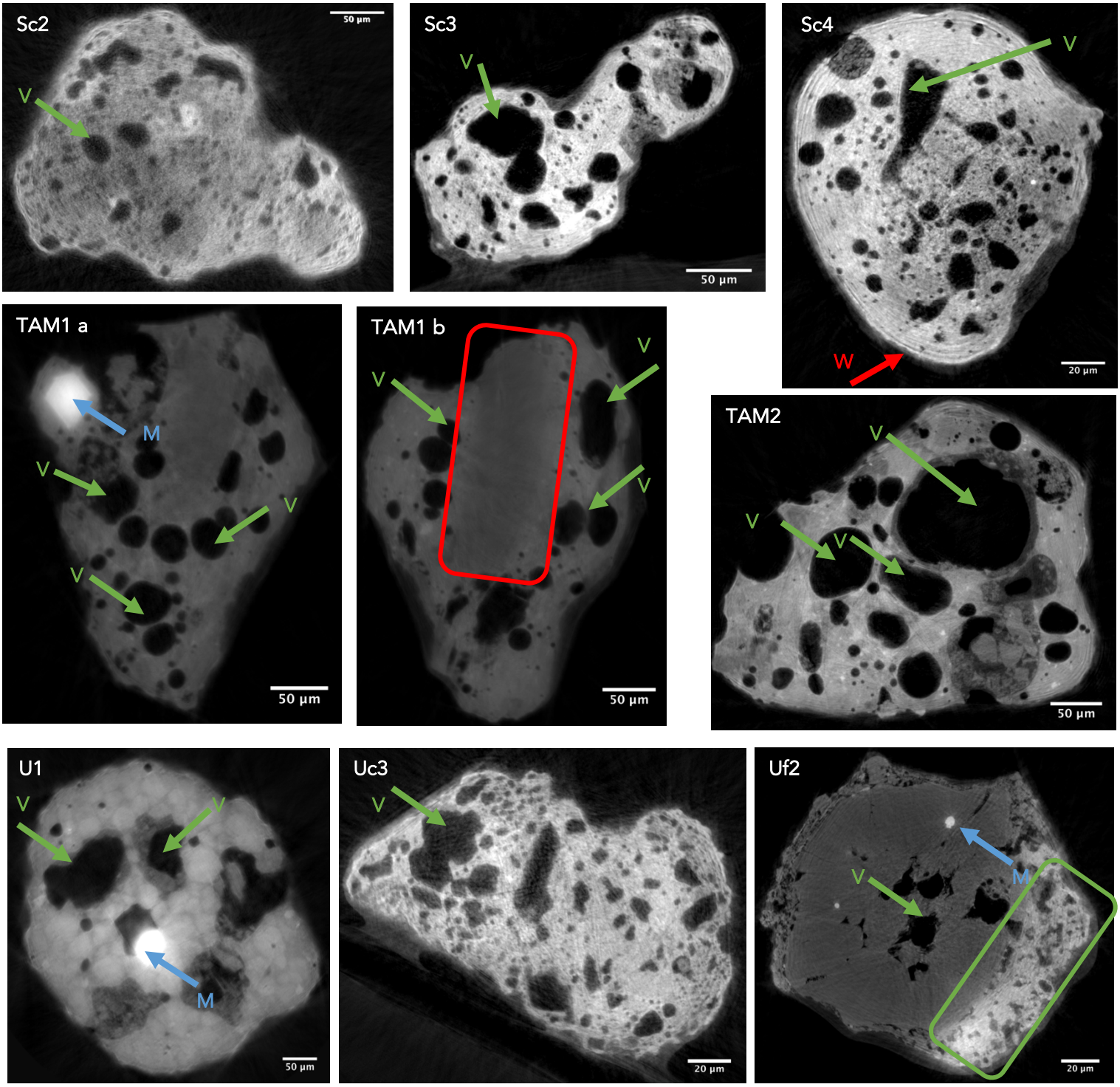

Figure 19: CT slices of all samples from the beamtime at the ESRF beamline ID16B. The brighter the image, the denser the material in this spot. The green arrows indicate the vesicles (V), which occur in all samples. The red arrow in sample Sc4 points at the outer white rim (W): a denser phase at the edge of the micrometeorite. The blue arrows in sample TAM1 slice a, U1 and Uf2 point at a highly dense white phase (M) present in these samples. The red square in sample TAM1 slice b indicates a less dense rectangular phase. The green square in sample Uf2 indicates the vesicular, brighter phase at the edge of this sample.

4.2.1 Octopus Analysis

The CT scans obtained at the ID16B beamline at the ESRF, are used as a basis for 3D reconstructions of the samples using the software package Octopus Analysis and Octopus Visualisation. The 3D reconstructions visualise the micrometeorite material and the volume of internal vesicles (Figure 20).

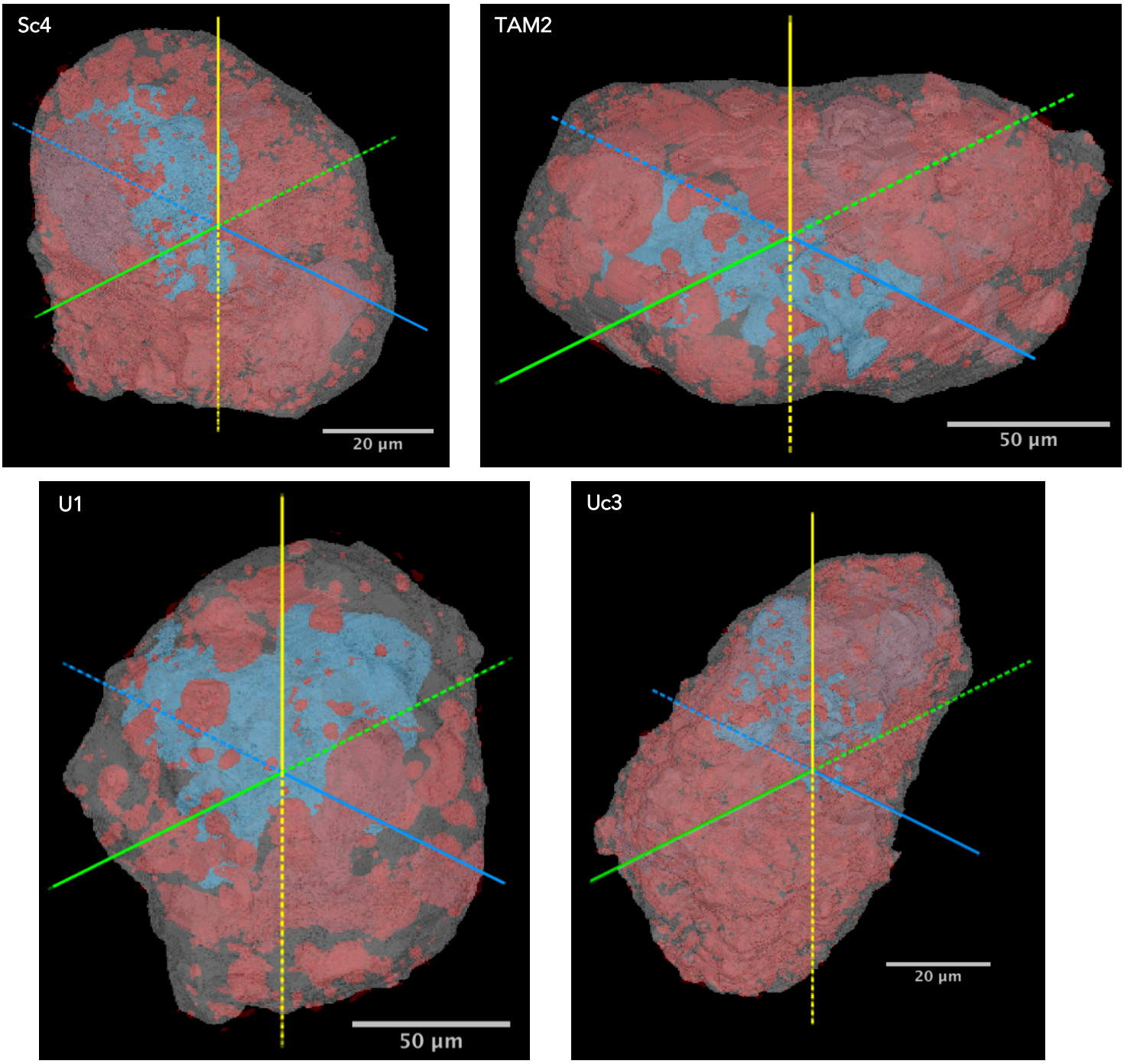

Figure 20: 3D volumes of several samples reconstructed by Octopus Visualisation. On every image, the x, y and z axis are represented by respectively a blue, yellow and green (dashed) line. The surface is coloured in grey and rendered transparent in order to visualise the vesicle distribution inside. The size range of the vesicles is given by the colour red (small vesicles) to blue (large vesicles).

Octopus Analysis determines several parameters including porosity, vesicle quantity and equivalent diameter. This data is presented in Table 1. Based on the porosity values observed during this study, three groups can be distinguished: (i) 2 micrometeorites with a porosity of less than 9 vol% (green), (ii) 4 micrometeorites with a porosity between 10 and 15 vol% (orange), and (iii) 3 micrometeorites with high porosities of more than 19 vol% (yellow). The number and equivalent diameter can be computed for all the vesicles. The total number of voids varies between 180 and 3185. The porosity is independent of the size of the crystals but the largest vesicles seem to occur in the largest particle (TAM1, TAM2 and U1). The equivalent diameter is the diameter of the sphere with a volume equal to that of the vesicle that has an irregular shape. This parameter observed in all of the samples varies between 0.4 and 186.1 µm. Within the different samples, this range also varies significantly (e.g. in sample Sc4 the equivalent diameter ranges between 0.6 and 55.9 µm, while for sample U1 this varies between 1.4 and 186.1 µm).

Table 1: Results on the vesicles of every sample determined using Octopus Analysis. The colour scale separates the micrometeorites in three different groups based on the porosity. In green are the micrometeorites with a porosity of less than 9 %; in orange, micrometeorites with a porosity between 10 and 15 %; and in yellow, micrometeorites with a porosity of more than 19 %.

Sample	Diameter sample (µm)	Porosity (vol%)	Total number of vesicles	Number of voxels per vesicle	Equivalent diameter (µm)	Scale (µm)
Sc2	185	8.9	2203	120 – 12,184,891	1.08 – 51.3	0.18
Sc3	152	23.3	1009	125 – 18,652,706	1.2 – 65.8	0.2
Sc4	138	19.8	3185	125 – 91,298,150	0.6 – 55.9	0.1
TAM1	350	11.7	709	125 – 75,132,354	1.2 – 104.8	0.2
TAM2	304	22.8	1081	7 – 148,623,654	0.4 – 131.4	0.2
U1	408	13.2	694	125 – 277,570,177	1.4 – 186.1	0.23
Uc2	170	11.1	180	343 – 9,222,003	0.6 – 38.2	0.1
Uc3	142	14.6	3071	125 – 29,075,536	0.6 – 38.2	0.1
Uf2	144	8.7	3701	100 – 45,407,022	0.6 – 44.3	0.1

4.3 X-Ray Fluorescence

4.3.1 Results from Herakles

Data not presented in this chapter can be found in the Appendix (SI A).

The data obtained by the Herakles is used to compose elemental maps. These maps provide an indication of possible regions of interest, despite the restricted number of elements (e.g., Sr, Mn, Ti, Ca, Fe, Ni, Cr) with sufficiently high signal-to-noise ratios (Figure 21). Most signals are obscured by the signal from Fe, which is present in large concentrations (10^5 – 10^6 counts) at the outer rim of the micrometeorites. The XRF spectra (Figure 22) show which elements are present in the bulk sample with their respective concentrations. In every sample, Fe is the most abundant element covering a range of approximately 10^5 - 10^6 counts. The samples recovered from the Sør Rondane Mountains are systematically enriched in Cr and Ni, and generally exhibit high Ca peaks. Conversely, these samples contain lower concentrations of K, Sr and Ti. The samples from the Transantarctic Mountains (TAM1 and TAM2) are systematically enriched in K, Sr and Ti, while they contain only minor amounts of Cr and Ni.

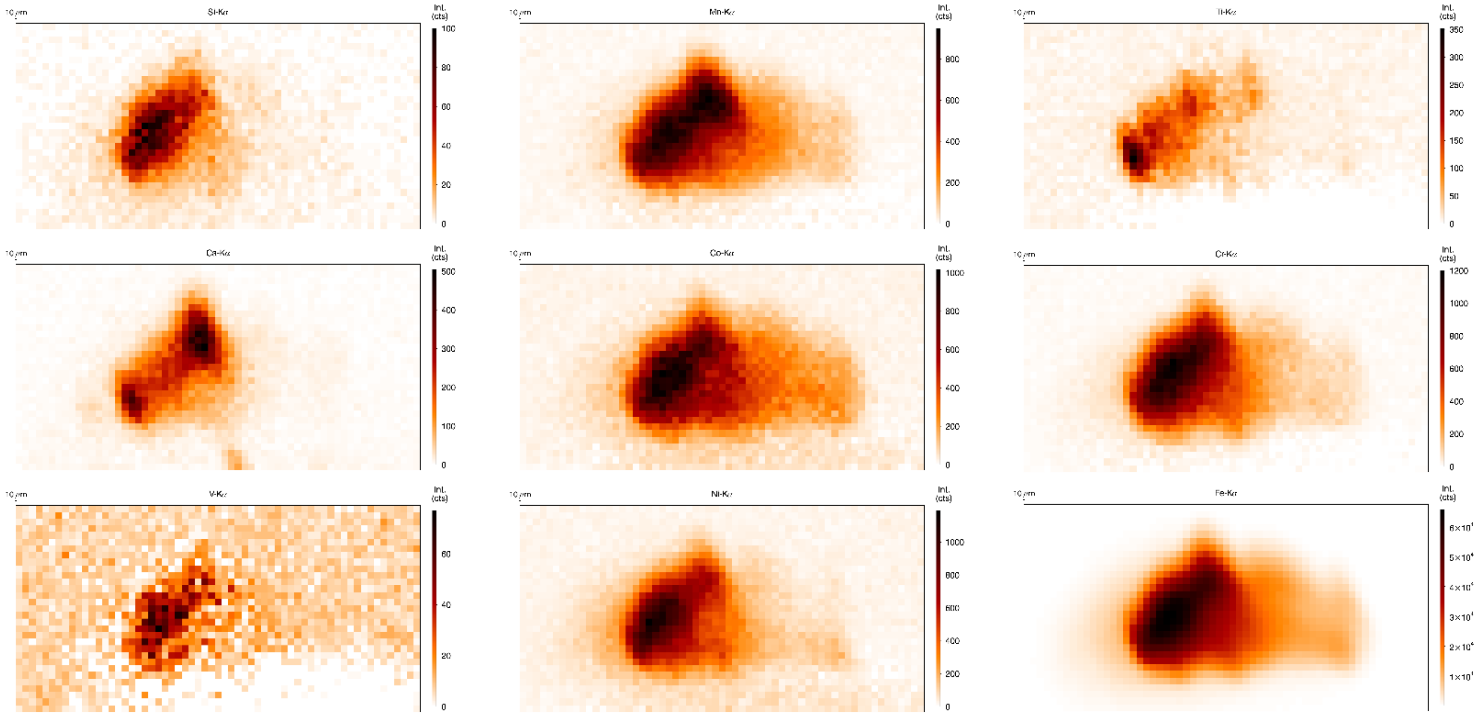

Figure 21: Elemental maps constructed based on the data obtained at the Herakles for sample Sc2. The intensity for every element is given in counts. The darker red, the higher the intensity of the element in that spot.

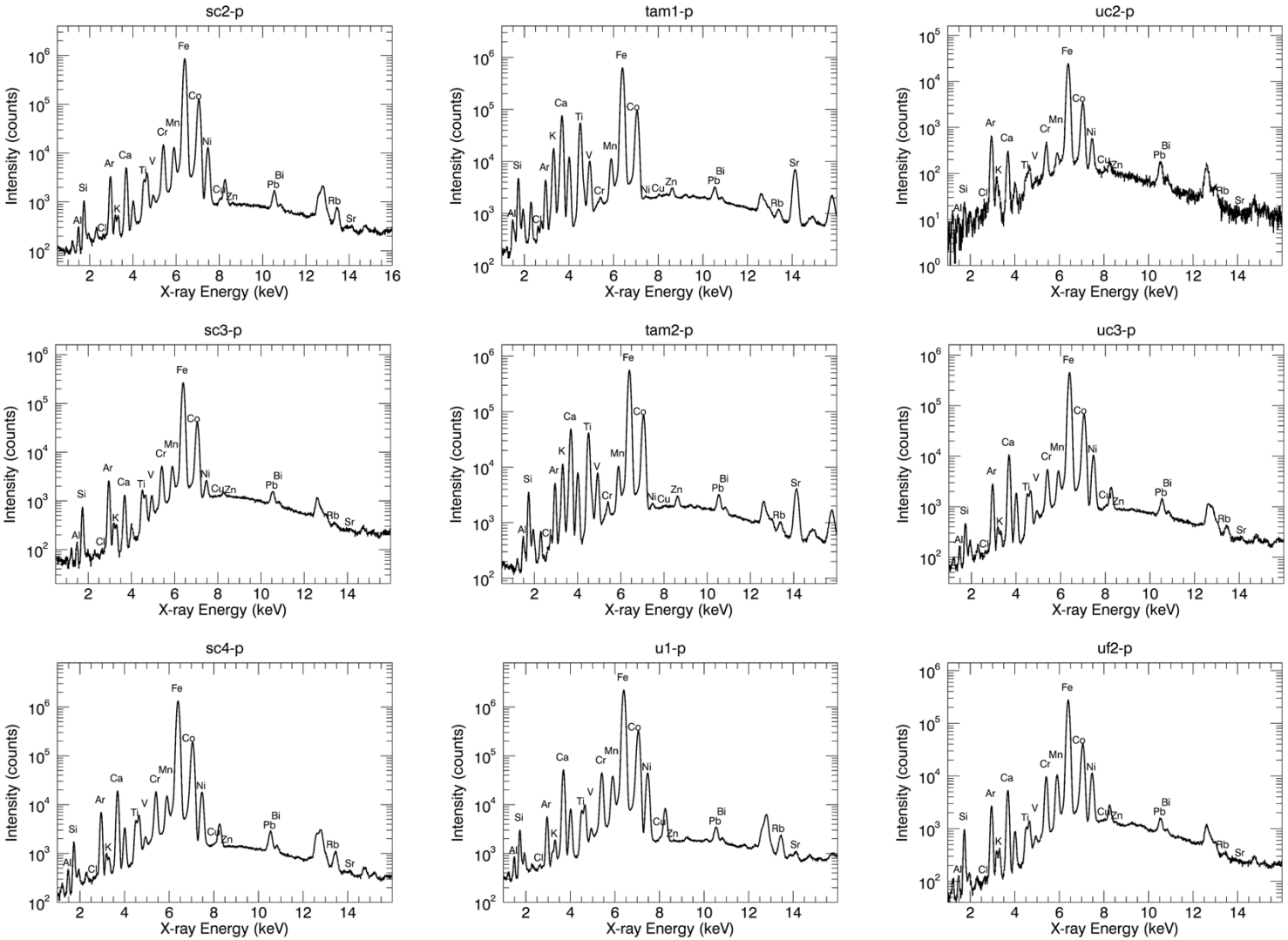

Figure 22: The XRF spectra based on data obtained using the Herakles instrument for all samples later analysed at the ID16B beamline at the ESRF. On the y-axis, the intensity of the elements is given in counts; on the x-axis, the X-ray energy is given in keV. For the most prominent peaks, the identified element is marked.

4.3.2 Data from ID16B

Elemental maps not presented in this chapter, can be found in Appendix (SI B).

From the data retrieved at the ID16B beamline, elemental maps for the various elements identified can be produced (Figure 23 - Figure 28) oriented along the x-axis (blue) in the 3D reconstructions from Figure 20. While Fe still has the highest intensity, several elements such as Ni, Cr, Mn, Sr, Ca and Ti display sufficiently high signal-to-noise ratios to provide informative elemental maps. The intensity of the Fe signal lies in the range of $2.0x10^3$ – $3.0x10^4$ counts and covers the complete field of view. Signal intensity may vary and can be less for example when the crust shows indentations or damage. In the samples from the TAM collection (Figure 26 - Figure 28), Cr and Ni are only present as localised isolated rounded zones (beads). In contrast, for samples from the SRM collection (Figure 23 - Figure 25), these elements may occur as localised beads or are scattered throughout the field of view following the distribution of Fe. Manganese generally follows the same distribution of Fe, although it often occurs as enriched beads which correlate well with Cr and, to a lesser extent, Ni. Calcium and Sr often occur together in enriched zones, rather than in localised beads, and are observed in both micrometeorite collections. Titanium is mainly present in the TAM micrometeorites as small bar-shaped features (Figure 27). In sample TAM1, a rectangular shaped Sr enriched zone is present (Figure 26). This zone is also slightly enriched in Ca. The detail XRF measurements of the Cr/Ni bead in sample TAM2 (Figure 28), indicates that this phase is also enriched in other elements like Pb, Mn and Co and depleted in Rb, Sr, Ga and V. In sample U1, a Ni bead is present on the right of the centre of the field of view, which shows a depletion in Fe and Mn (Figure 25).

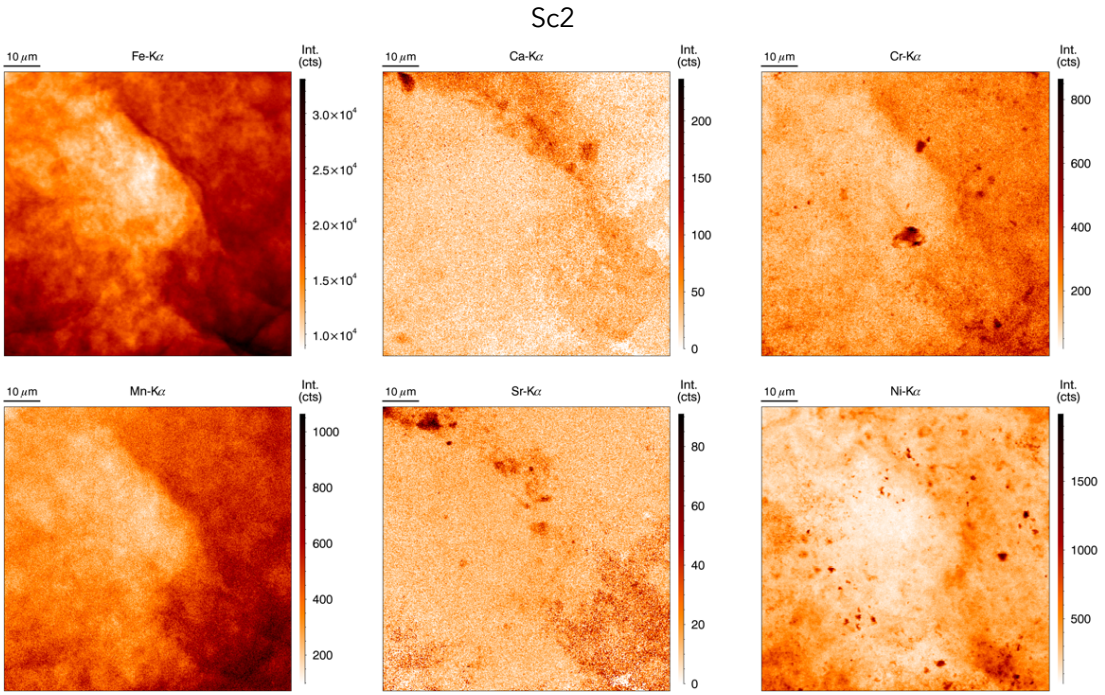

Figure 23: Most informative elemental maps constructed based on the data obtained at the ID16B beamline of the ESRF for sample Sc2. The intensity for every element is given in counts. The darker red, the higher the intensity of the element in that region.

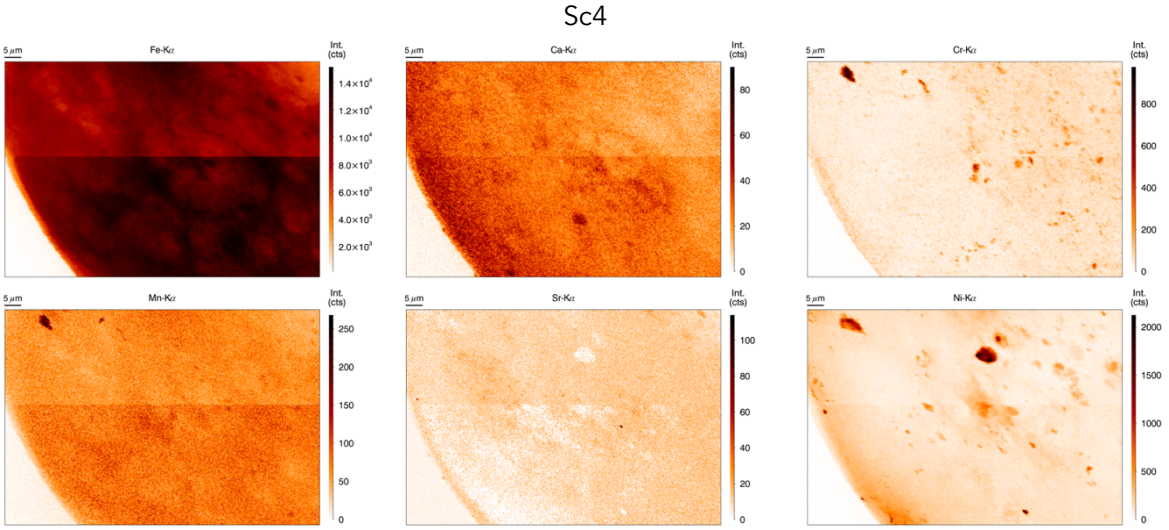

Figure 24: Most informative elemental maps constructed based on the data obtained at the ID16B beamline of the ESRF for sample Sc4. The intensity for every element is given in counts. The darker red, the higher the intensity of the element in that region. The increase in intensity about halfway the image is due to the refill during the measurement at the synchrotron facility.

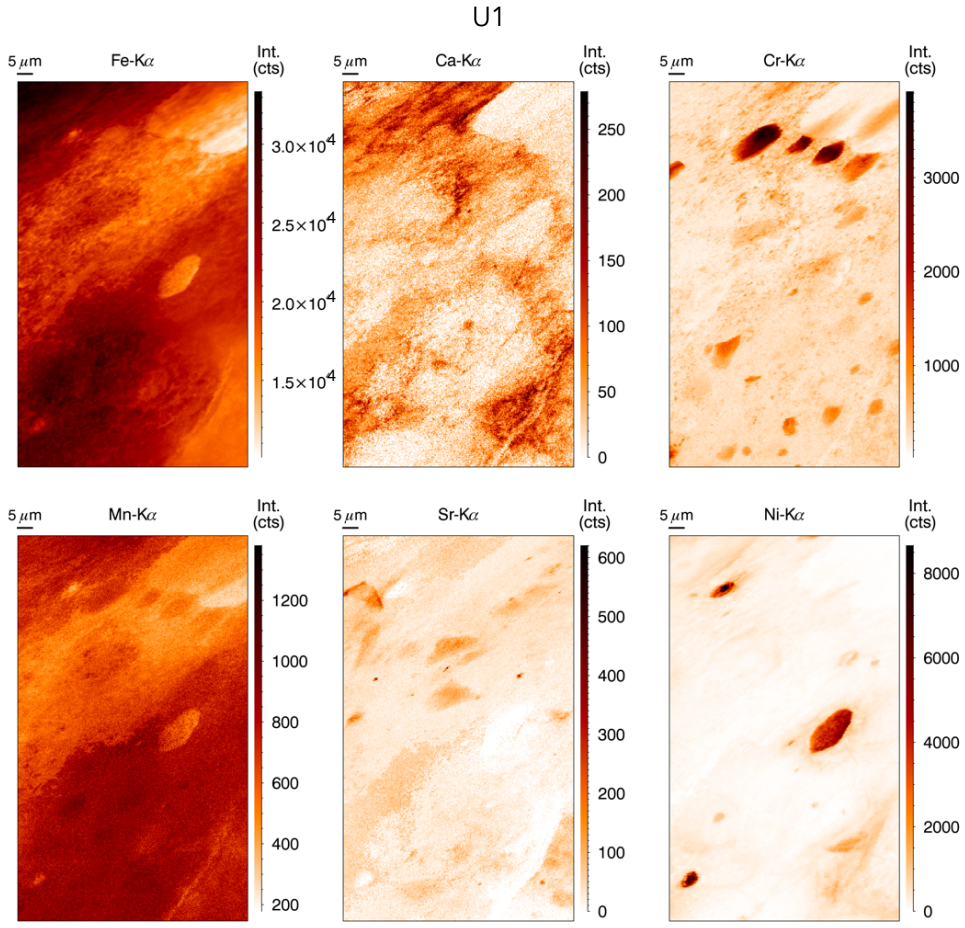

Figure 25: Most informative elemental maps constructed based on the data obtained at the ID16B beamline of the ESRF for sample U1. The intensity for every element is given in counts. The darker red, the higher the intensity of the element in that region.

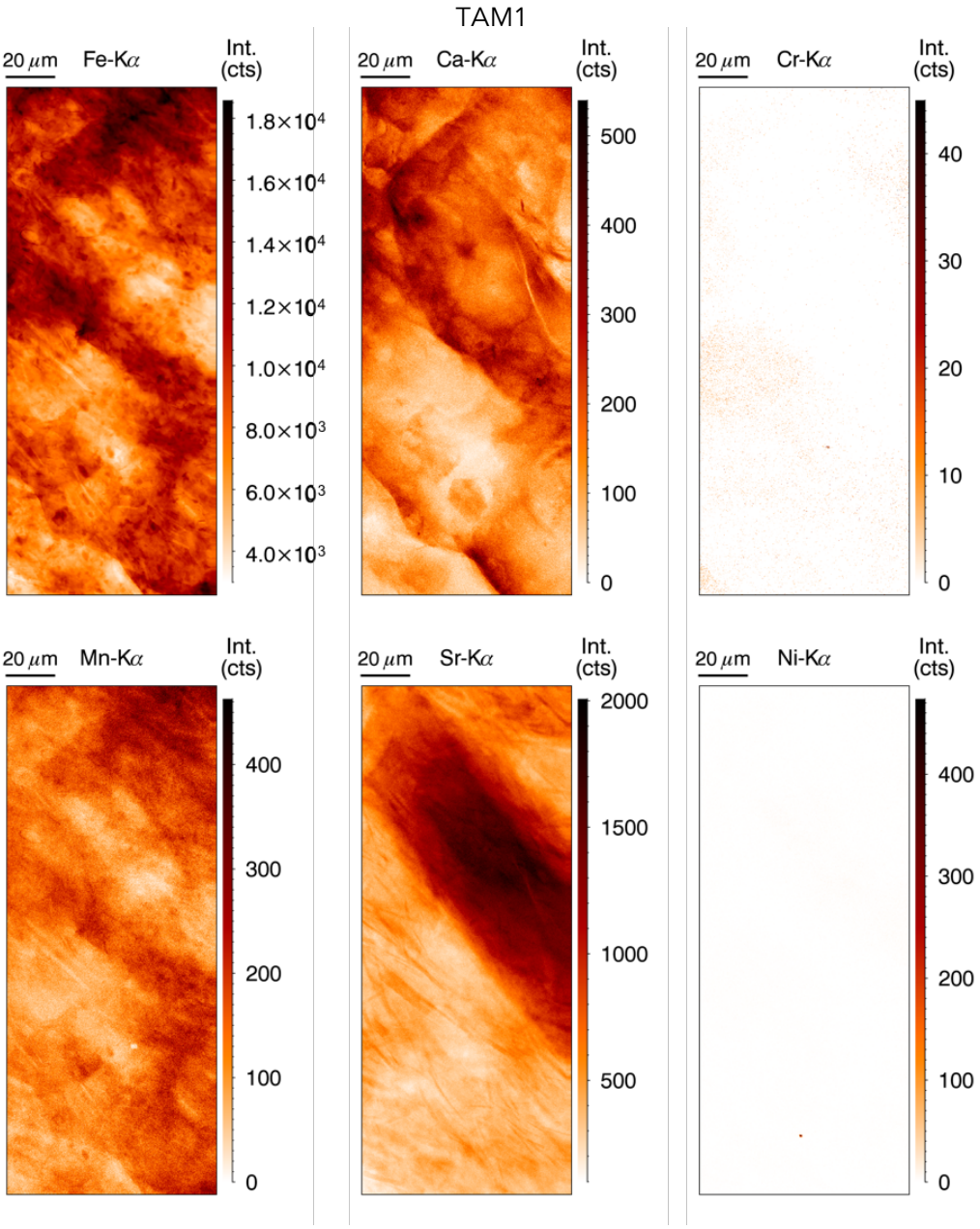

Figure 26: Most informative elemental maps constructed based on the data obtained at the ID16B beamline of the ESRF for sample TAM1. The intensity for every element is given in counts. The darker red, the higher the intensity of the element in that region.

TAM2

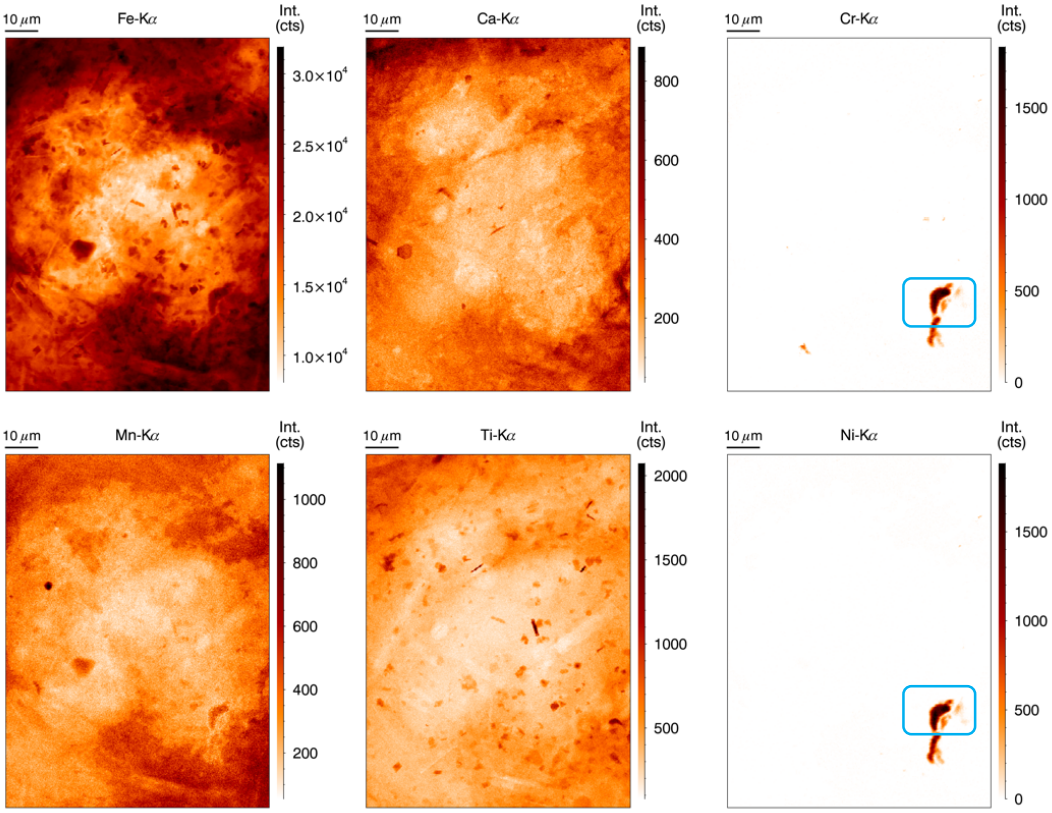

Figure 27: Most informative elemental maps constructed based on the data obtained at the ID16B beamline of the ESRF for sample TAM2. The intensity for every element is given in counts. The darker red, the higher the intensity of the element in that region. A detail of the area in the blue square is given in Figure 28.

Detail TAM2

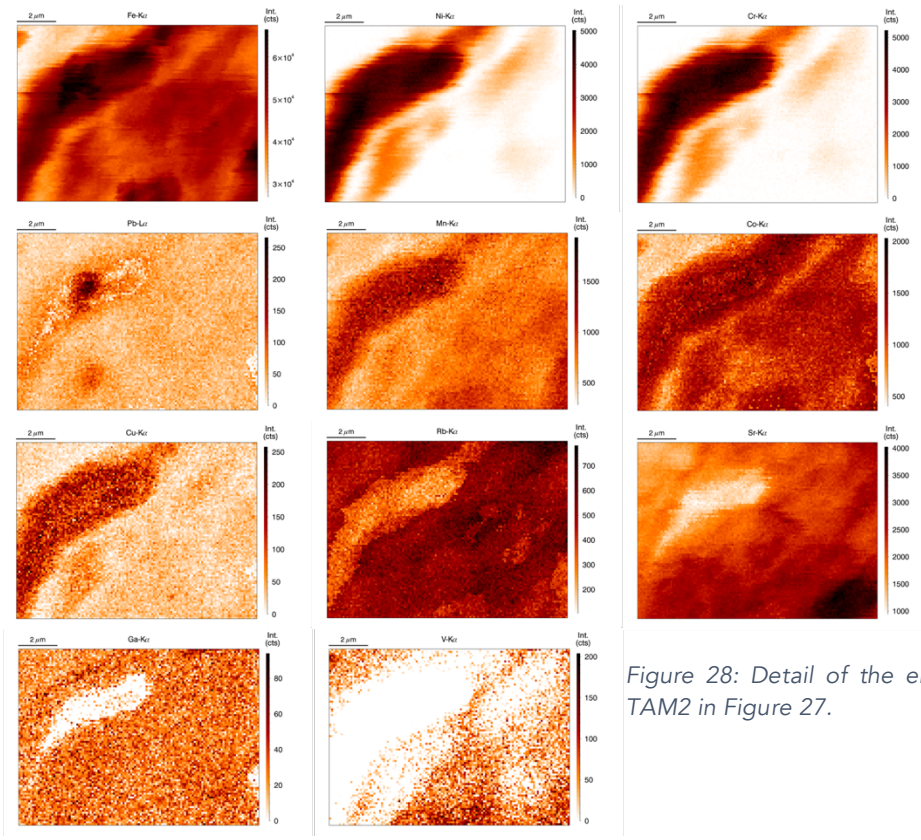

Figure 28: Detail of the elemental map of TAM2 in Figure 27.

With the fundamental parameter method, the concentrations of several elements have been computed for 8 samples (Sc2, Sc3, Sc4, TAM1, TAM2, U1, Uc2 and Uc3). These values are presented in Table 2. No XRF measurements are made on sample Uf2. The calculated concentration values confirm several of the qualitative observations. (i) First, the samples from the Transantarctic Mountains clearly differ from those from the Sør Rondane Mountains. (ii) Titanium and V have only been observed in the TAM samples. Furthermore, these samples contain very little to no Cr and Ni. (iii) The amount of Sr is at least two orders of magnitude higher than the concentrations in the Sør Rondane samples. (iv) Gallium and Y are only present in three samples and in relatively small amounts: in Sc3, TAM1 and TAM2 and in TAM1, TAM2 and Uc3, respectively. The concentration of Fe is high in all samples and varies between 0.15 and 78.86 wt%.

Table 2: Concentrations of the different elements for all samples. Ca, Ti, Mn and Fe are given in wt%, the other elements are given in ppm. These values were calculated using the fundamental parameter method. ND = not detected.

	Sc2	Sc3	Sc4	TAM1	TAM2	U1	Uc2	Uc3
Ca (wt%)	2.25	0.49	0.72	2.48	5.89	0.90	0.02	4.04
Ti (wt%)	ND	ND	ND	1.02	3.07	ND	ND	ND
V	ND	ND	ND	ND	334.62	ND	ND	ND
Cr	2390.39	422.69	260.65	ND	16.18	448.82	5.79	511.10
Mn (wt%)	0.64	0.12	0.04	0.04	0.12	0.11	ND	0.17
Fe (wt%)	78.86	11.34	13.48	4.95	16.81	9.08	0.15	26.68
Co	20887.94	2223.14	3551.74	1030.30	3867.25	3548.34	35.81	7433.74
Ni	25290.54	258.63	1860.37	ND	ND	982.59	17.02	9248.38
Cu	779.06	27.01	40.94	23.25	89.92	27.26	ND	164.04
Zn	427.60	25.47	53.15	76.57	369.76	37.52	ND	70.93
Ga	ND	1.95	ND	11.43	38.85	ND	ND	ND
Br	ND	2.22	79.98	ND	ND	ND	ND	ND
Rb	65.43	4.90	2.11	14.19	105.62	13.51	ND	12.99
Sr	31.04	6.24	ND	277.02	705.03	6.46	ND	12.21
Y	ND	ND	ND	7.53	38.63	ND	ND	1.52

4.4 Sectioned SRM particles

Five particles from the SRM collection (Sc2, Sc3, U1, Uc3 and Uf2) are polished and examined again using the SEM-EDS. The SEM images are shown in Figure 29. For every sample, several EDS spectra were obtained (Table 3). The locations of these spot analyses are marked by the green stars in Figure 29. Sample U1 is surrounded by a white dense rim with an average thickness of 5 µm (ranges from 2 – 47 µm). This rim is thicker (47 µm) at the top right corner and shown in more detail in Figure 29. It contains 78.11 % of FeO, the main constituent of magnetite. However,

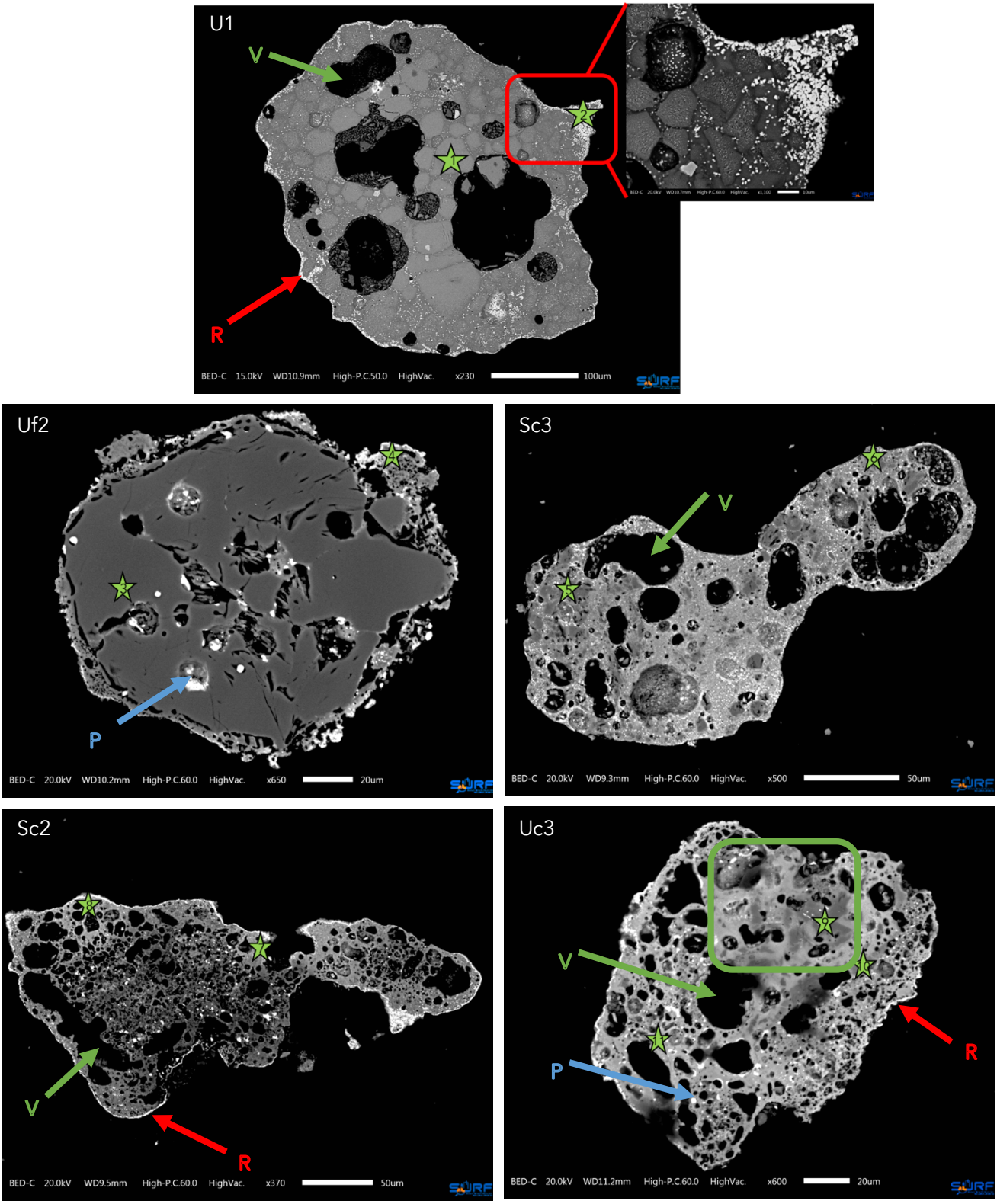

Figure 29: SEM images of sectioned particles. The green arrows mark vesicles (V) present in the samples. The red arrows point at the white, dense rim (R). The blue particles indicate the white, dense phases (P) in the particles. The red square marks the region of the detail from the rim in sample U1. The green square indicates the less vesicular region in sample Uc3. The green stars mark the locations where the EDS spectra presented in Table 3 were obtained.

this value is too low for pure magnetite. The rim also contains MgO (12.51 %) and SiO2 (4.75 %) (spectrum 2), and only minor amounts of other components. Inside the micrometeorite, individual crystals with an olivine ($(Mg,Fe)_2SiO_4$) composition (spectrum 1) can be recognised. The white material that makes up the rim, is also distributed along the edges of the crystals. Sample Uf2 consists of a uniform central part composed of Mg-rich olivine (forsterite) (spectrum 3) and a vesicular, denser outer rim which contains more FeO (spectrum 4). Also, Na_2O, a volatile element can be found in this rim. It ranges in thickness from 2 – 30 µm. Inside the central part, denser phases are present as inclusions. Sample Sc3 is a vesicular particle made up of a fine-grained matrix, consisting of mainly MgO and SiO_2 (spectrum 5) with several darker crystals. These darker crystals contain a lot of Al_2O_3 and MgO, the main components of spinel ($MgAl_2O_4$) (spectrum 6). Sample Sc2 is highly vesicular and surrounded by a white dense rim of varying thickness (0.5 – 20 µm). The white rim consists mainly of FeO (spectrum 7). The matrix contains MgO, SiO_2, SO_3 and FeO (spectrum 8). Sample Uc3 is a particle with vesicles except in the region in the green square. This region is also darker and contains a lot of Al_2O_3 (90.45 %) and CaO (8.01 %; spectrum 9). In spectrum 10, at the edge of the darker region MgO, SiO_2 and CaO are present. These oxides make the mineral diopside ($MgCaSi_2O_6$). On some points on the edge, a white rim can be observed. This rim is very thin (0.5 – 3 µm). Several brighter phases are also present, mainly near the vesicles. Spectrum 11 presents an overview of the composition of the matrix of sample Uc3.

Table 3: Overview of the oxides present in samples U1, Uf2, Sc2, Sc3 and Uc3 based on the spectra obtained with the SEM-EDS. The location of these spectra in the samples is given in Figure 29. All oxides are given in %. ND = not detected.

Spectrum	Na_2O	MgO	Al_2O_3	SiO_2	P_2O_5	SO_3	CaO	TiO_2	Cr_2O_3	MnO	FeO	NiO
1	ND	28.92	ND	36.71	ND	ND	ND	ND	ND	ND	34.37	ND
2	ND	12.51	1.92	4.75	ND	ND	0.96	ND	ND	0.60	78.11	1.15
3	ND	56.33	ND	42.28	ND	ND	0.35	ND	0.28	ND	0.77	ND
4	0.94	22.14	2.54	36.01	ND	ND	0.73	ND	0.53	0.47	34.78	1.86
5	ND	56.51	ND	42.11	ND	ND	ND	ND	0.41	0.42	0.56	ND
6	ND	28.05	69.38	0.68	ND	ND	ND	ND	ND	ND	1.89	ND
7	ND	6.54	1.71	0.59	ND	ND	ND	0.44	1.09	ND	88.98	0.65
8	ND	16.63	2.51	21.89	0.98	8.94	0.38	ND	0.77	ND	44.40	3.50
9	ND	0.35	90.45	ND	ND	ND	8.01	0.78	ND	ND	0.40	ND
10	ND	17.75	0.70	53.61	ND	ND	25.41	ND	ND	ND	2.53	ND
11	ND	22.37	2.40	33.74	ND	ND	7.00	ND	ND	ND	33.56	0.92

5. Discussion

5.1. Classification of the micrometeorites

The classification of micrometeorites from Genge et al. (2008) is mostly based on petrographic and mineralogical characteristics observed in BSE images of polished grain mounts of particles. Several parameters, such as the presence of a magnetite rim, mineralogy etc. have been used. Here, an attempt is made to determine several of these parameters in a non-destructive way in order to classify these particles. During the atmospheric entry process, dust particles often develop a magnetite rim due to surface melting and the oxidation of iron. This rim often varies in thickness and can be estimated from a single CT scan slice (0.5 – 10 μm). It can be recognized as a black layer on top of the particle using a stereomicroscope. In the SEM images (Figure 16) the rim can be identified as a dense, white layer and in the synchrotron CT scans (Figure 19) it occurs as a white layer that envelops the outer rim of the sample. Often this rim forms a barrier for the detection of minerals and phases closer to the centre of the micrometeorite. This is the case for the elemental maps reconstructed with the data from the Herakles instrument: most signals are obscured by the signal of Fe, which is present in large quantities in the outer magnetite rim (Figure 21). In the elemental maps obtained at the ID16B beamline, the signal is less obscured due to the higher spatial resolution but the signal intensity and XRF spectra are still influenced by the presence of the magnetite rim. According to the classification made by Genge et al. (2008), the presence of magnetite envelopes, is highly characteristic for scoriaceous micrometeorites, although it may still occur in unmelted micrometeorites as well. This observation also forms one of the main classification criteria during this study.

Vesicles are a common feature in micrometeorites due to degassing of volatile components (Genge, 2017). Their relative abundance is commonly used to discriminate between scoriaceous and unmelted micrometeorites (Genge et al., 2008). The abundance of vesicles in scoriaceous micrometeorites is usually high and can even reach more than 50 % in volume. Unmelted micrometeorites contain less vesicles. Three groups have been proposed based on the percentage of vesicles in the samples (Table 1). The first group, with less than 9 vol% vesicles, consists of truly unmelted micrometeorites. The second group, with more than 19 vol% vesicles, contains scoriaceous micrometeorites. The intermediate group, with a porosity between 10 and 15 vol%, comprises samples of an intermediate type, i.e. between scoriaceous and unmelted.

The chemical compositions of the samples, calculated from the synchrotron XRF data with the fundamental parameter method, can be normalised to the composition of Ivuna-type (CI-type) carbonaceous chondrites (Lodders, 2003). The samples from the SRM collection are presented in Figure 30, the samples from the TAM collection in Figure 31 using various colours and symbols. Most micrometeorites show some resemblance to the CI chondrites for different elements including Ca, Cr, Mn, Fe, Ni, Cu, Zn, Ga, Rb, Sr, Y. Every micrometeorite, from both collections,

contains high amounts of Co, but this is likely due to spectral overlap of the peaks of Fe and Co. For this reason, Co is excluded from the graphs in Figure 30 and Figure 31. The samples from the TAM collection display strong deviation for the following elements: Ti, C, Rb, Sr and Y are clearly enriched relative to CI chondrites and the samples of the SRM collection. Conversely, the TAM samples also appear strongly depleted in Cr. The curve for sample Uc2 shows approximately the same shape as the other curves for the SRM samples but it is strongly depleted in all elements relative to CI. Part of this sample broke off prior to the XRF analysis and thus the calculated concentrations do not correspond to the determined volume of this sample. The other samples from the SRM collection are generally chondritic with exception of the following elements. Samples Uc3 and Sc2 exhibit a slight enrichment in Ca. Samples Sc4, Sc3, U1 and Uc3 are depleted in Cr. Sample Sc2 is enriched in Mn, Fe, Ni, Cu, Rb and Sr. Samples Sc3 and U1 are highly depleted in Ni, Cu and Zn. The composition of the CM type chondrites was also added to the plot and normalised to the CI type composition in order to compare the samples to the CM type chondrites. Most SRM particles show the same trend for Ca, Rb, Sr and Y, but they are more enriched in Fe. They are also depleted in Ni, Cr and Mn compared to CM chondrites, as was previously observed by Genge et al. (1997). The TAM particles do not follow the same trend as the CM chondrites.

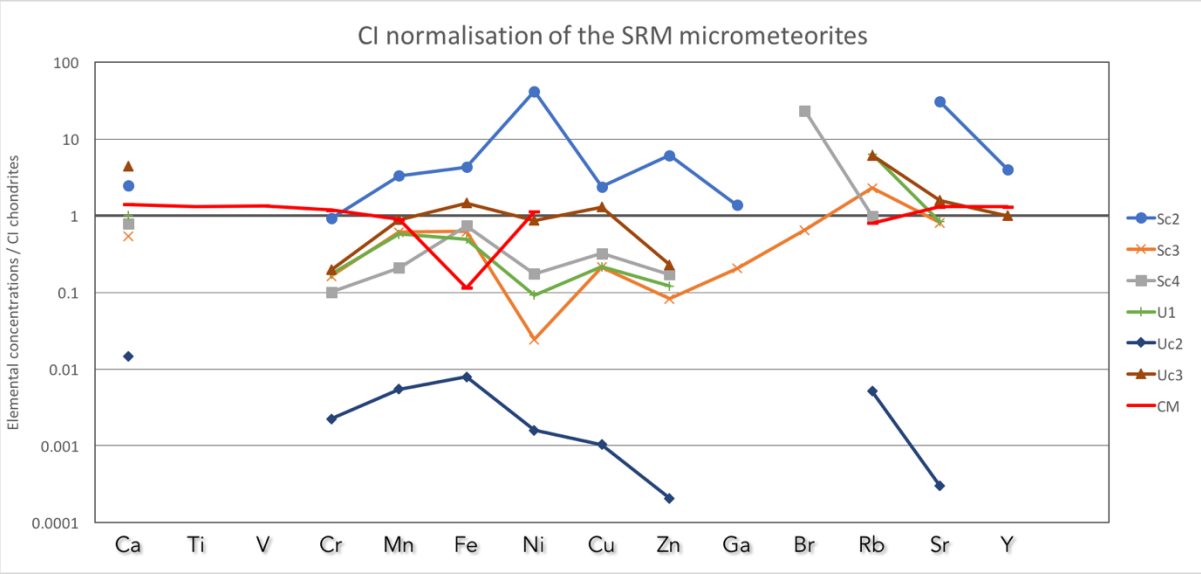

Figure 30: Abundances of the elements in the samples from the SRM collection normalised to the values of the CI chondrites (Lodder, 2003). The curves for the different samples are given in different colours and with a different symbol. If values were not detected in the sample, they were omitted from the graph. The CM composition (Hutchison, 2004) has also been normalised to the values of the CI chondrites and is given in red.

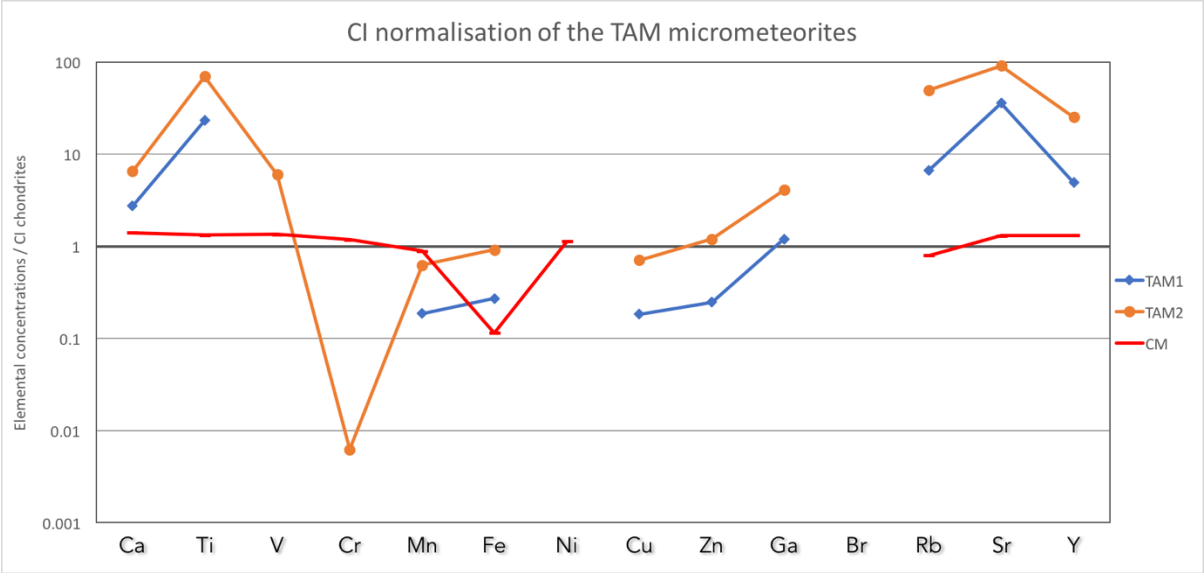

Figure 31: Abundances of the elements in the samples from the TAM collection normalised to the values of the CI chondrites (Lodder, 2003). The curves for the different samples are given in different colours and with a different symbol. If values were not detected in the sample, they were omitted from the graph. The CM composition (Hutchison, 2004) has also been normalised to the values of the CI chondrites and is given in red.

Based on the observations made in the CT scans and the chemical composition, the studied samples have been divided into two groups: scoriaceous or unmelted (Table 4). Particles that were sectioned and examined with the SEM-EDS can be classified further into fine- or coarse-grained unmelted micrometeorites and for the scoriaceous particles a fine-grained matrix could be identified. Samples are considered to be chondritic in composition if the average of their normalised values does not deviate from CI chondrites by a factor of more than 5. The scoriaceous group is comprised of samples with a high percentage of vesicles (more than 14.6 %) and no individual crystals. The unmelted group contains samples with a low percentage of vesicles (less than 13.2 %) and individually recognisable crystals (10 – 150 μm).

Table 4: Classification criteria and proposed class of all studied samples. NR = not representative, C = coarse-grained, F = fine-grained, FM = fine-grained matrix.

Sample	Diameter (µm)	Magnetite rim	Vesicles (vol%)	Individual crystals	Chemical composition	Class
Sc2	185	Yes, non-uniform	8.9	No	Non-chondritic	Unmelted (F)
Sc3	152	No	23.3	No	Chondritic	Scoriaceous (FM)
Sc4	138	Yes, uniform	19.8	No	Chondritic	Scoriaceous
TAM1	350	No	11.7	Yes (50 – 150 µm)	Non-chondritic	Unmelted
TAM2	304	No	22.8	Yes (10 – 30 µm)	Non-chondritic	Scoriaceous
U1	408	Yes, uniform	13.2	Yes (20 – 50 µm)	Chondritic	Unmelted (C)
Uc2	170	Yes, non-uniform	11.1	No	Chondritic	Unmelted
Uc3	142	Yes, non-uniform	14.6	No	Chondritic	Scoriaceous (FM)
Uf2	144	Yes, non-uniform	8.7	Yes (10 – 140 µm)	NR	Unmelted (C)

5.2. Comparison between the TAM and SRM collections

The samples from the two different collections show distinct differences in chemical composition (Figure 23 - Figure 27). The micrometeorites from the Transantarctic Mountains contain little to no Ni or Cr, but are enriched in Sr and Ti. In contrast, the samples from the Sør Rondane Mountains are characterised by distinct enrichments in Ni and Cr, but lower concentrations of Sr and Ti. A possible explanation for these chemical differences can be attributed to local weathering processes. On Antarctica, the environmental conditions are generally constant (i.e. cold and dry) with little to no effects of chemical weathering. However, a number of meteorites have been found on Antarctica that clearly show evidence of weathering (Bland et al., 2006). Overall, weathering processes are characterised by the enrichment of Sr and Ba and concurrent depletion in Ni and S in chondritic materials. These elements are generally mobile in the Antarctic environment. Several factors influence the degree of weathering: (i) the primary composition of the micrometeorite and containing mineral phases with distinct crystal structures; (ii) the nature of the secondary oxidation products; (iii) the degree of porosity or fracturing; and (iv) the exposure time. According to the observations made by Bland et al. (2006), Antarctic meteorites contain little to no magnetite. If magnetite is present it is not as a magnetite rim as observed in micrometeorites. This is an important difference compared to micrometeorites, which contain a clearly discernible magnetite rim as the result of the oxidation of metallic Fe during atmospheric passage. Although this magnetite is not the result of alteration in the Antarctic environment, it does help preserve the

internal structure and mineralogy of the original body. Carbonaceous chondrites are more susceptible to terrestrial weathering than other meteorite types (Bland et al., 2006). A large variability in Br abundances was observed and the organic matter in the meteorites suffers from large effects of weathering. This also means that the Antarctic collections may not be as pristine as previously considered. Van Ginneken et al. (2016) previously studied the weathering of Antarctic micrometeorites (mostly cosmic spherules) and reached the following conclusions. First of all, the main weathering effects include formation of irregular and faceted cavities, etch pits in olivine crystals, infilled cavities, replaced silicate phases and hydrated and replaced metal. Secondly, a weathering scale was established in combination with the level of encrustation. From these observations, it became evident that the TAM particles examined during this study experienced chemical changes during their terrestrial residence. While SiO_2, MgO, FeO and CaO are progressively lost, TiO_2 becomes enriched. This is consistent with the observed Ti enrichment in TAM1 and TAM2.

The exposure time of the two collections sampled for this study is different: Frontier Mountain in the Transantarctic Mountains has an exposure age of 4.4 Ma (Rochette et al., 2008), while the Sør Rondane Mountains have an exposure age of 1.9 Ma (Suganuma et al., 2014; Goderis et al., forthcoming). Consequently, it is highly likely that the samples from the TAM collection experienced a longer residence time and have thus been exposed to the Antarctic environment for a longer period of time. Another important factor that may influence the weathering of the samples are the environmental factors. Depending on where the sample ended up on Antarctica, it will weather differently. For the TAM collection, weathering effects have already been studied thoroughly (van Ginneken et al., 2017b), but not yet for the SRM collection. These differences in terrestrial age and weathering environment may have caused the enrichment in Sr and Ti in the TAM samples and the lack of Cr and Ni. While terrestrial weathering may alter several properties of micrometeorites found on Earth, the results of this study are important, as Antarctic weathering processes may serve as an analogue for aqueous alteration processes on asteroids. The alteration products formed during both processes and behaviour of organic material is similar (Bland et al., 2006).

5.3. Comparison to the micrometeorite parent body material

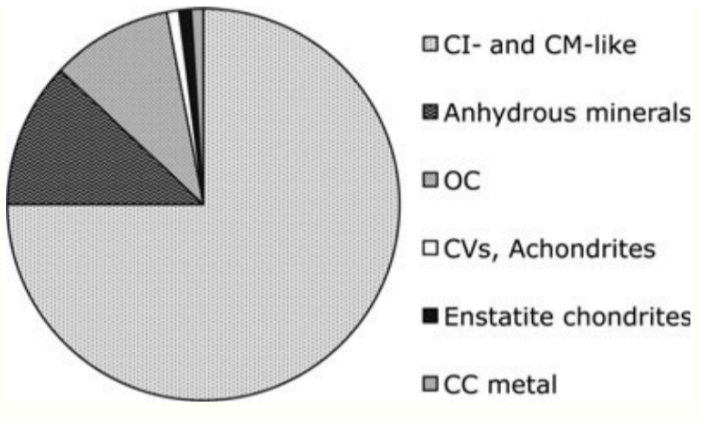

Figure 32: Estimate of different sources for micrometeorites based on petrographic features. Fine-grained CI-, CM-like material forms the origin for 75 % of the micrometeorites. Anhydrous minerals make up 10 – 15 % and may come from different chondrites. The ordinary chondrites account for ≤ 10 %. CV's, achondrites, enstatite chondrites and metal from chondrites form only a minor fraction (1 %) (Taylor et al., 2012).

One of the major issues considering micrometeorites, is the identification of the parent body or precursor material because of the small size and textural and chemical alterations during atmospheric entry. The general consensus is that up to 99 % of all micrometeorites originate from carbonaceous chondrites. According to Taylor et al. (2012), fine-grained CI and CM-like material, two types of carbonaceous chondrites, makes up the largest fraction of precursors for micrometeorites, representing about 75 % (Figure 32). Based on oxygen isotope ratios, the CM/CO type chondrites are the best option as parent material and the CI type chondrites are rather rare, similar to meteorites (Suavet et al., 2010). Carbonaceous chondrites are fragments from the most primitive asteroids known in the Solar System and might even originate at the edges of our Solar System. Often, these materials have experienced varying degrees of aqueous alteration. CI-type meteorites do not contain any recognizable chondrule, are very fragile and porous (up to 30%) and consist of fine-grained minerals including olivine, orthopyroxene, clinopyroxene and magnetite. Their water content ranges between 17 and 22 wt%. CM type meteorites contain a number of olivine-rich chondrules in a matrix with a chemical composition broadly similar to CI meteorites (Weisberg et al., 2006).

The porosities of different meteorite types have been studied by Britt and Consolmagno S. J. (2003). For CI type meteorites, the average porosity approximates 11.3 %, while CM type meteorites display average porosity levels of 23 %. When using these values, it is important to bear in mind that only few samples of these meteorites are available on which these values are based (9 CI chondrites and 587 CM chondrites). Another thing to consider is the fact that vesicularity in micrometeorites is mainly a function of degassing and volatile loss during atmospheric entry. In order to determine the original porosity, a good understanding of volatile loss is required. For cosmic spherules, this has been done by studying isotope variability in chemical elements such as Fe, K, Cr, etc. (Engrand et al., 2005) and based on the Si/Al and Mg/Al ratios (Taylor et al., 2005). There might be some resemblance in the values between the determined porosities in the micrometeorites and the known porosities of potential parent bodies. The second group, with a porosity between 11 and 15 %, could be linked to CI type meteorites. This is highly unlikely based on oxygen isotope ratios. The third group with a porosity

of more than 19 %, matches the values observed in CM type meteorites. The resemblance to CI type chondrites is highly unlikely based on oxygen isotope ratios. Even though there are some similarities, the comparison of porosities is not conclusive to identify the parent body. The processes responsible for vesicle formation in asteroids are not similar to the vaporisation in micrometeorites. Furthermore, at such a small scale, the porosity of the parent body is not preserved or representative (Genge, 2017). These values can only be used to estimate the volatile loss during atmospheric entry and determine the porosity and potential volatile and water content before atmospheric entry.

Another way to try and identify the parent body is by looking at element ratios of refractory elements that should not be altered much during atmospheric entry. One of these ratios is the Cr/Mn ratio. For CI chondrites, this is 1.35 ± 1, for CM chondrites 2.2 ± 0.5. When comparing these values to the ratios in the samples studied here (Table 5), there is an overlap with CI chondrites in the uncertainty range. However, this is not conclusive. The ratios range from 0 to 0.75 and are thus significantly smaller than in either CI or CM chondrites.

Table 5: Cr/Mn ratio for the samples studied here. ND = not determined.

	Sc2	Sc3	Sc4	TAM1	TAM2	U1	Uc2	Uc3
Cr/Mn	0.38	0.33	0.75	ND	ND	0.34	ND	0.29

Determining the parent material remains one of the more difficult tasks, and requires a lot of additional information in order to be certain of a statement. The XRD data may contribute to this challenge or the bulk oxygen isotopic composition could be determined. The oxygen isotope signature can be used to link the micrometeorites to one of four groups of parent material (Suavet et al., 2010; van Ginneken et al., 2017a). It is important to consider that this method is destructive.

5.4. Comparison to the NASA Stardust mission

The NASA stardust mission to comet Wild-2 brought back interstellar dust samples imbedded in an aerogel. In a first stage, the Stardust Interstellar Preliminary Examination (ISPE) , these samples have been analysed using XRF at synchrotron facilities (Brenker et al., 2014; Flynn et al., 2014; Simionovici et al., 2014). The main limitation for XRF analysis was the lack of sensitivity for major rock-forming elements (e.g., C, O, Mg, Al, Si, S and Fe), as this technique was only sensitive to S

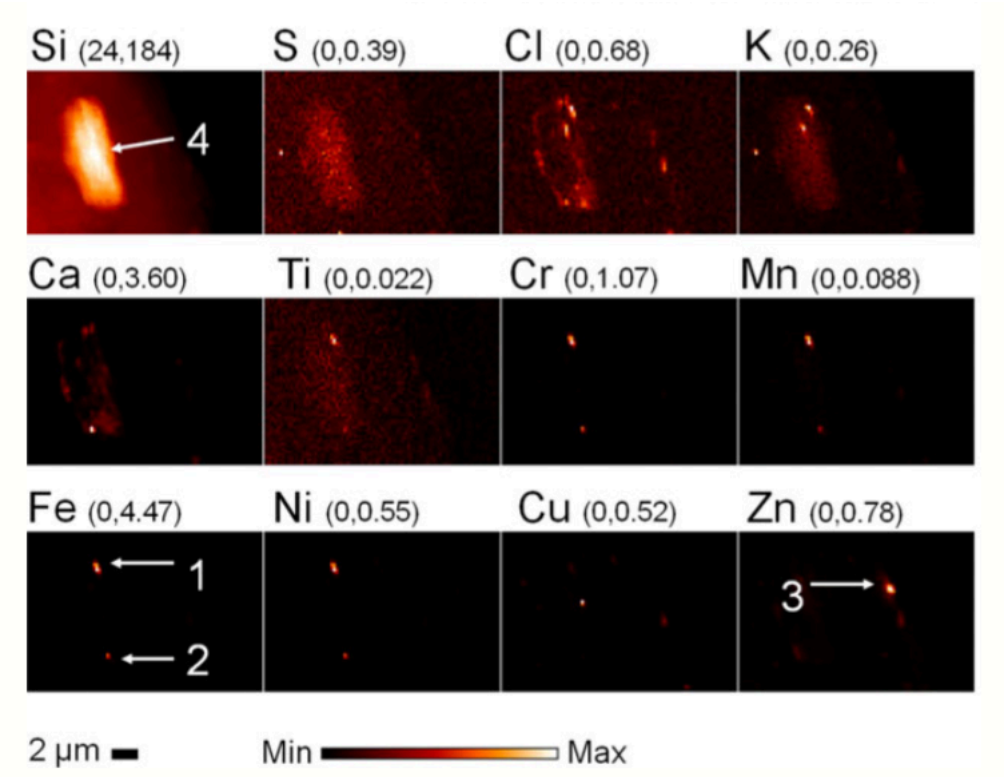

Figure 33: Elemental maps of interstellar candidate I1001,1,16 with a Si-rich region at the surface. This region contains three elemental hotspots: two rich in Fe, Ni, Mn and Cr and one rich in Zn. Values in parentheses are the minimum and maximum µg cm^{-2} used in applying the colour scale bar (Flynn et al., 2014).

and Fe due to the fluorescence of Si in the aerogel. For several particles, elemental maps were constructed (Figure 33). Due to the absence of a magnetite rim in these particles, less Fe is present compared to micrometeorites that entered the atmosphere. Significantly high amounts of Si have been found in Stardust samples. This has not been measured in the micrometeorites but is an interesting feature to investigate further. The samples do contain Mn, Cr and Ni hotspots similar to those found in the micrometeorite samples from the SRM collection. Based on XRD and XRF measurements forsterite, spinel and an Fe-bearing phase were identified in sample Orion. With the same techniques, sample Sirius has been observed to be highly altered (Flynn et al., 2014). Comparing micrometeorites found on Earth to interstellar dust particles may help to link these particles and identify their source regions in the Solar System.

5.5. Evaluation of the analytical techniques

One of the goals of this study was to create a set of non-destructive analytical tools for the analysis of micrometeorites. The original idea was to obtain structural, chemical and mineralogical information from the particles. However, the mineralogical information from the XRD analyses is not available yet. Nevertheless, the CT imaging and XRF analysis at high-resolution has proven to be highly useful. It is expected that the XRD data will only attribute to this workflow and provide a way to link the mineralogical and chemical data. Currently only 9 samples from the 2 sample locations have been analysed following the aforementioned protocol, which excludes statistical representativeness. If more samples were to be studied using this protocol, numerical constraints could be imposed for the classification of the micrometeorites regarding their porosity and chemical composition. This set of tools, especially XRF, CT and XRD, would also be useful for the study of interstellar dust particles brought back from ongoing and future space missions. If all samples would be treated in the same way, it makes the data more accessible for comparison.

In order to evaluate if this method is adequate, the samples were cut open and analysed with the SEM at the Vrije Universiteit Brussel. In the cross sections (Figure 29), more details and smaller structures can be distinguished than on the CT scans. However, large structures (> 10 μm), like the igneous rim in sample Uf2, the individual crystals in sample U1, the magnetite rim and vesicles in all particles, can already be recognised in the CT scans (Figure 19). This means that the CT scans provide the opportunity to characterise these larger structures (>10 μm) without destroying the samples and provide a first impression of what to expect from the micrometeorite. For fine-grained particles, CT scans are not as clear. It is more difficult to identify crystals or structures. If more detail or a more thorough understanding of the internal structure is needed, polishing the samples and examining them with the SEM-EDS is recommended. Chemical information was also obtained with the SEM-EDS. This is given in oxide% so the mineralogy could be derived from these values. This is not (yet) possible with the set of tools presented here, but the XRD data should give more clarity on this. Again, it is expected that the SEM-EDS will assess this in more detail and the XRD would just provide a primary assessment of the mineral phases present in the samples.

6. Conclusion

The primary goal of this dissertation was to come up with a set of analytical tools to characterise micrometeorites in a non-destructive way. Preferably, structural, chemical and mineralogical properties would be determined in order to provide a complete picture of the samples. To achieve this, the micrometeorites were examined at the ID16B beamline at the ESRF where synchrotron-based X-ray analysis is possible at the nanoscale, combining X-ray fluorescence (XRF), X-ray diffraction (XRD) and computed tomography (CT). Several problems are encountered when examining these samples in a laboratory-based setup, like the size of the samples and the presence of a magnetite rim. At the ID16B beamline these problems were largely solved. Firstly, the high resolution of 50 nm is more than sufficient to image the micrometeorites in detail despite their relatively small size. Secondly, the use of the pink beam mode at 17.5 keV allowed to measure beyond the magnetite rim. Consequently, XRF, XRD and CT data was collected at the ESRF for 9 samples, 2 from the Transantarctic mountains and 7 from the Sør Rondane mountains. Results from the XRD measurements are not yet available due to unforeseen circumstances, but the XRF and CT data are presented in this work. The CT images allow the identification of large structures (>10 μm), like crystals, vesicles, a magnetite rim and an igneous rim. The XRF measurements provide elemental maps, which give information regarding the distribution of chemical elements, and the possibility to quantify the chemical composition. Here, this quantification was carried out using the fundamental parameter method. In the future, this may be upgraded to Monte Carlo simulations, which is more precise and takes into account more parameters. The results of both techniques can be used to classify the micrometeorites in the known classes as established from Genge et al. (2008).

The obtained results may even help to update the classification criteria, which was the second goal for this study, if more samples are analysed in the aforementioned way and values are statistically valid. The porosity could be determined based on the CT scans and an absolute constraint could be established for the number of vesicles in scoriaceous and unmelted micrometeorites. The same applies for the chemical composition. The abundances can be used to determine to which class the samples belong, although caution is advised since the chemical composition may change during atmospheric entry and during the terrestrial residence due to weathering processes.

The final goal was to compare the samples from the two different collections, i.e. the SRM and TAM collection. This has revealed distinct differences in chemical composition which may be attributed to weathering processes. These processes depend on the terrestrial age, which is different for both collections, and on environmental conditions in and around the trap. This has resulted in an enrichment in Sr and Ti and a depletion in Cr and Ni. These two characteristics are not observed for the samples from the SRM. In previous work, it was generally assumed that the Antarctic collections are pristine and do not exhibit terrestrial alteration effects. But here, there is a clear effect of the Antarctic environment on the samples and this should be taken into account for chemical analyses of samples from all collections retrieved at Antarctica. Since the Antarctic

weathering processes may form an analogue for aqueous alteration processes on asteroids, studying weathering on Earth can help understand the latter.
In addition to the original objectives, the results were also compared to parent body material and samples from the NASA stardust mission. Based on the obtained results, it still remains difficult to link the micrometeorites to a certain type of parent body. The porosities and chemical composition are not sufficient to appoint a definite parent material. More data is necessary such as oxygen isotopes and perhaps the XRD data will also help to refine this. The comparison with the Stardust samples showed that there might be some similarities between the two in terms of chemical composition. However, analysing these particles in the same way may allow a better comparison and help to identify their source regions in the Solar System. The main difference is the presence of a magnetite rim in the micrometeorites which is clear from the Fe content.

The applied set of tools has proven to be adequate for a first characterisation and classification of the samples. However, if more detail is needed, additional methods are required that may be destructive. For example, in this study five particles from the SRM collection were polished and examined with the SEM-EDS. This revealed previously unresolved smaller structures and provided a mineralogical composition.

The applied methodology may be improved in the future by a number of adjustments. If the spatial resolution in CT scanning improves, smaller structures could be recognised and used for the classification. The XRD measurements should be further analysed in order to assess their contribution to the method. If the measurements were to be conducted in vacuum conditions, more elements could be measured, including Mg, Al, Si, but this not feasible yet for a synchrotron setup. The five particles which have been polished and examined with SEM-EDS, are highly promising and will be examined further using different tools including secondary ion mass spectrometry (SIMS) or sensitive high-resolution ion microprobe (SHRIMP) to determine the triple-oxygen isotopic composition of the samples and use this information to identify potential source regions in the Solar System.

7. Bibliography

Akulov, N.I., Pavlova, L.A., Antipin, E. V., 2014. Geochemical peculiarities of micrometeorites in bottom sediments of Lake Baikal. Dokl. Earth Sci. 454, 193–198. doi:10.1134/S1028334X14020184

Badjukov, D.D., Brandstätter, F., Raitala, J., Kurat, G., 2010. Basaltic micrometeorites from the Novaya Zemlya glacier. Meteorit. Planet. Sci. 45, 1502–1512. doi:10.1111/j.1945-5100.2010.01125.x

Baruchel, J., Buffiere, J.Y., Cloetens, P., Di Michiel, M., Ferrie, E., Ludwig, W., Maire, E., Salvo, L., 2006. Advances in synchrotron radiation microtomography. Scr. Mater. 55, 41–46. doi:10.1016/j.scriptamat.2006.02.012

Beckhoff, B., Kanngießer, B., Wolff, H., Langhoff, N., Wedell, W., 2006. Handbook of Practical X-Ray Fluorescence Analysis, New York. doi:10.1007/978-3-540-36722-2

Bland, P.A., Zolensky, M.E., Benedix, G.K., Sephton, M.A., 2006. Weathering of Chondritic Meteorites, in: Meteorites and the Early Solar System II. pp. 853–867.

Brabant, L., Vlassenbroeck, J., De Witte, Y., Cnudde, V., Boone, M.N., Dewanckele, J., Van Hoorebeke, L., 2011. Three-Dimensional Analysis of High-Resolution X-Ray Computed Tomography Data with Morpho+. Microsc. Microanal. 17, 252–263. doi:10.1017/S1431927610094389

Brenker, F.E., Westphal, A.J., Vincze, L., Burghammer, M., Schmitz, S., Schoonjans, T., Silversmit, G., Vekemans, B., Allen, C., Anderson, D., Ansari, A., Bajt, S., Bastien, R.K., Bassim, N., Bechtel, H.A., Borg, J., Bridges, J., Brownlee, D.E., Burchell, M., Butterworth, A.L., Changela, H., Cloetens, P., Davis, A.M., Doll, R., Floss, C., Flynn, G., Fougeray, P., Frank, D.R., Gainsforth, Z., Grün, E., Heck, P.R., Hillier, J.K., Hoppe, P., Hudson, B., Huth, J., Hvide, B., Kearsley, A., King, A.J., Lai, B., Leitner, J., Lemelle, L., Leroux, H., Leonard, A., Lettieri, R., Marchant, W., Nittler, L.R., Ogliore, R., Ong, W.J., Postberg, F., Price, M.C., Sandford, S.A., Tresseras, J.A.S., Simionovici, A.S., Solé, V.A., Srama, R., Stadermann, F., Stephan, T., Sterken, V.J., Stodolna, J., Stroud, R.M., Sutton, S., Trieloff, M., Tsou, P., Tsuchiyama, A., Tyliszczak, T., Von Korff, J., Wordsworth, N., Zevin, D., Zolensky, M.E., 2014. Stardust interstellar preliminary examination V: XRF analyses of interstellar dust candidates at ESRF ID13. Meteorit. Planet. Sci. 49, 1594–1611. doi:10.1111/maps.12206

Britt, D.T., Consolmagno, S.J.G.J., 2003. Stony meteorite porosities and densities : A review of the data through 2001. Meteorit. Planet. Sci. 38, 1161–1180.

Cnudde, V., Boone, M.N., 2013. High-resolution X-ray computed tomography in geosciences: A review of the current technology and applications. Earth-Science Rev. 123, 1–17. doi:10.1016/j.earscirev.2013.04.003

Cordier, C., Folco, L., Suavet, C., Sonzogni, C., Rochette, P., 2011. Major, trace element and oxygen isotope study of glass cosmic spherules of chondritic composition: The record of their source material and atmospheric entry heating. Geochim. Cosmochim. Acta 75, 5203–5218. doi:10.1016/j.gca.2011.06.014

Dobrică, E., Engrand, C., Duprat, J., Gounelle, M., Leroux, H., Quirico, E., Rouzaud, J.N., 2009. Connection between micrometeorites and Wild 2 particles: From Antarctic snow to cometary ices. Meteorit. Planet. Sci. 44, 1643–1661. doi:10.1111/j.1945-5100.2009.tb01196.x

Duprat, J., Dobrică, E., Engrand, C., Aléon, J., Marrocchi, Y., Mostefaoui, S., Meibom, A., Leroux, H., Rouzaud, J.N., Gounelle, M., Robert, F., 2010. Extreme Deuterium Excesses in Ultracarbonaceous Micrometeorites from Central Antarctic Snow. Science (80-.). 328, 742–745.

Duprat, J., Engrand, C., Maurette, M., Kurat, G., Gounelle, M., Hammer, C., 2007. Micrometeorites from Central Antarctic snow: The CONCORDIA collection. Adv. Sp. Res. 39, 605–611. doi:10.1016/j.asr.2006.05.029

Engrand, C., Deloule, E., Robert, F., Maurette, M., Kurat, G., 1999. Extraterrestrial water in micrometeorites and cosmic spherules from Antarctica: An ion microprobe study. Meteorit. Planet. Sci. 34, 773–786. doi:10.1111/j.1945-5100.1999.tb01390.x

Engrand, C., McKeegan, K.D., Leshin, L.A., Herzog, G.F., Schnabel, C., Nyquist, L.E., Brownlee, D.E., 2005. Isotopic compositions of oxygen, iron, chromium, and nickel in cosmic spherules: Toward a better comprehension of atmospheric entry heating effects. Geochim. Cosmochim. Acta 69, 5365–5385. doi:10.1016/j.gca.2005.07.002

Flynn, G.J., Sutton, S.R., Lai, B., Wirick, S., Allen, C., Anderson, D., Ansari, A., Bajt, S., Bastien, R.K., Bassim, N., Bechtel, H.A., Borg, J., Brenker, F.E., Bridges, J., Brownlee, D.E., Burchell, M., Burghammer, M., Butterworth, A.L., Changela, H., Cloetens, P., Davis, A.M., Doll, R., Floss, C., Frank, D., Gainsforth, Z., Grün, E., Heck, P.R., Hillier, J.K., Hoppe, P., Hudson, B., Huth, J., Hvide, B., Kearsley, A., King, A.J., Leitner, J., Lemelle, L., Leroux, H., Leonard, A., Lettieri, R., Marchant, W., Nittler, L.R., Ogliore, R., Ong, W.J., Postberg, F., Price, M.C., Sandford, S.A., Tresseras, J.A.S., Schmitz, S., Schoonjans, T., Silversmit, G., Simionovici, A., Solé, V.A., Srama, R., Stadermann, F.J., Stephan, T., Sterken, V., Stodolna, J., Stroud, R.M., Trieloff, M., Tsou, P., Tsuchiyama, A., Tyliszczak, T., Vekemans, B., Vincze, L., Von Korff, J., Westphal, A.J., Wordsworth, N., Zevin, D., Zolensky, M.E., 2014. Stardust interstellar preliminary examination VII: Synchrotron X-ray fluorescence analysis of six Stardust interstellar candidates measured with the Advanced Photon Source 2-ID-D microprobe. Meteorit. Planet. Sci. 49, 1626–1644. doi:10.1111/maps.12144

Folco, L., Cordier, C., 2015. Micrometeorites. EMU Notes Mineral. 15, 253–297. doi:10.1180/EMU-notes.15.9

Folco, L., D'Orazio, M., Tiepolo, M., Tonarini, S., Ottolini, L., Perchiazzi, N., Rochette, P., Glass, B.P., 2009. Transantarctic Mountain microtektites: Geochemical affinity with Australasian microtektites. Geochim. Cosmochim. Acta 73, 3694–3722. doi:10.1016/j.gca.2009.03.021

Genge, M.J., 2017. An increased abundance of micrometeorites on Earth owing to vesicular parachutes. Geophys. Res. Lett. 44, 1679–1686. doi:10.1002/2016GL072490

Genge, M.J., 2006. Igneous rims on micrometeorites. Geochim. Cosmochim. Acta 70, 2603–2621. doi:10.1016/j.gca.2006.02.005

Genge, M.J., Engrand, C., Gounelle, M., Taylor, S., 2008. The classification of micrometeorites 515, 497–515.

Genge, M.J., Gileski, a., Grady, M.M., 2005. Chondrules in Antarctic micrometeorites 238, 225–238. doi:10.1111/j.1945-5100.2005.tb00377.x

Genge, M.J., Grady, M.M., Hutchison, R., 1997. The textures and compositions of fine-grained Antarctic micrometeorites: Implications for comparisons with meteorites. Geochim. Cosmochim. Acta 61, 5149–5162. doi:10.1016/S0016-7037(97)00308-6

Genge, M.J., van Ginneken, M., Suttle, M.D., Harvey, R.P., 2018. Accumulation mechanisms of micrometeorites in an ancient supraglacial moraine at. Meteorit. Planet. Sci. 1–16. doi:10.1111/maps.13107

Herzog, G.F., Xue, S., Hall, G.S., Nyquist, L.E., Shih, C.Y., Wiesmann, H., Brownlee, D.E., 1999. Isotopic and elemental composition of iron, nickel, and chromium in type I deep-sea spherules: Implications for origin and composition of the parent micrometeoroids. Geochim. Cosmochim. Acta 63, 1443–1457. doi:10.1016/S0016-7037(99)00011-3

Hutzler, A., Gattacceca, J., Rochette, P., Braucher, R., Carro, B., Christensen, E.J., Cournede, C., Gounelle, M., Laridhi Ouazaa, N., Martinez, R., Valenzuela, M., Warner, M., Bourles, D., 2016. Description of a very dense meteorite collection area in western Atacama: Insight into the long-term composition of the meteorite flux to Earth. Meteorit. Planet. Sci. 51, 468–482. doi:10.1111/maps.12607

Ketcham, R.A., Carlson, W.D., 2001. Acquisition, optimization and interpretation of x-ray computed tomographic imagery: Applications to the geosciences. Comput. Geosci. 27, 381–400. doi:10.1016/S0098-3004(00)00116-3

Laforce, B., Carlier, C., Vekemans, B., Villanova, J., Tucoulou, R., Ceelen, W., Vincze, L., 2016. Assessment of Ovarian Cancer Tumors Treated with Intraperitoneal Cisplatin Therapy by Nanoscopic X-ray Fluorescence Imaging. Sci. Rep. 6, 29999. doi:10.1038/srep29999

Laforce, B., Masschaele, B., Boone, M.N., Schaubroeck, D., Dierick, M., Vekemans, B., Walgraeve, C., Janssen, C., Cnudde, V., Van Hoorebeke, L., Vincze, L., 2017. Integrated Three-Dimensional Microanalysis Combining X-Ray Microtomography and X-Ray Fluorescence Methodologies. Anal. Chem. acs.analchem.7b03205. doi:10.1021/acs.analchem.7b03205

Laforce, B., Masschaele, B., Vekemans, B., Dierick, M., Hoorebeke, L. Van, Vincze, L., 2015. Development of HERAKLES : an integrated absorption tomography / X- ray fluorescence scanner for non-destructive 3D analysis on the micro-scale. 2nd UGCT Semin. B. Abstr.

Laforce, B., Schmitz, S., Vekemans, B., Rudloff, J., Garrevoet, J., Tucoulou, R., Brenker, F.E., Martinez-Criado, G., Vincze, L., 2014. Nanoscopic X-ray fluorescence imaging of meteoritic particles and diamond inclusions. Anal. Chem. 86, 12369–12374. doi:10.1021/ac503764h

Lodders, K., 2003. Solar System Abundances and Condensation Temperatures of the Elements. Astrophys. J. 591, 1220–1247. doi:10.1086/375492

Love, S.G., Brownlee, D.E., 1993. Target Porosity Effects in Impact Cratering and Collisional Disruption. Icarus 105, 216–224.

Love, S.G., Brownlee, D.E., 1991. Heating and thermal transformation of micrometeoroids entering the Earth's atmosphere. Icarus 89, 26–43. doi:10.1016/0019-1035(91)90085-8

Martinez-Criado, G., Villanova, J., Tucoulou, R., Salomon, D., Suuronen, J.P., Laboure, S., Guilloud, C., Valls, V., Barrett, R., Gagliardini, E., Dabin, Y., Baker, R., Bohic, S., Cohen, C., Morse, J., 2015. ID16B: A hard X-ray nanoprobe beamline at the ESRF for nano-analysis. J. Synchrotron Radiat. 23, 344–352. doi:10.1107/S1600577515019839

Maurette, M., Jéhanno, C., Robin, E., Hammer, C., 1987. Characteristics and mass distribution of extraterrestrial dust from the Greenland ice cap. Nature 328, 699–702.

Maurette, M., Olinger, C., Michel-Levy, M.C., Kurat, G., Pourchet, M., 1991. A collection of diverse micrometeorites recovered from 100 tonnes of Antarctic blue ice. Nature 351, 44–46. doi:10.1038/351044a0

Murray, J., Renard, A.F., 1891. Report on the deep-sea deposits based on the specimens collected during the voyage of HMS Challenger in the years 1872 to 1876. Edinburgh.

Osanai, Y., Nogi, Y., Baba, S., Nakano, N., Adachi, T., Hokada, T., Toyoshima, T., Owada, M., Satish-Kumar, M., Kamei, A., Kitano, I., 2013. Geologic evolution of the Sør Rondane Mountains, East Antarctica: Collision tectonics proposed based on metamorphic processes and magnetic anomalies. Precambrian Res. 234, 8–29. doi:10.1016/j.precamres.2013.05.017

Reimer, L., 1998. Scanning Electron Microscopy: Physics of Image Formation and Microanalysis, US Patent 5,872,358. doi:10.1002/jobm.3620270311

Rochette, P., Folco, L., Suavet, C., van Ginneken, M., Gattacceca, J., Perchiazzi, N., Braucher, R., Harvey, R.P., 2008. Micrometeorites from the Transantarctic Mountains. Proc. Natl. Acad. Sci. 105, 18206–18211. doi:10.1073/pnas.0806049105

Rousseau, R.M., Boivin, J. a, 1998. The fundamental algorithm: A natural extension of the Sherman equation Part 1: Theory. Rigaku J. 15, 13–28.

Rubin, A.E., Grossman, J.N., 2010. Meteorite and meteoroid: New comprehensive definitions. Meteorit. Planet. Sci. 45, 117–125. doi:10.1111/j.1945-5100.2009.01009.x

Schoonjans, T., Silversmit, G., Vekemans, B., Schmitz, S., Burghammer, M., Riekel, C., Brenker, F.E., Vincze, L., 2012. Fundamental parameter based quantification algorithm for confocal nano-X-ray fluorescence analysis. Spectrochim. Acta - Part B At. Spectrosc. 67, 32–42. doi:10.1016/j.sab.2011.12.006

Shiraishi, K., Dunkley, D.J., Hokada, T., Fanning, C.M., Kagami, H., Hamamoto, T., 2008. Geochronological constraints on the Late Proterozoic to Cambrian crustal evolution of eastern Dronning Maud Land, East Antarctica: a synthesis of SHRIMP U-Pb age and Nd model age data. Geol. Soc. London, Spec. Publ. 308, 21 LP-67.

Simionovici, A.S., Lemelle, L., Cloetens, P., Sole, V.A., Tresseras, J.A.S., Butterworth, A.L., Westphal, A.J., Gainsforth, Z., Stodolna, J., Allen, C., Anderson, D., Ansari, A., Bajt, S., Bassim, N., Bastien, R.K., Bechtel, H.A., Borg, J., Brenker, F.E., Bridges, J., Brownlee, D.E., Burchell, M., Burghammer, M., Changela, H., Davis, A.M., Doll, R., Floss, C., Flynn, G., Frank, D.R., Grün, E., Heck, P.R., Hillier, J.K., Hoppe, P., Hudson, B., Huth, J., Hvide, B., Kearsley, A., King, A.J., Lai, B., Leitner, J., Leonard, A., Leroux, H., Lettieri, R., Marchant, W., Nittler, L.R., Ogliore, R., Ong, W.J., Postberg, F., Price, M.C., Sandford, S.A., Schmitz, S., Schoonjans, T., Silversmit, G., Srama, R., Stadermann, F.J., Stephan, T., Sterken, V.J., Stroud, R.M., Sutton, S., Trieloff, M., Tsou, P., Tsuchiyama, A., Tyliszczak, T., Vekemans, B., Vincze, L., Von Korff, J., Wordsworth, N., Zevin, D., Zolensky, M.E., 2014. Stardust interstellar preliminary examination VI: Quantitative elemental analysis by synchrotron X-ray fluorescence nanoimaging of eight impact features in aerogel. Meteorit. Planet. Sci. 49, 1612–1625. doi:10.1111/maps.12208

Soens, B., Goderis, S., Greenwood, R.C., Mckibbin, S.J., van Ginneken, M., Vanhaecke, F., Debaille, V., Franchi, I.A., Claeys, P., 2017. Major, Trace element concentration and triple-oxygen isotope compositions of G- and I-type spherules from the SØr Rondane Mountains, East Antarctica. 80th Annu. Meet. Meteorit. Soc. 2017.

Suavet, C., Alexandre, A., Franchi, I.A., Gattacceca, J., Sonzogni, C., Greenwood, R.C., Folco, L., Rochette, P., 2010. Identification of the parent bodies of micrometeorites with high-precision oxygen isotope ratios. Earth Planet. Sci. Lett. 293, 313–320. doi:10.1016/j.epsl.2010.02.046

Suavet, C., Rochette, P., Kars, M., Gattacceca, J., Folco, L., Harvey, R.P., 2009. Statistical properties of the Transantarctic Mountains (TAM) micrometeorite collection. Polar Sci. 3, 100–109. doi:10.1016/j.polar.2009.06.003

Suganuma, Y., Miura, H., Zondervan, A., Okuno, J., 2014. East Antarctic deglaciation and the link to global cooling during the Quaternary: Evidence from glacial geomorphology and10Be surface exposure dating of the Sør Rondane Mountains, Dronning Maud Land. Quat. Sci. Rev. 97, 102–120. doi:10.1016/j.quascirev.2014.05.007

Suryanarayana, C., Grant Norton, M., 1998. X-Ray Diffraction A practical Approach, Journal of Chemical Information and Modeling. doi:10.1017/CBO9781107415324.004

Taylor, S., Lever, J.H., Harvey, R.P., 1998. Accretion rate of cosmic spherules measured at the South Pole. Nature 392, 899–903. doi:10.1038/31894

Taylor, S., Matrajt, G., Guan, Y., 2012. Fine-grained precursors dominate the micrometeorite flux. Meteorit. Planet. Sci. 47, 550–564. doi:10.1111/j.1945-5100.2011.01292.x

Taylor, S., O'D. Alexander, C.M., Delaney, J., Ma, P., Herzog, G.F., Engrand, C., 2005. Isotopic fractionation of iron, potassium, and oxygen in stony cosmic spherules: Implications for heating histories and sources. Geochim. Cosmochim. Acta 69, 2647–2662. doi:10.1016/j.gca.2004.11.027

Van Espen, P., Janssens, K., Nobels, J., 1986. AXIL-PC, Software for the Analysis of Complex X-Ray Spectra. Chemom. Intell. Lab. Syst. 1, 109–114. doi:10.1016/0169-7439(86)80031-4

van Ginneken, M., Folco, L., Cordier, C., Rochette, P., 2012. Chondritic micrometeorites from the Transantarctic Mountains. Meteorit. Planet. Sci. 47, 228–247. doi:10.1111/j.1945-5100.2011.01322.x

van Ginneken, M., Gattacceca, J., Rochette, P., Sonzogni, C., Alexandre, A., Vidal, V., Genge, M.J., 2017a. The parent body controls on cosmic spherule texture: Evidence from the oxygen isotopic compositions of large micrometeorites. Geochim. Cosmochim. Acta 212, 196–210. doi:10.1016/j.gca.2017.05.008

van Ginneken, M., Genge, M.J., Folco, L., Harvey, R.P., 2016. The weathering of micrometeorites from the Transantarctic Mountains. Geochim. Cosmochim. Acta 179, 1–31. doi:10.1016/j.gca.2015.11.045

van Ginneken, M., Goderis, S., Soens, B., Debaille, V., Avila, J., Holden, P., Mckibbin, S.J., Claeys, P., Ireland, T., 2017b. Identification of the parent bodies of micrometeorites from the Widerøefjellet, Sør Rondane Mountains , by means of oxygen isotopes. 8th Symp. Polar Sci.

Vekemans, B., Janssens, K., Vincze, L., Adams, F., Van Espen, P., 1994. Analysis of X-ray-spectry by iterative least-squares (AXIL): new developments. X-Ray Spectrom. 23, 278–285. doi:10.1002/xrs.1300230609

Vlassenbroeck, J., Dierick, M., Masschaele, B., Cnudde, V., Van Hoorebeke, L., Jacobs, P., 2007. Software tools for quantification of X-ray microtomography at the UGCT. Nucl. Instruments Methods Phys. Res. Sect. A Accel. Spectrometers, Detect. Assoc. Equip. 580, 442–445. doi:10.1016/j.nima.2007.05.073

Weisberg, M.K., McCoy, T.J., Krot, A.N., 2006. Systematics and Evaluation of Meteorite Classification. Meteorites early Sol. Syst. II 19–52.

Westphal, A.J., Allbrink, A., Allen, C., Bajt, S., Bastien, R., Bechtel, H., Bleuet, P., Borg, J., Bowker, S., Brenker, F., Bridges, J., Brownlee, D.E., Burchell, M., Burghammer, M., Butterworth, A.L., Campanile, A., Cloetens, P., Cody, G., Ferroir, T., Ferrari, K., Floss, C., Flynn, G.J., Frank, D., Gainsforth, Z., Grün, E., Harmer, M., Hoppe, P., Kearsley, A., Kulkarni, S., Lai, B., Lemelle, L., Leroux, H., Lettieri, R., Marchant, W., McCreadie, B., Nittler, L.R., Ogliore, R., Postberg, F., Rigamonti, C., Sandford, S.A., Schmitz, S., Silversmit, G., Simionovici, A., Sperry, G., Srama, R., Stadermann, F., Stephan, T., Stroud, R.M., Susini, J., Sutton, S., Thompson, V., Toucoulou, R., Trieloff, M., Tsou, P., Tsuchiyama, A., Tyliczszak, T., Vekemans, B., Vincze, L., Warren, J., Yahnke, T., Zevin, D., Zolensky, M.E., 2010. Non-destructive search for interstellar dust using synchrotron microprobes. AIP Conf. Proc. 1221, 131–138. doi:10.1063/1.3399239

Westphal, A.J., Bechtel, H.A., Brenker, F.E., Butterworth, A.L., Flynn, G., Frank, D.R., Gainsforth, Z., Hillier, J.K., Postberg, F., Simionovici, A.S., Sterken, V.J., Stroud, R.M., Allen, C., Anderson, D., Ansari, A., Bajt, S., Bastien, R.K., Bassim, N., Borg, J., Bridges, J., Brownlee, D.E., Burchell, M., Burghammer, M., Changela, H., Cloetens, P., Davis, A.M., Doll, R., Floss, C., Grün, E., Heck, P.R., Hoppe, P., Hudson, B., Huth, J., Hvide, B., Kearsley, A., King, A.J., Lai, B., Leitner, J., Lemelle, L., Leroux, H., Leonard, A., Lettieri, R., Marchant, W., Nittler, L.R., Ogliore, R., Ong, W.J., Price, M.C., Sandford, S.A., Tresseras, J.A.S., Schmitz, S., Schoonjans, T., Silversmit, G., Solé, V.A., Srama, R., Stadermann, F., Stephan, T., Stodolna, J., Sutton, S., Trieloff, M., Tsou, P., Tsuchiyama, A., Tyliszczak, T., Vekemans, B., Vincze, L., Von Korff, J., Wordsworth, N., Zevin, D., Zolensky, M.E., 2014. Final reports of the stardust interstellar preliminary examination. Meteorit. Planet. Sci. 49, 1720–1733. doi:10.1111/maps.12221

8. Appendix

A. XRF data Herakles

Sc1

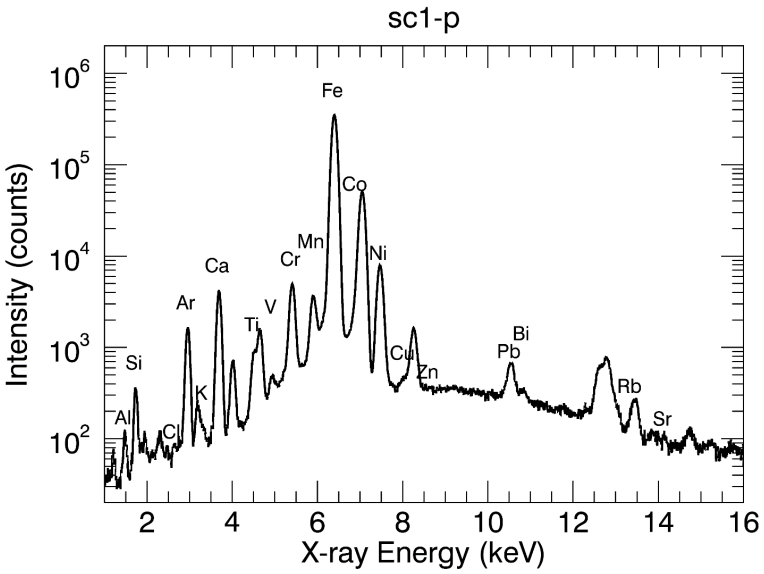

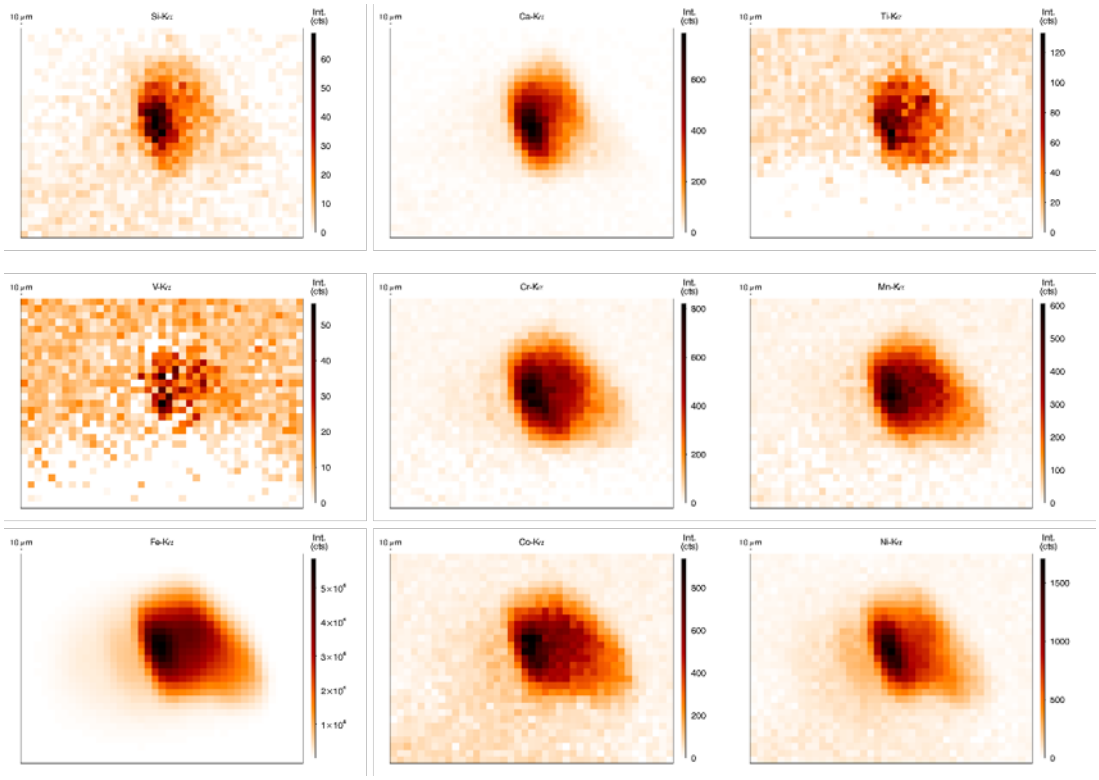

Sc3

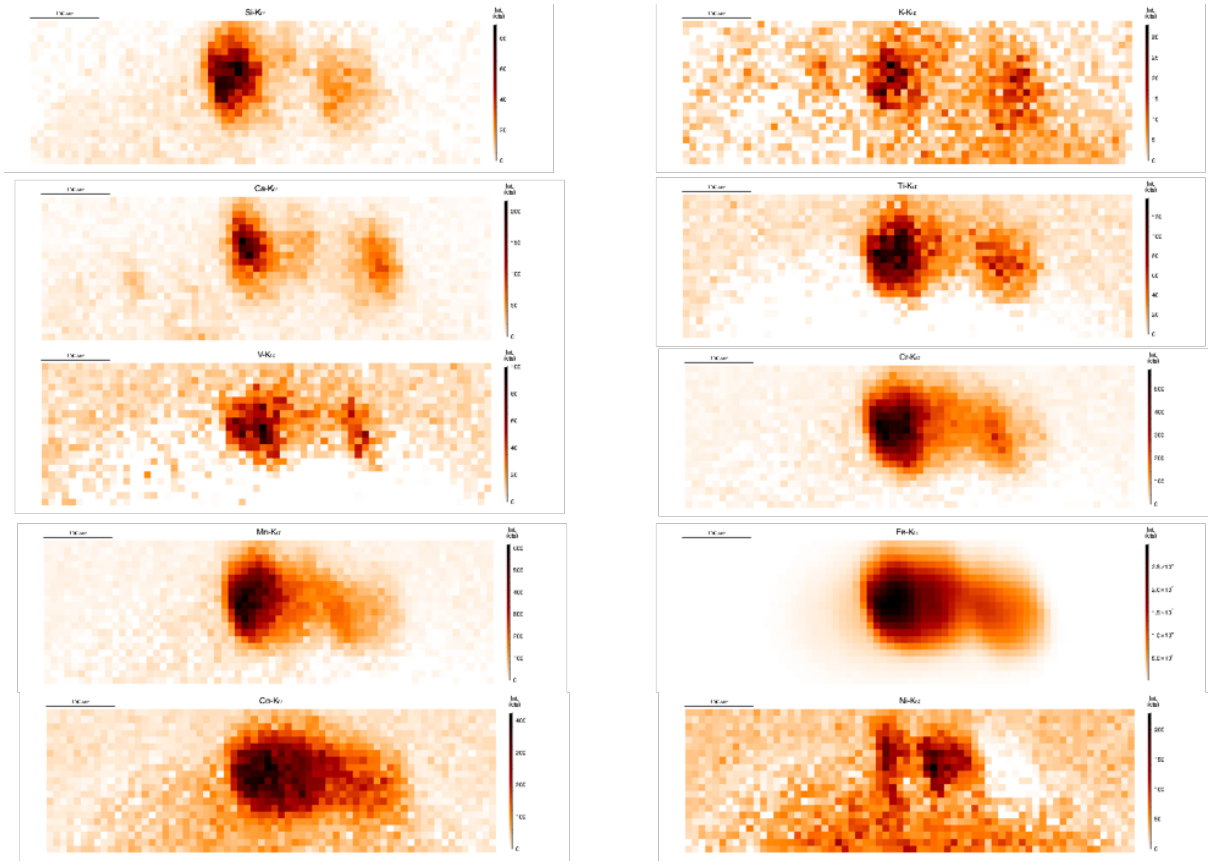

Sc4

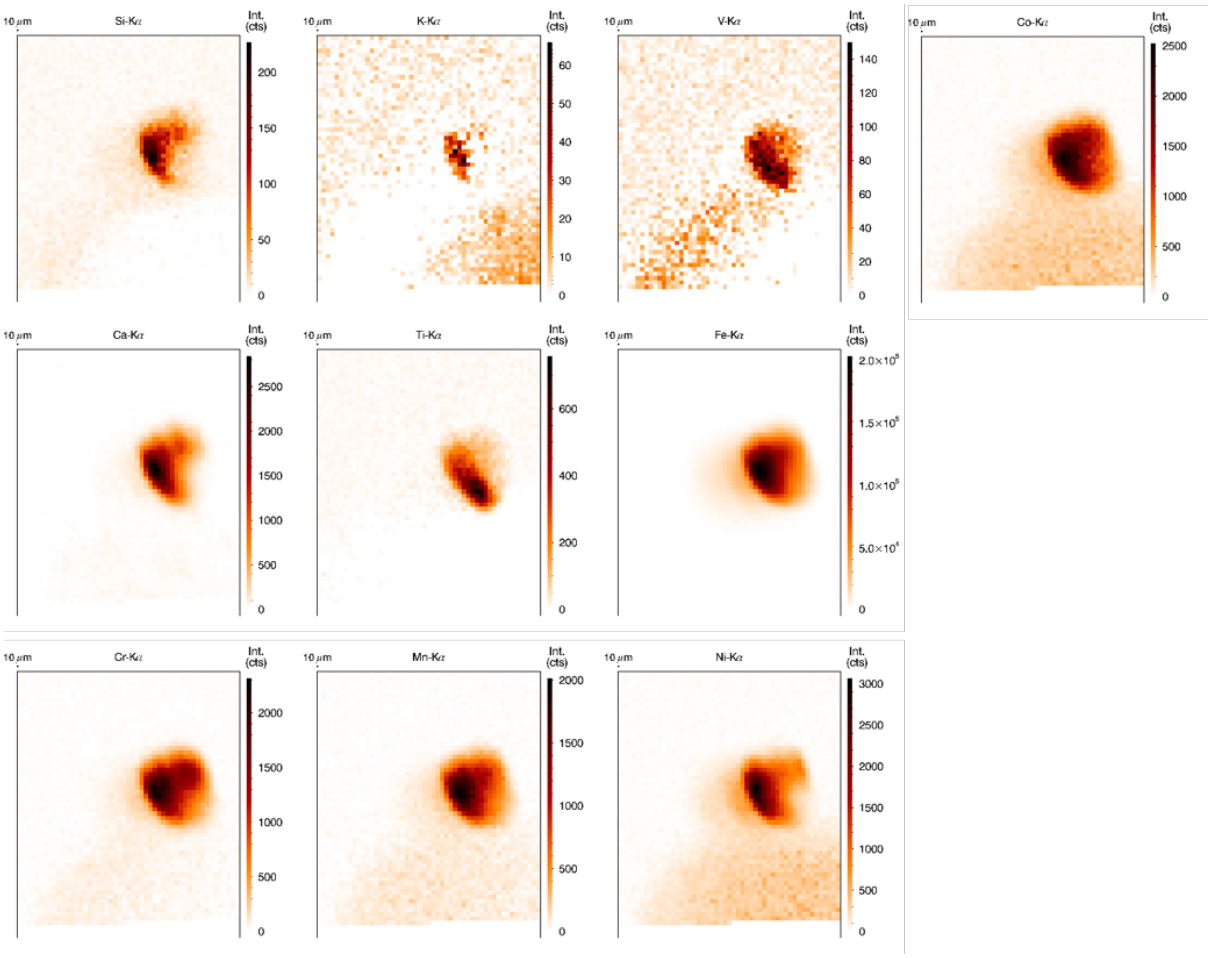
10 μm
Si-Kα
Int. (cts)
200
150
100
50
0
10 μm
K-Kα
Int. (cts)
60
50
40
30
20
10
0
10 μm
V-Kα
Int. (cts)
140
120
100
80
60
40
20
0
10 μm
Co-Kα
Int. (cts)
2500
2000
1500
1000
500
0
10 μm
Ca-Kα
Int. (cts)
2500
2000
1500
1000
500
0
10 μm
Ti-Kα
Int. (cts)
600
400
200
0
10 μm
Fe-Kα
Int. (cts)
2.0×10^5
1.5×10^5
1.0×10^5
5.0×10^4
0
10 μm
Cr-Kα
Int. (cts)
2000
1500
1000
500
0
10 μm
Mn-Kα
Int. (cts)
2000
1500
1000
500
0
10 μm
Ni-Kα
Int. (cts)
3000
2500
2000
1500
1000
500
0

U1

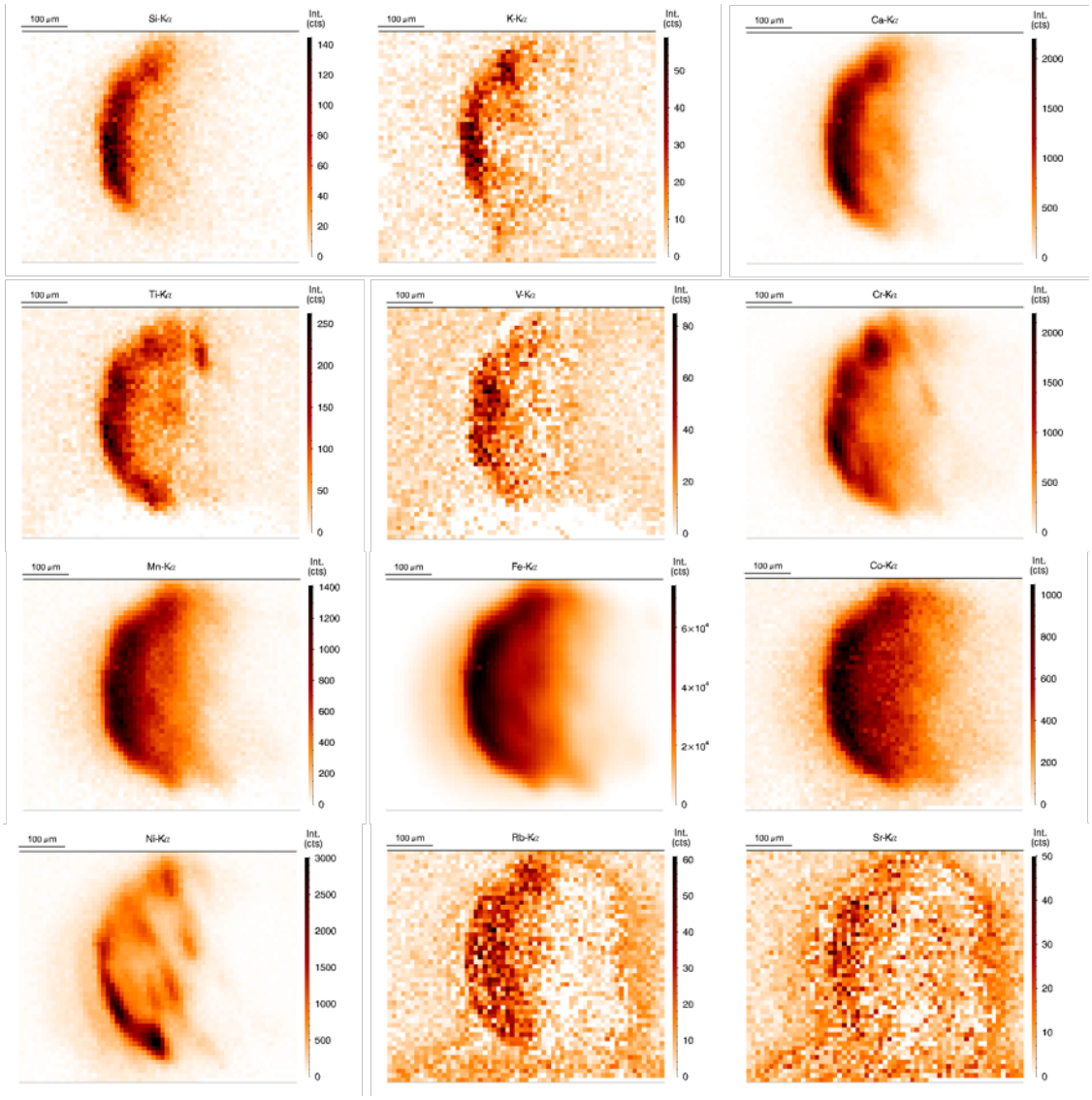
100 µm
Si-Kα
Int. (cts)
140
120
100
80
60
40
20
0
100 µm
K-Kα
Int. (cts)
50
40
30
20
10
0
100 µm
Ca-Kα
Int. (cts)
2000
1500
1000
500
0
100 µm
Ti-Kα
Int. (cts)
250
200
150
100
50
0
100 µm
V-Kα
Int. (cts)
80
60
40
20
0
100 µm
Cr-Kα
Int. (cts)
2000
1500
1000
500
0
100 µm
Mn-Kα
Int. (cts)
1400
1200
1000
800
600
400
200
0
100 µm
Fe-Kα
Int. (cts)
6×10⁴
4×10⁴
2×10⁴
0
100 µm
Co-Kα
Int. (cts)
1000
800
600
400
200
0
100 µm
Ni-Kα
Int. (cts)
3000
2500
2000
1500
1000
500
0
100 µm
Rb-Kα
Int. (cts)
60
50
40
30
20
10
0
100 µm
Sr-Kα
Int. (cts)
50
40
30
20
10
0

Uc1

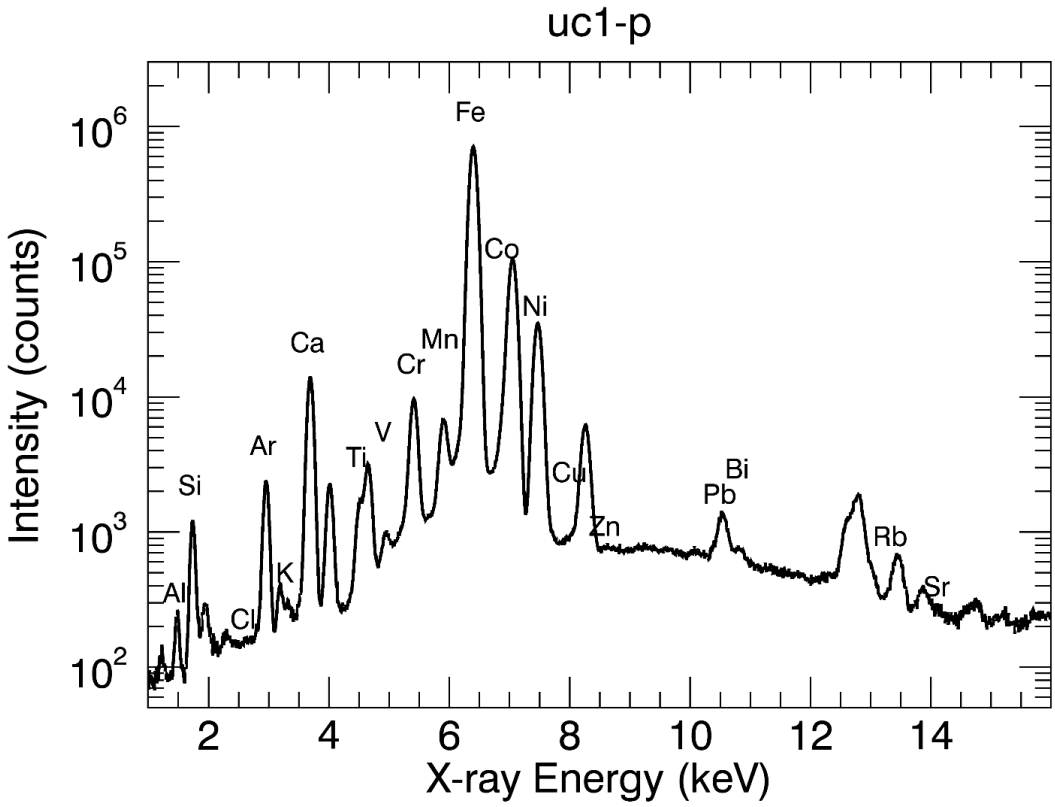
uc1-p
Intensity (counts)
X-ray Energy (keV)
Si
Al
Cl
Ar
K
Ca
Ti
V
Cr
Mn
Fe
Co
Ni
Cu
Zn
Pb
Bi
Rb
Sr

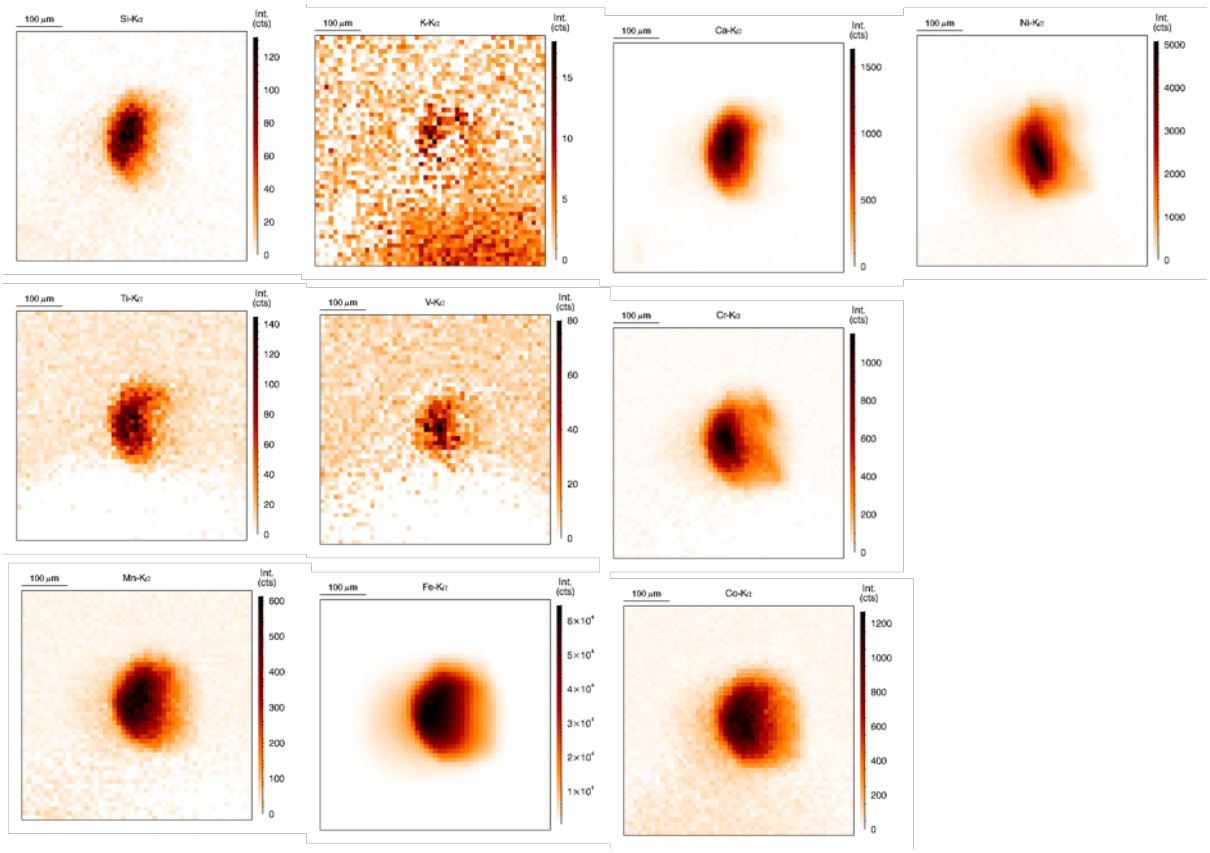

Uc2

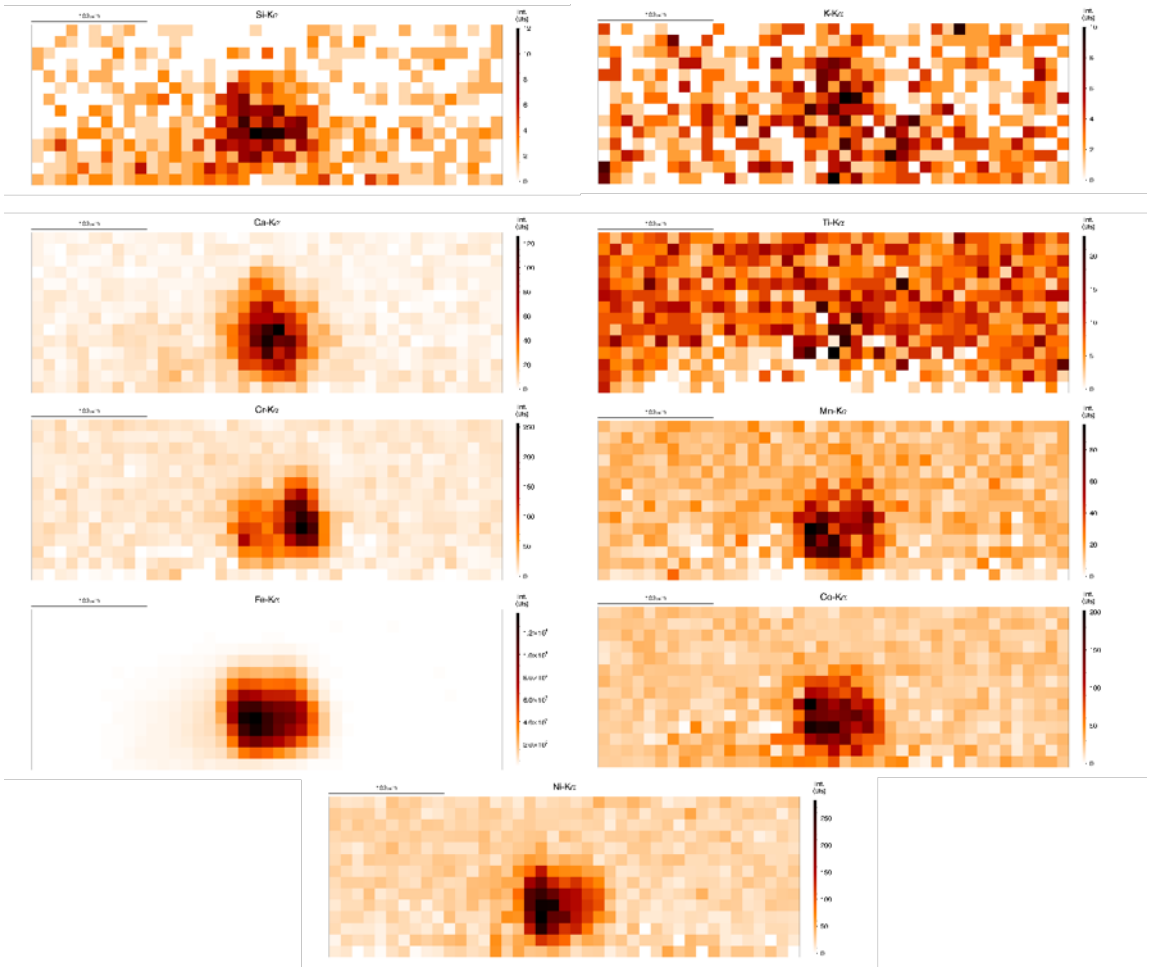
Si-Kα
K-Kα
Ca-Kα
Ti-Kα
Cr-Kα
Mn-Kα
Fe-Kα
Co-Kα
Ni-Kα

Uc3

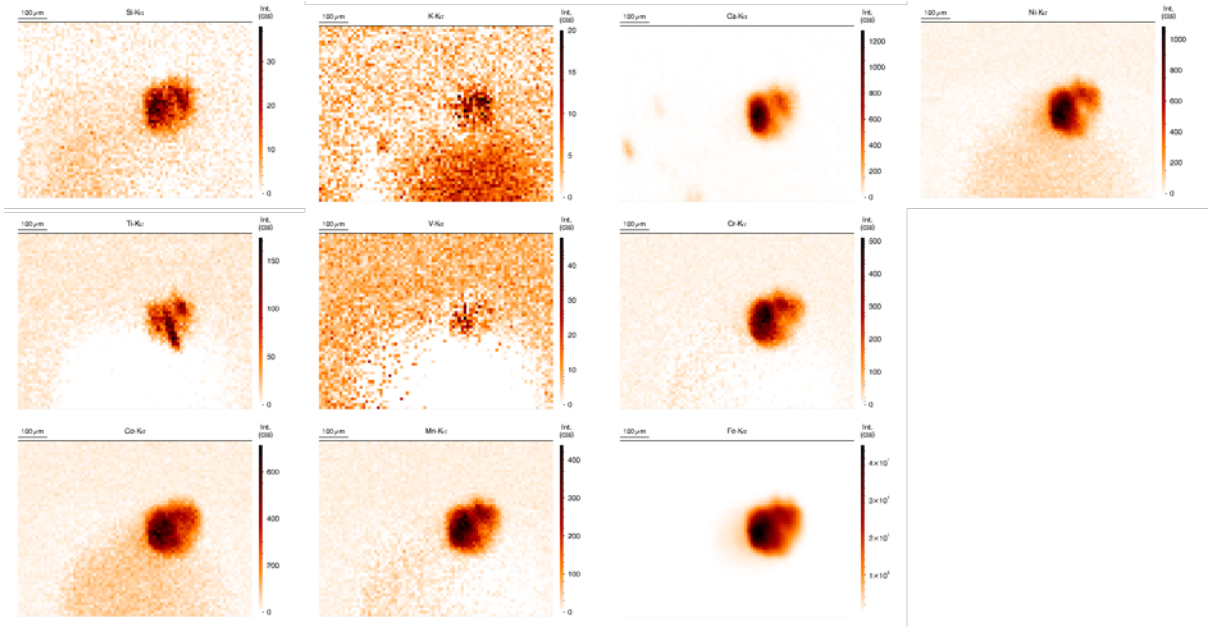
Si-Kα
K-Kα
Ca-Kα
Ni-Kα
Ti-Kα
V-Kα
Cr-Kα
Co-Kα
Mn-Kα
Fe-Kα

Uf1

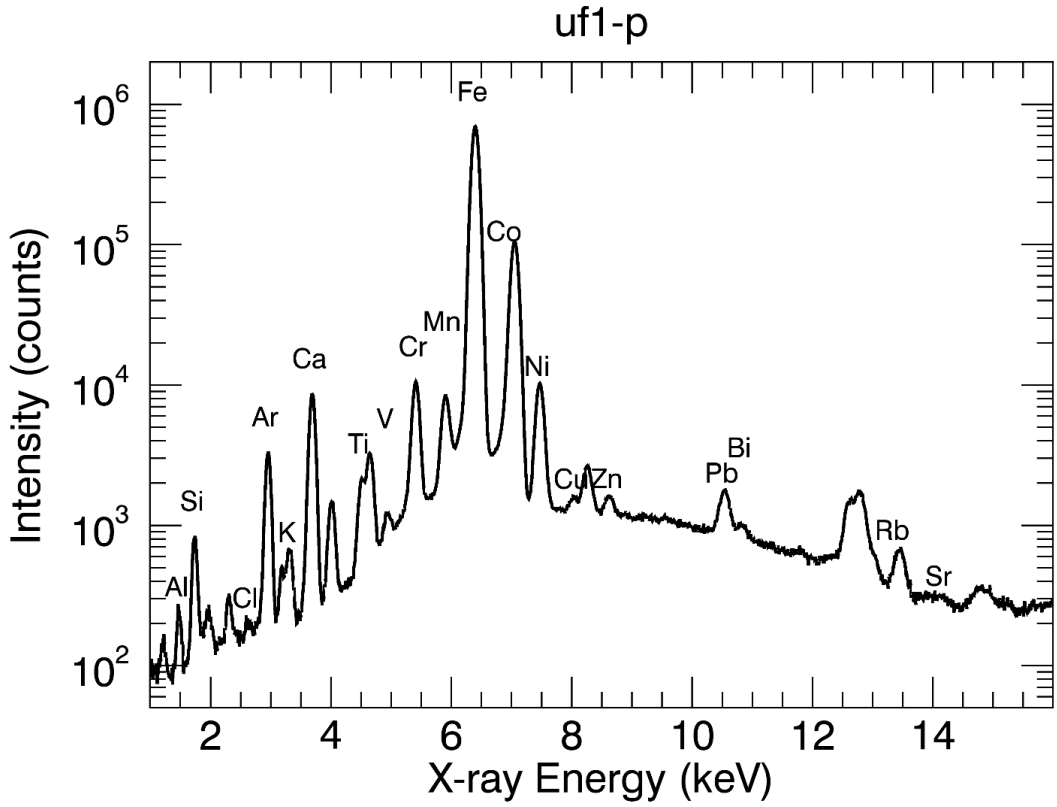
uf1-p
Intensity (counts)
X-ray Energy (keV)
Fe
Co
Mn
Cr
Ni
Ca
Ar
V
Ti
Si
K
Al
Cl
Cu
Zn
Pb
Bi
Rb
Sr

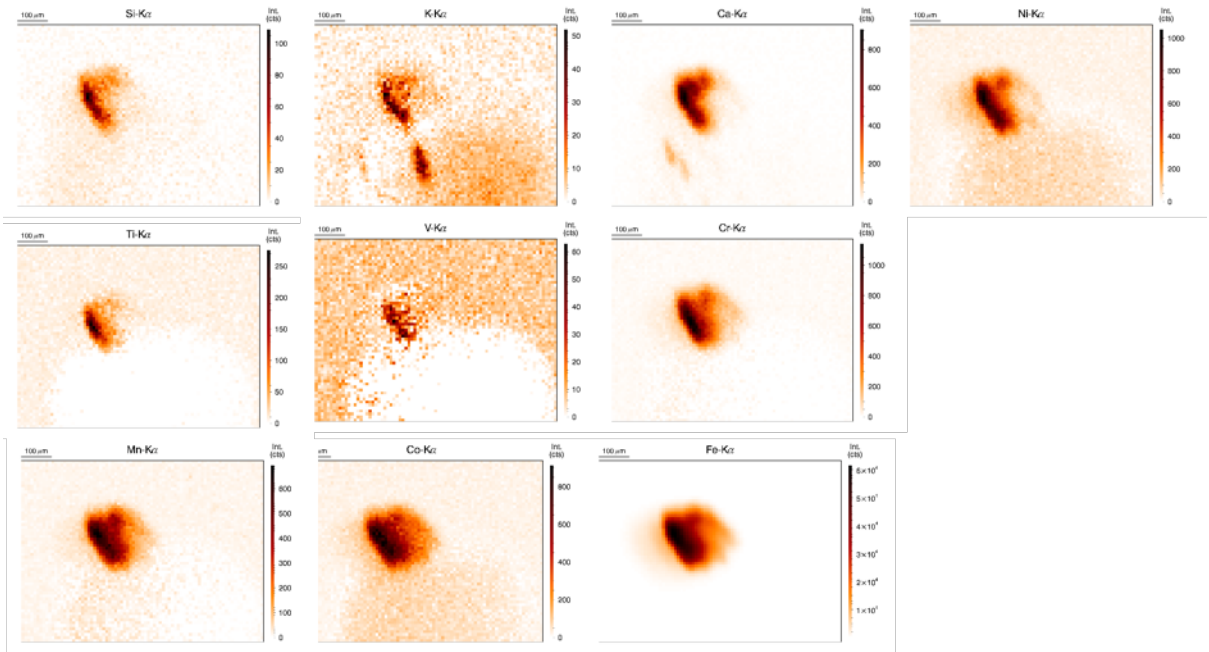
Si-Kα
K-Kα
Ca-Kα
Ni-Kα
Ti-Kα
V-Kα
Cr-Kα
Mn-Kα
Co-Kα
Fe-Kα

Uf2

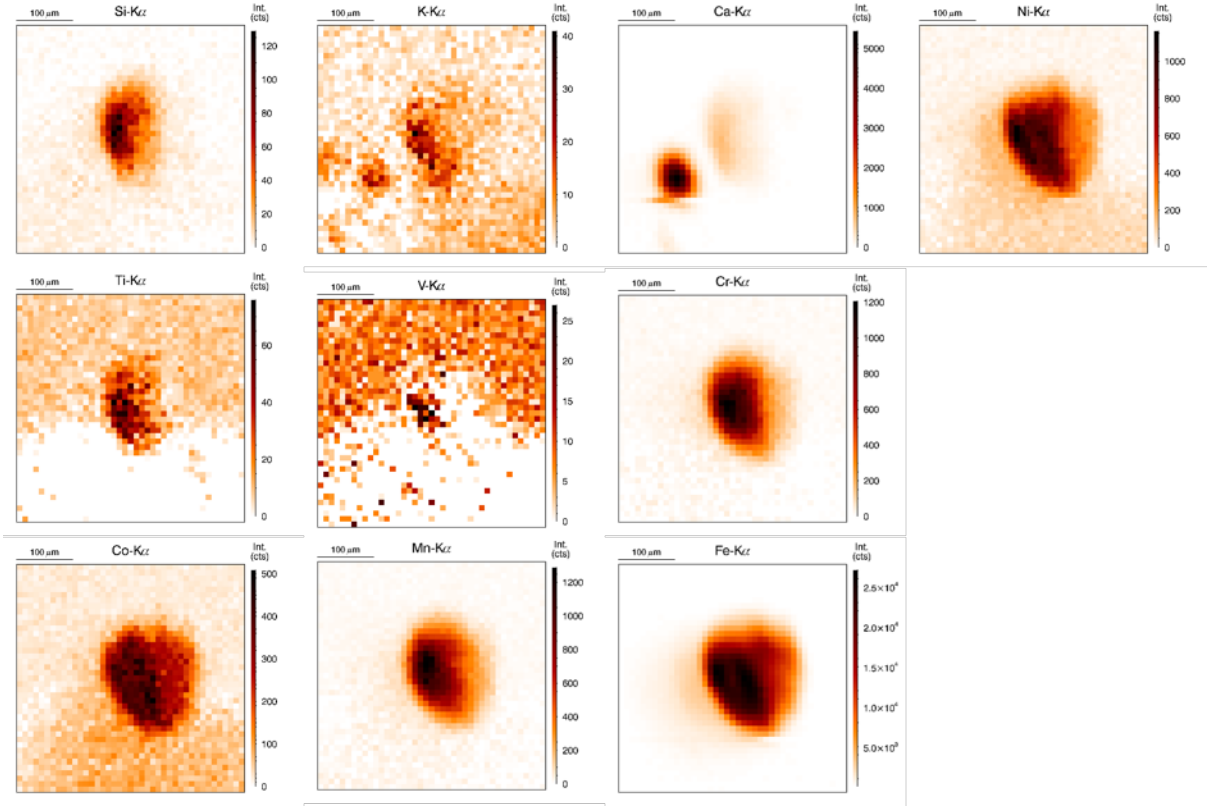
100 µm
Si-Kα
Int. (cts)
120
100
80
60
40
20
0
100 µm
K-Kα
Int. (cts)
40
30
20
10
0
100 µm
Ca-Kα
Int. (cts)
5000
4000
3000
2000
1000
0
100 µm
Ni-Kα
Int. (cts)
1000
800
600
400
200
0
100 µm
Ti-Kα
Int. (cts)
60
40
20
0
100 µm
V-Kα
Int. (cts)
25
20
15
10
5
0
100 µm
Cr-Kα
Int. (cts)
1200
1000
800
600
400
200
0
100 µm
Co-Kα
Int. (cts)
500
400
300
200
100
0
100 µm
Mn-Kα
Int. (cts)
1200
1000
800
600
400
200
0
100 µm
Fe-Kα
Int. (cts)
2.5×10⁴
2.0×10⁴
1.5×10⁴
1.0×10⁴
5.0×10³

B. XRF data ID16B beamline

Sc2 overview

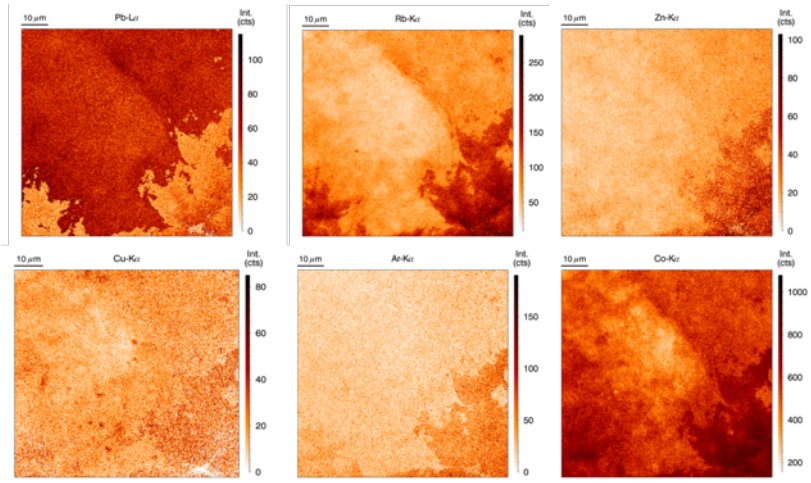

Sc2 detail 1_2

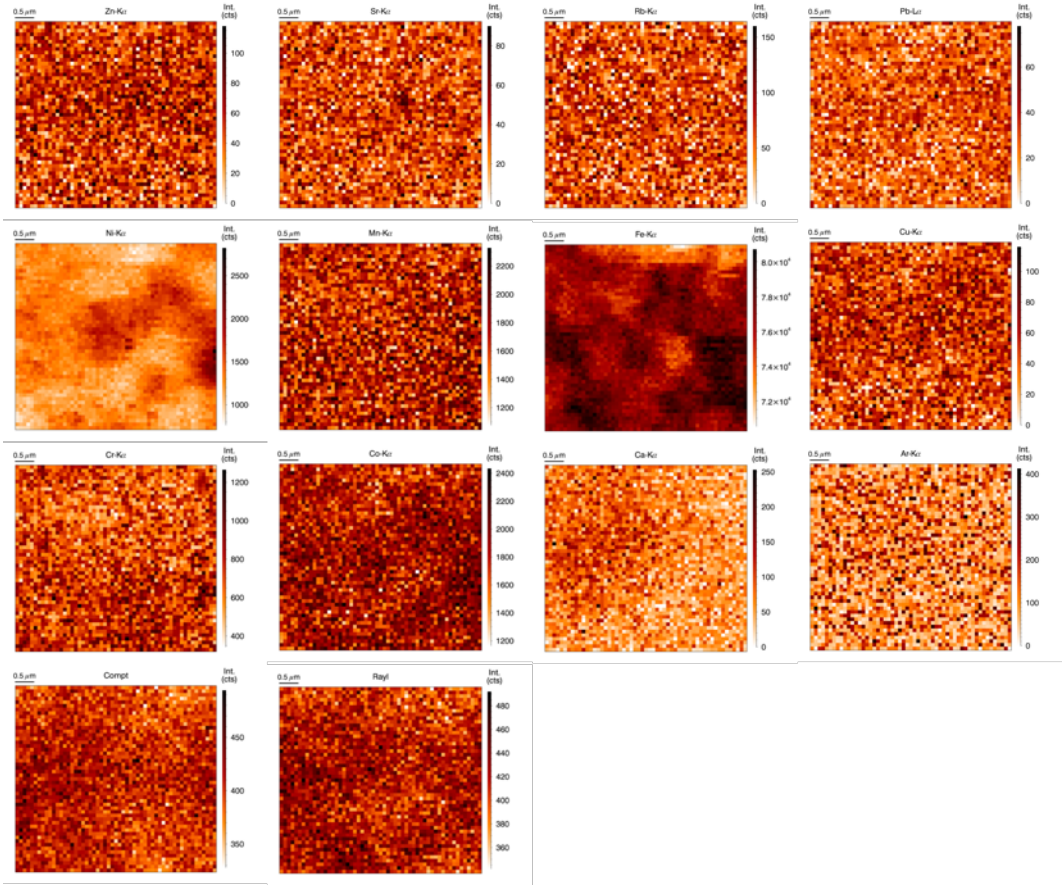

Sc2 detail 1_3

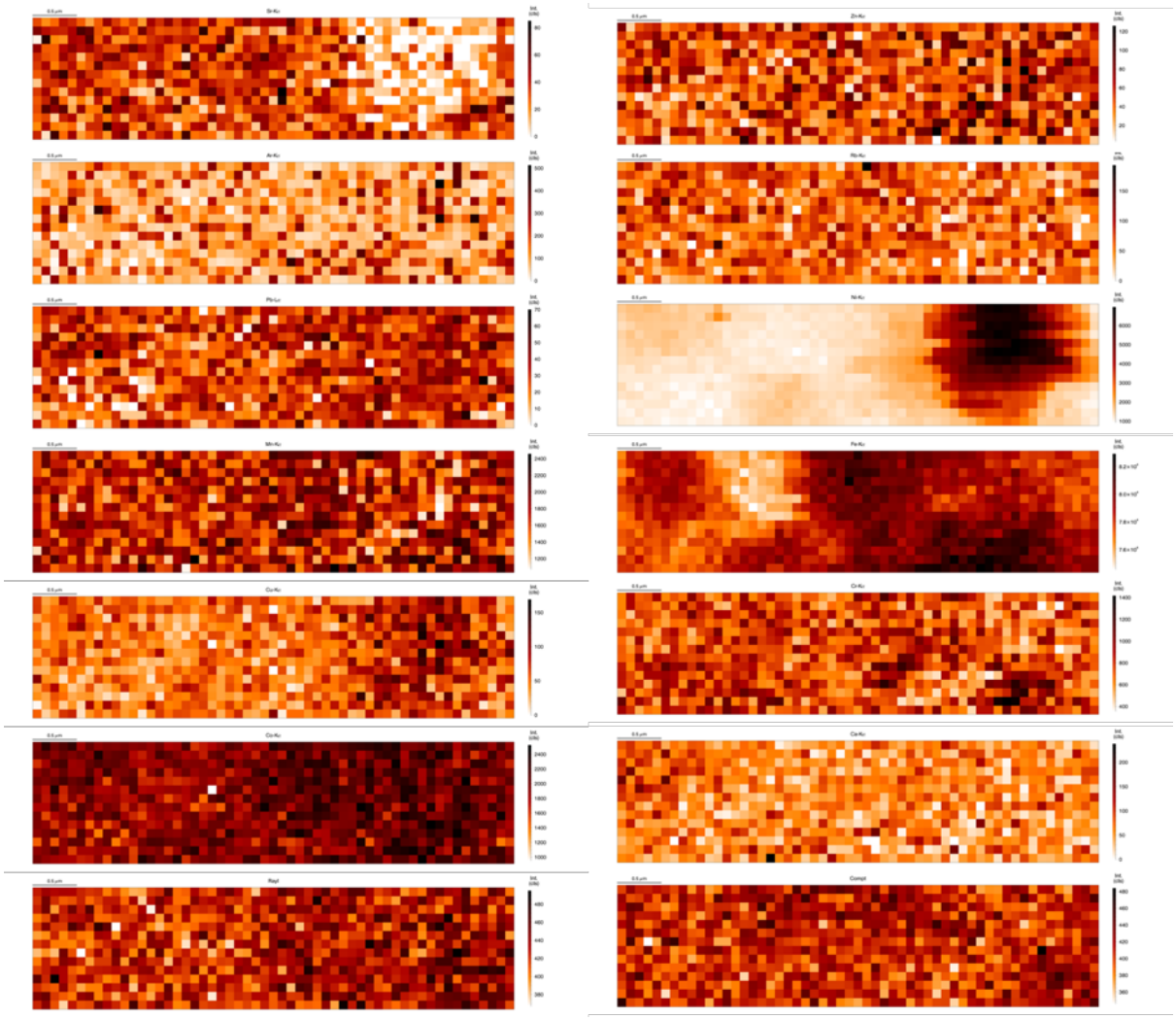

Sc2 detail 2_1

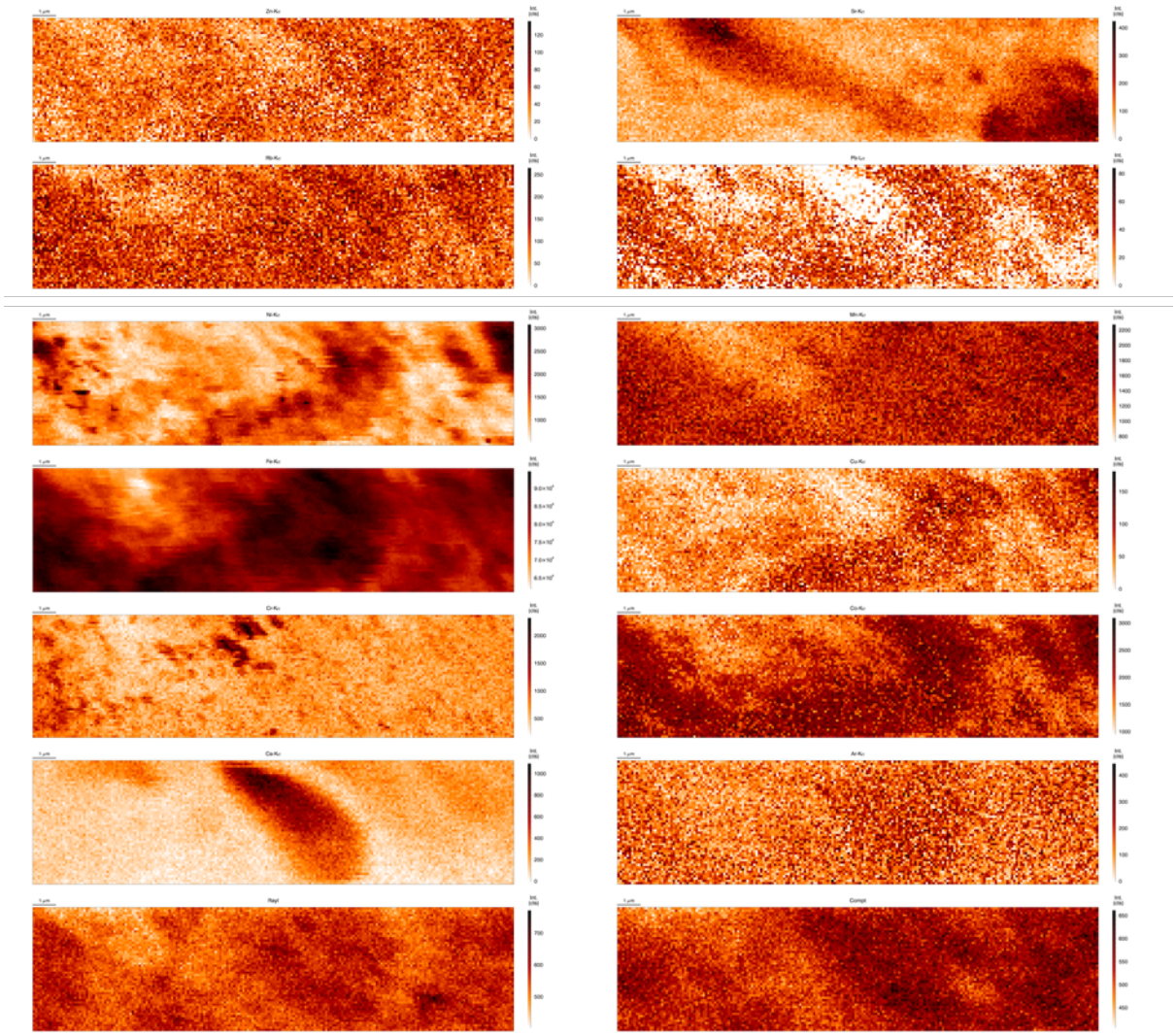

Sc2 detail 3_1

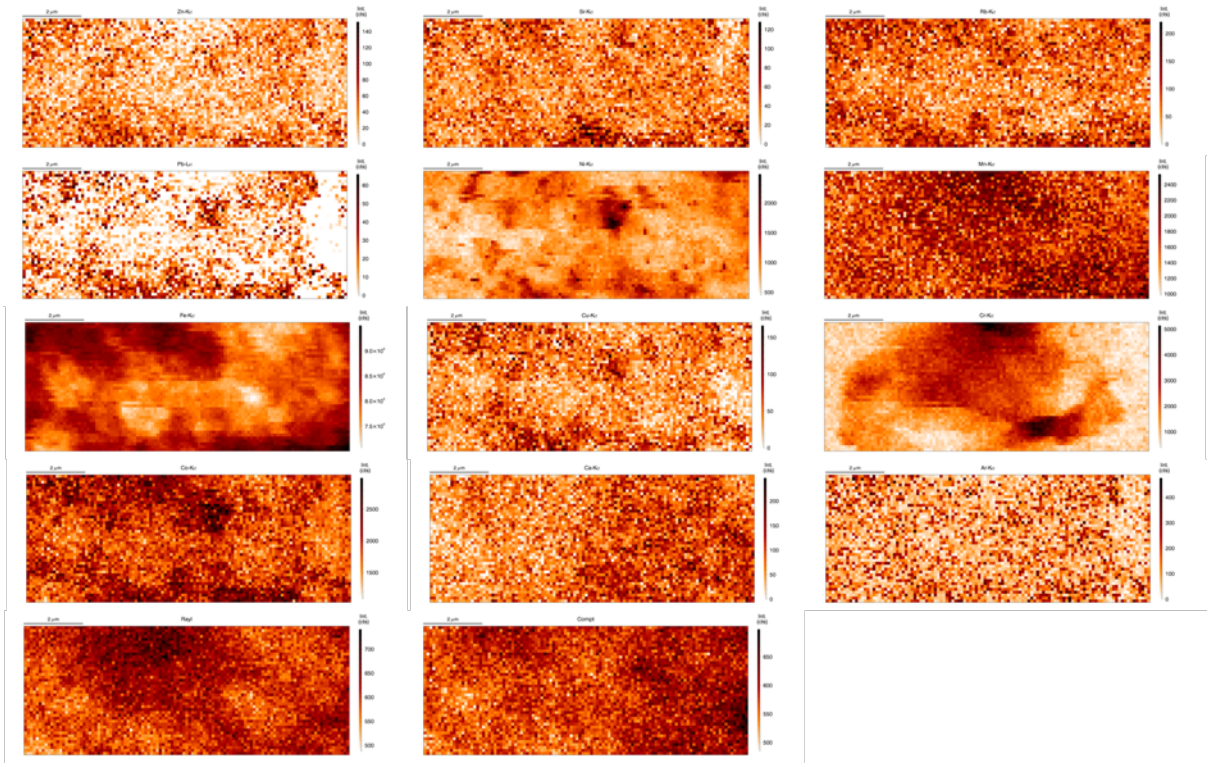

Sc2 detail 4_1

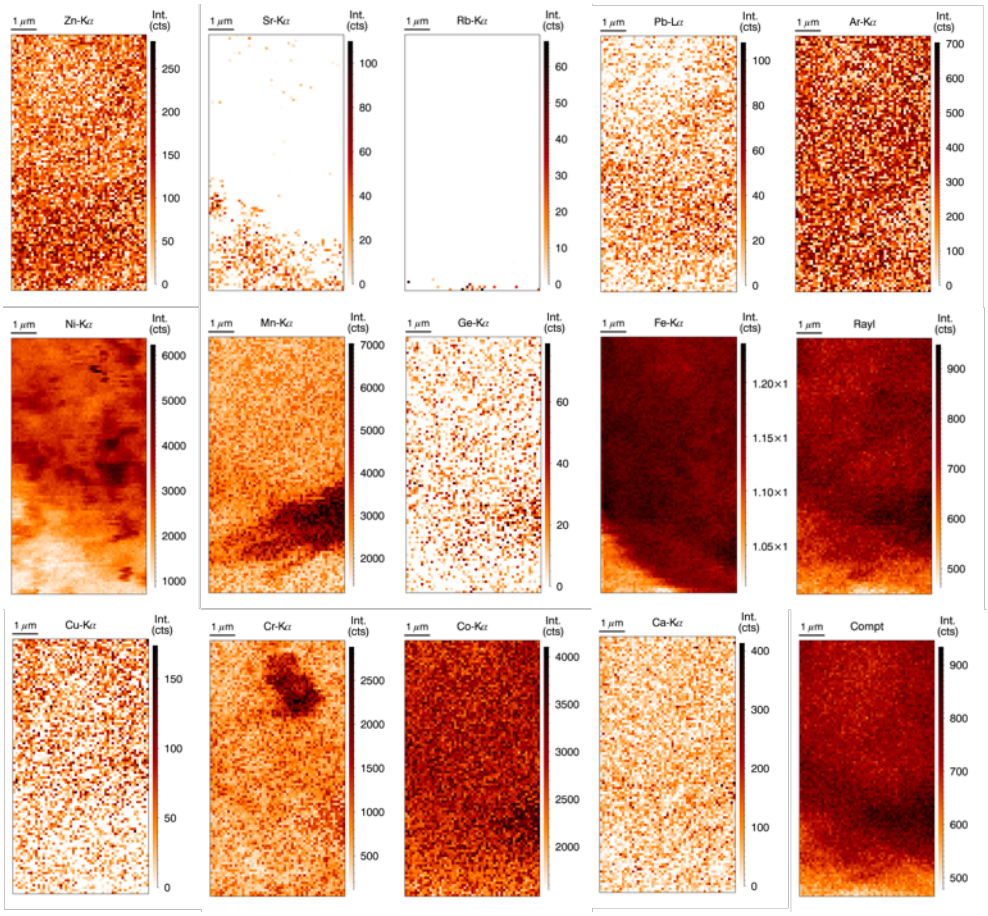

Sc3 overview

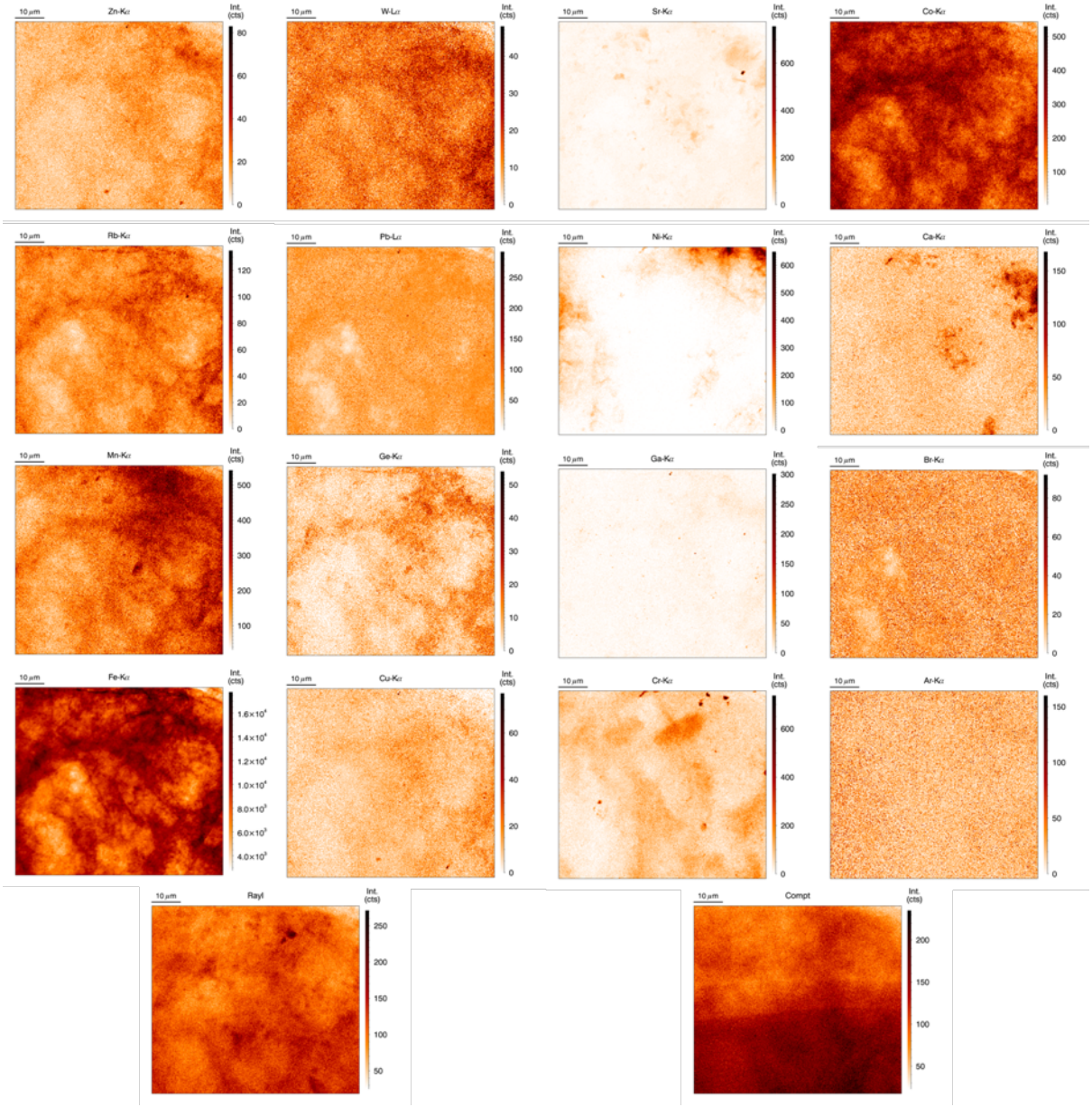

Sc3 detail d_2

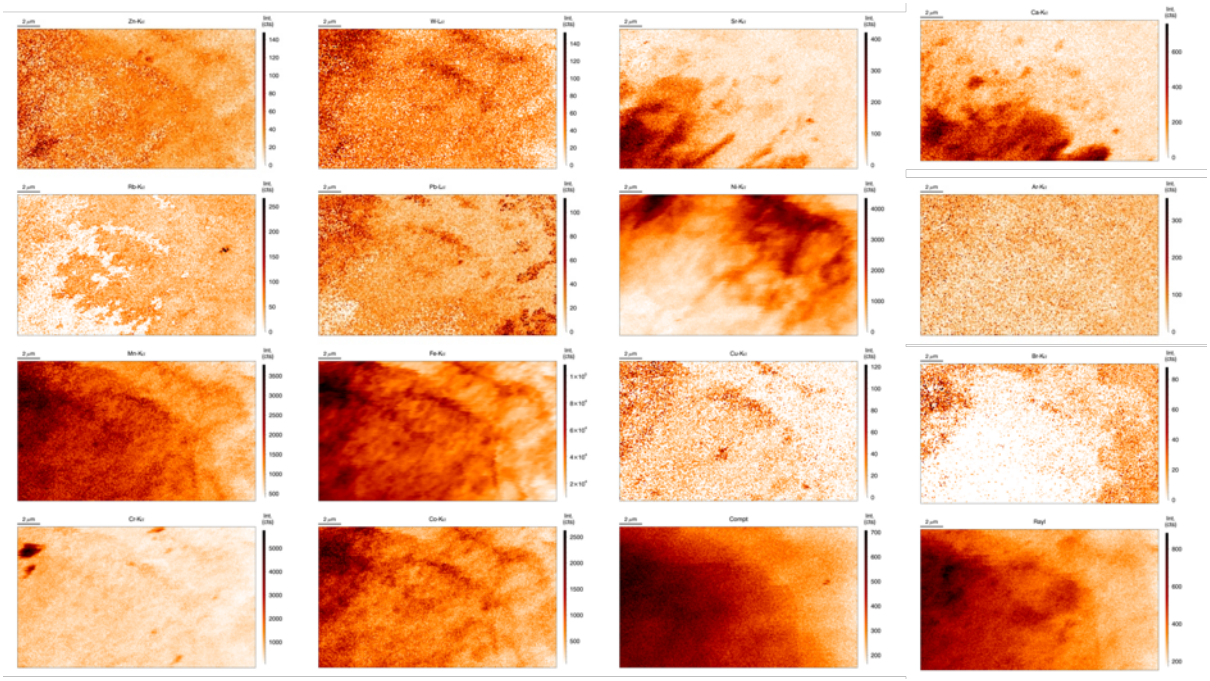

Sc3 detail d_3

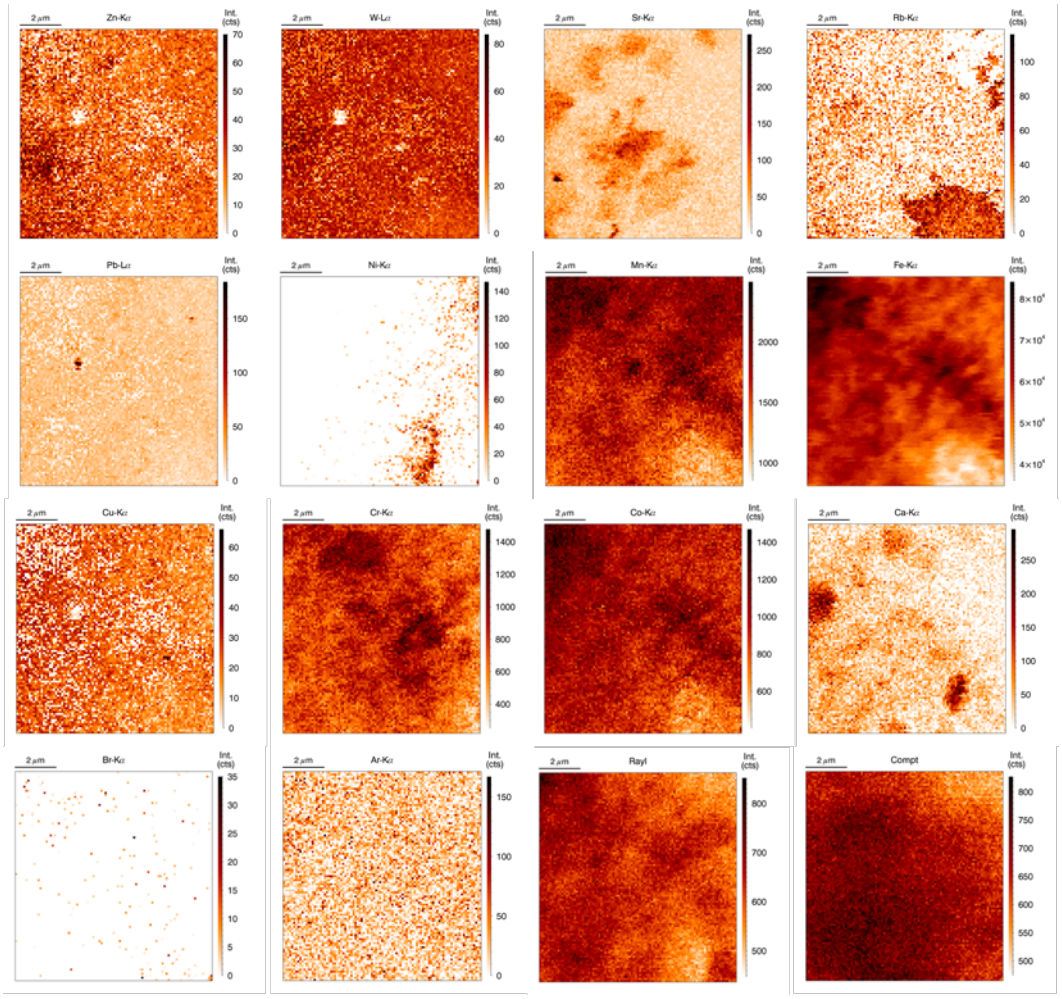

Sc3 detail d_4

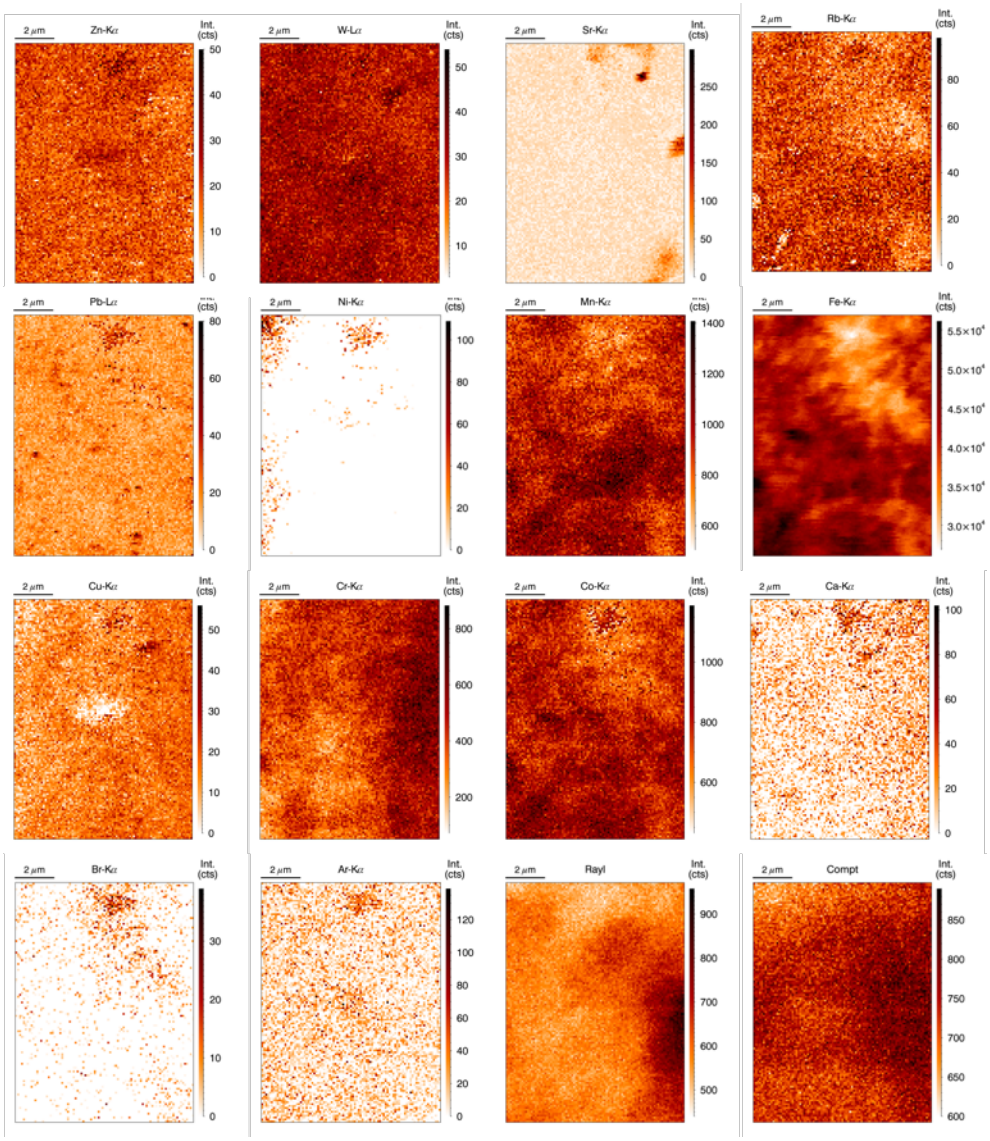

Sc3 detail d_5

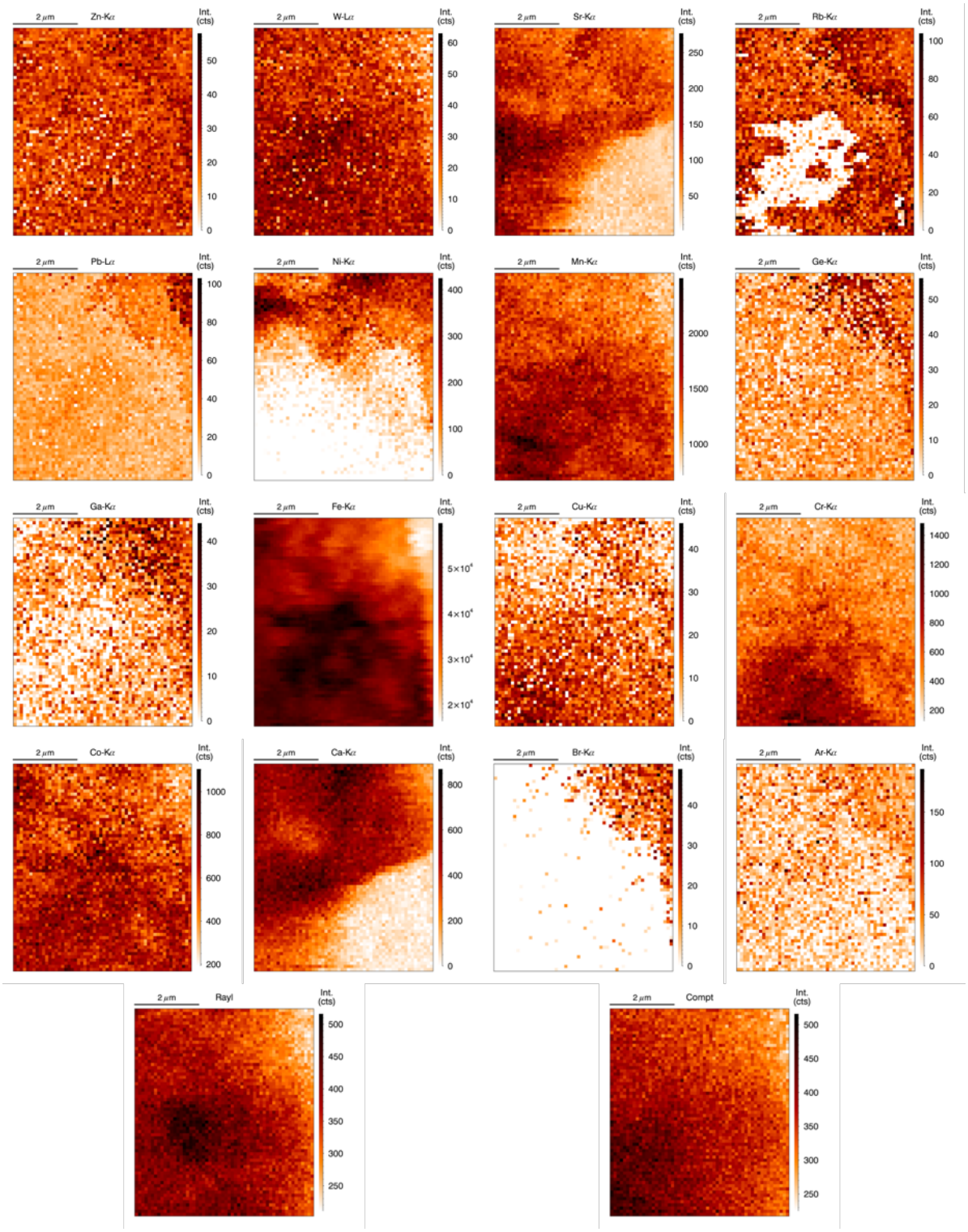

Sc4 overview

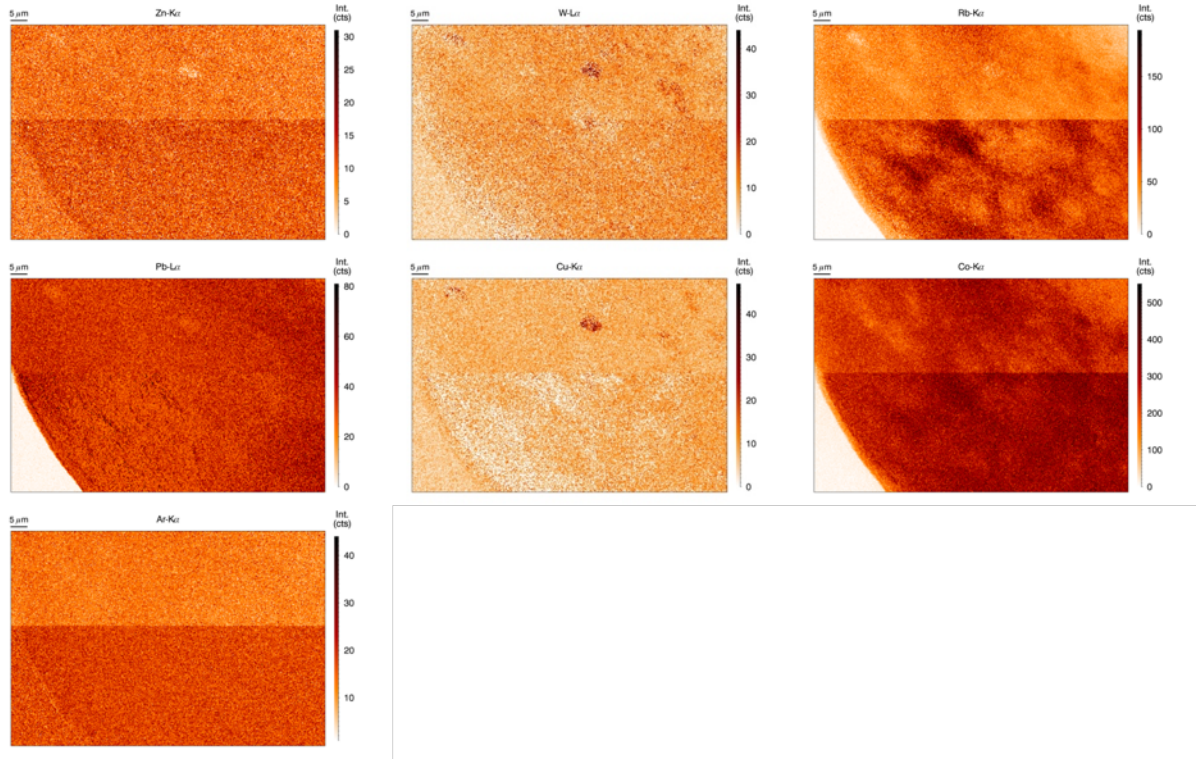

Sc4 detail 2_1

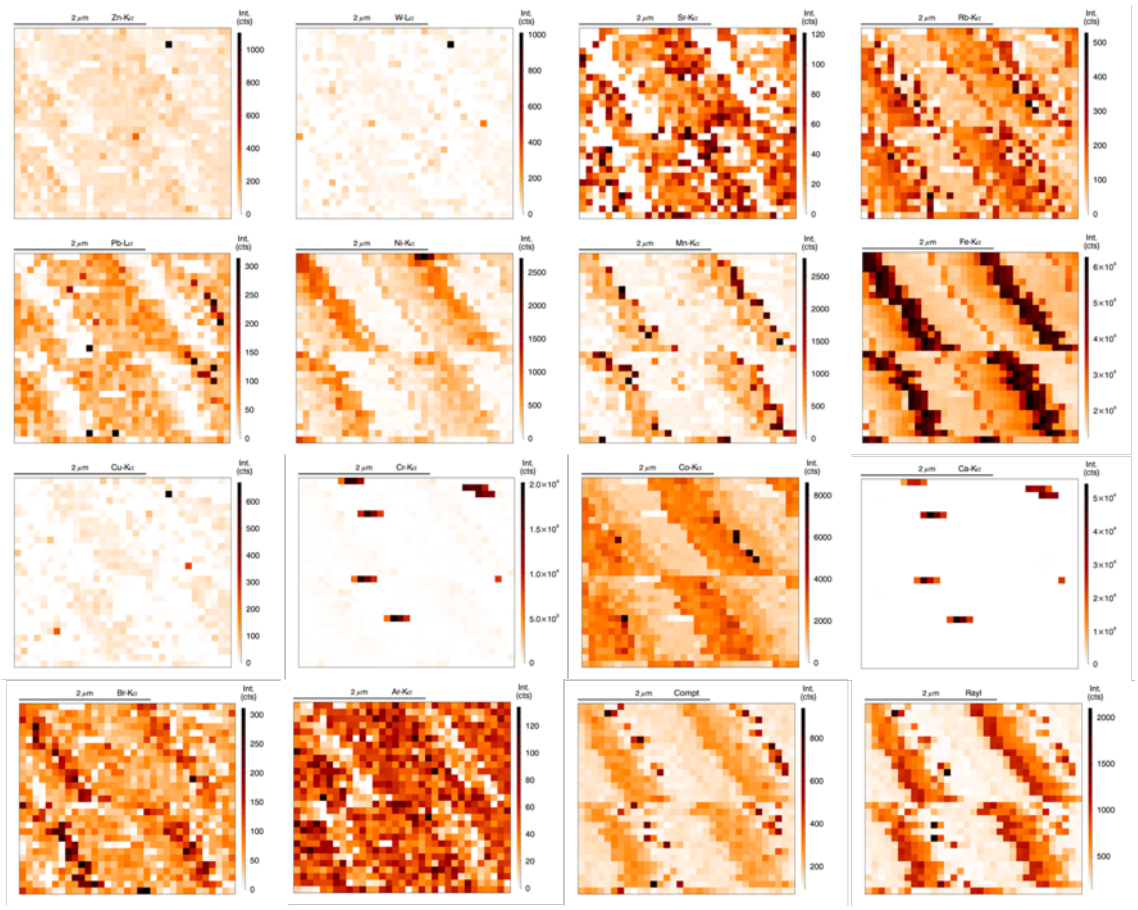

Sc4 detail 2_2

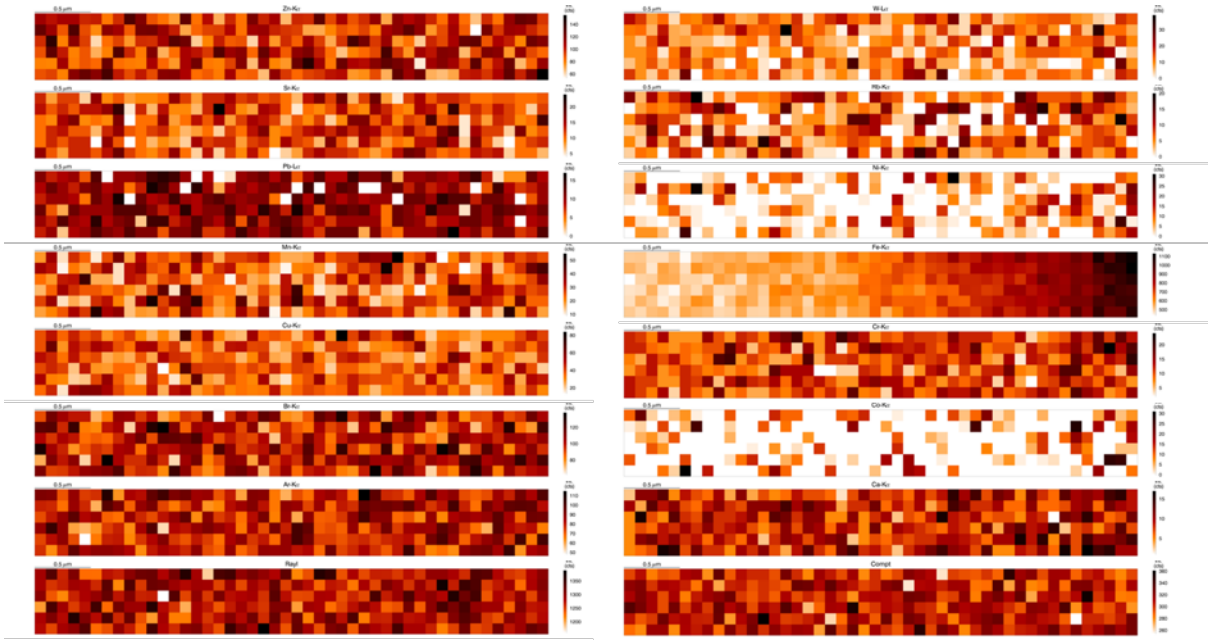

Sc4 detail 2_3

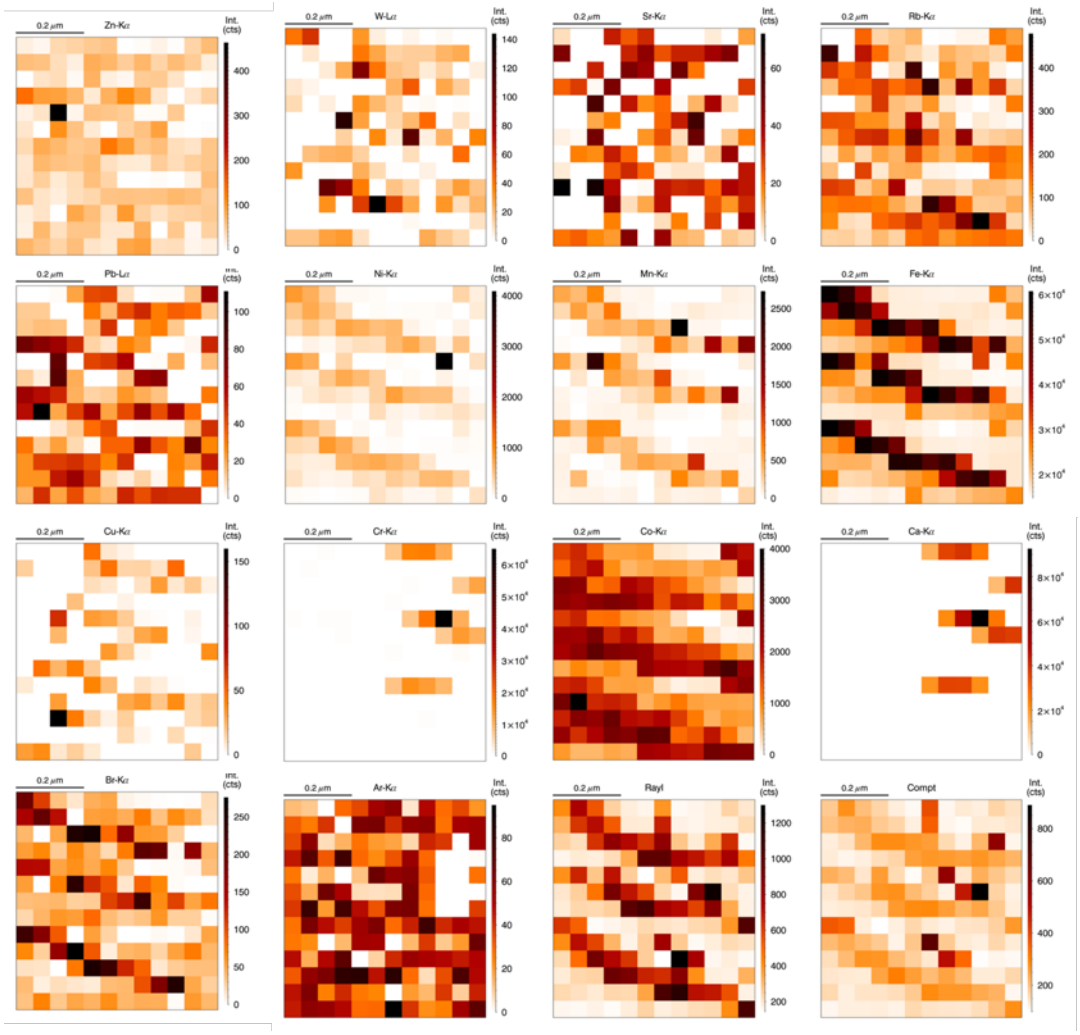

Sc4 detail 2_4

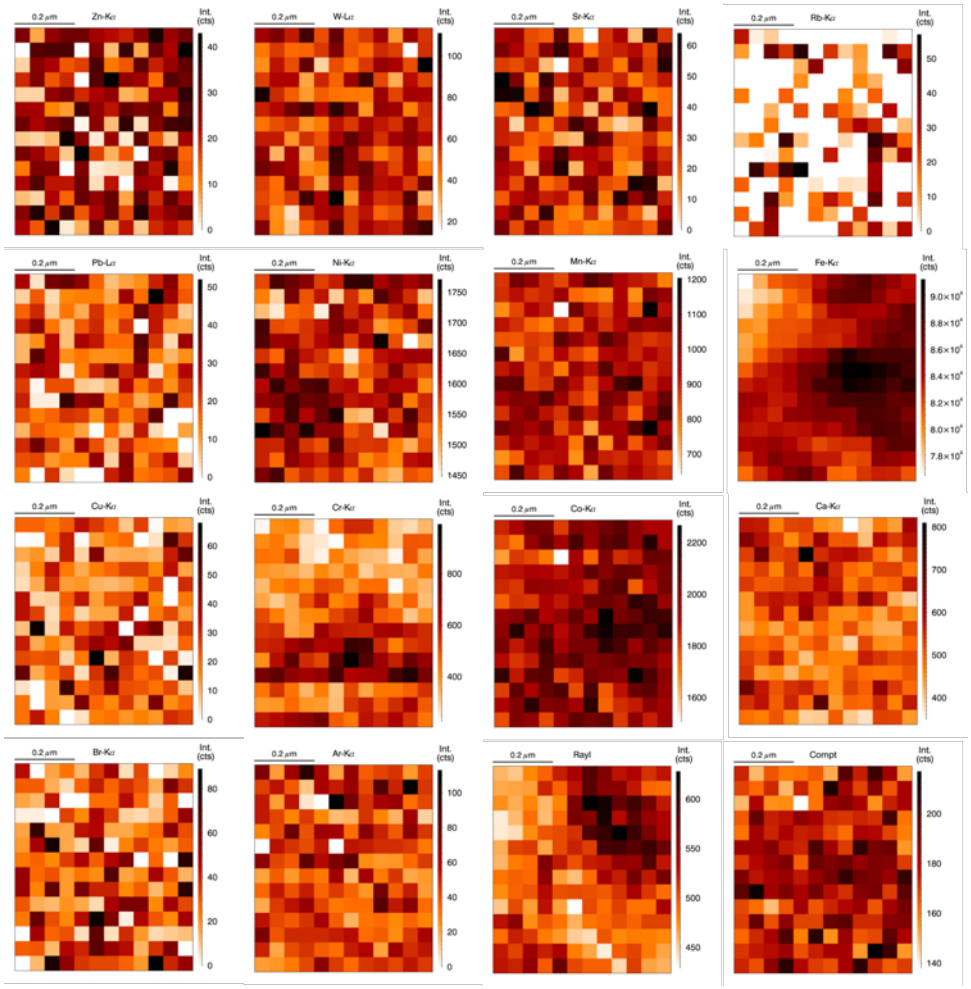

Sc4 detail 2_5

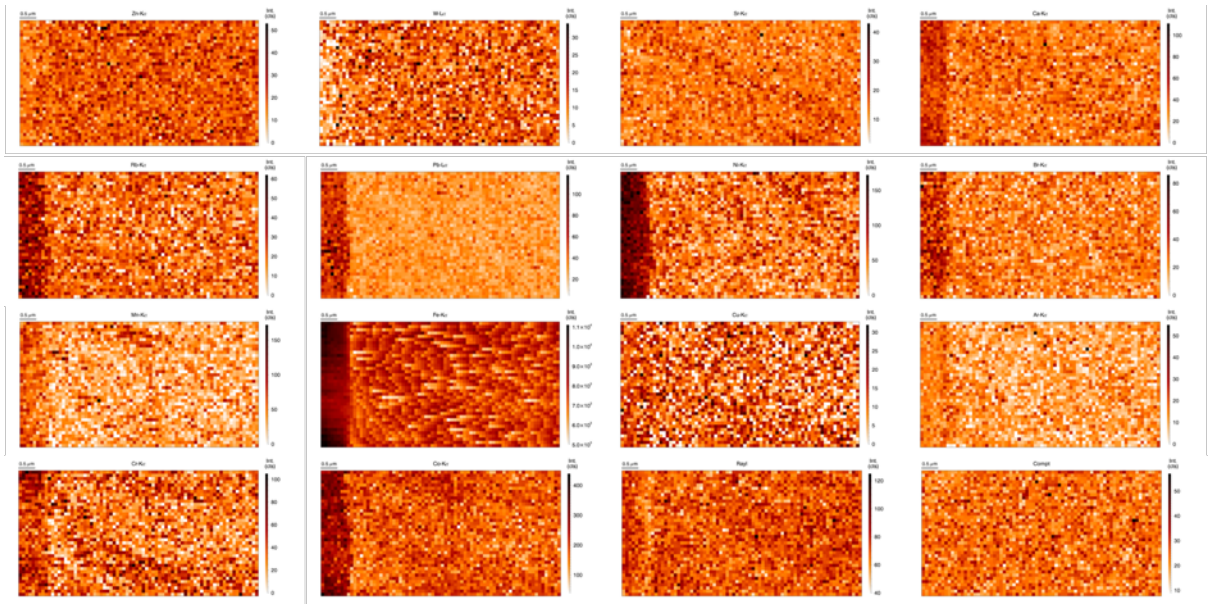

U1 overview

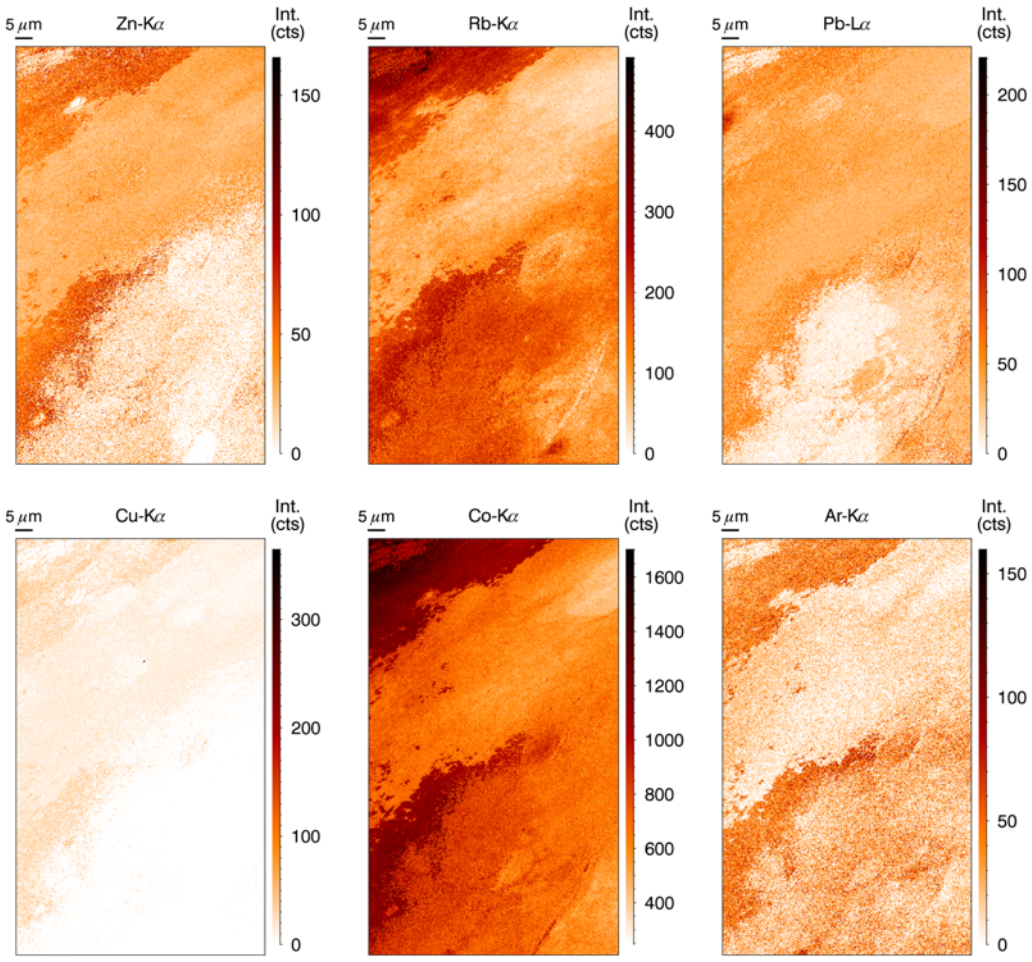
5 µm
Zn-Kα
Int. (cts)
150
100
50
0
5 µm
Rb-Kα
Int. (cts)
400
300
200
100
0
5 µm
Pb-Lα
Int. (cts)
200
150
100
50
0
5 µm
Cu-Kα
Int. (cts)
300
200
100
0
5 µm
Co-Kα
Int. (cts)
1600
1400
1200
1000
800
600
400
5 µm
Ar-Kα
Int. (cts)
150
100
50
0

U1 detail 1_2

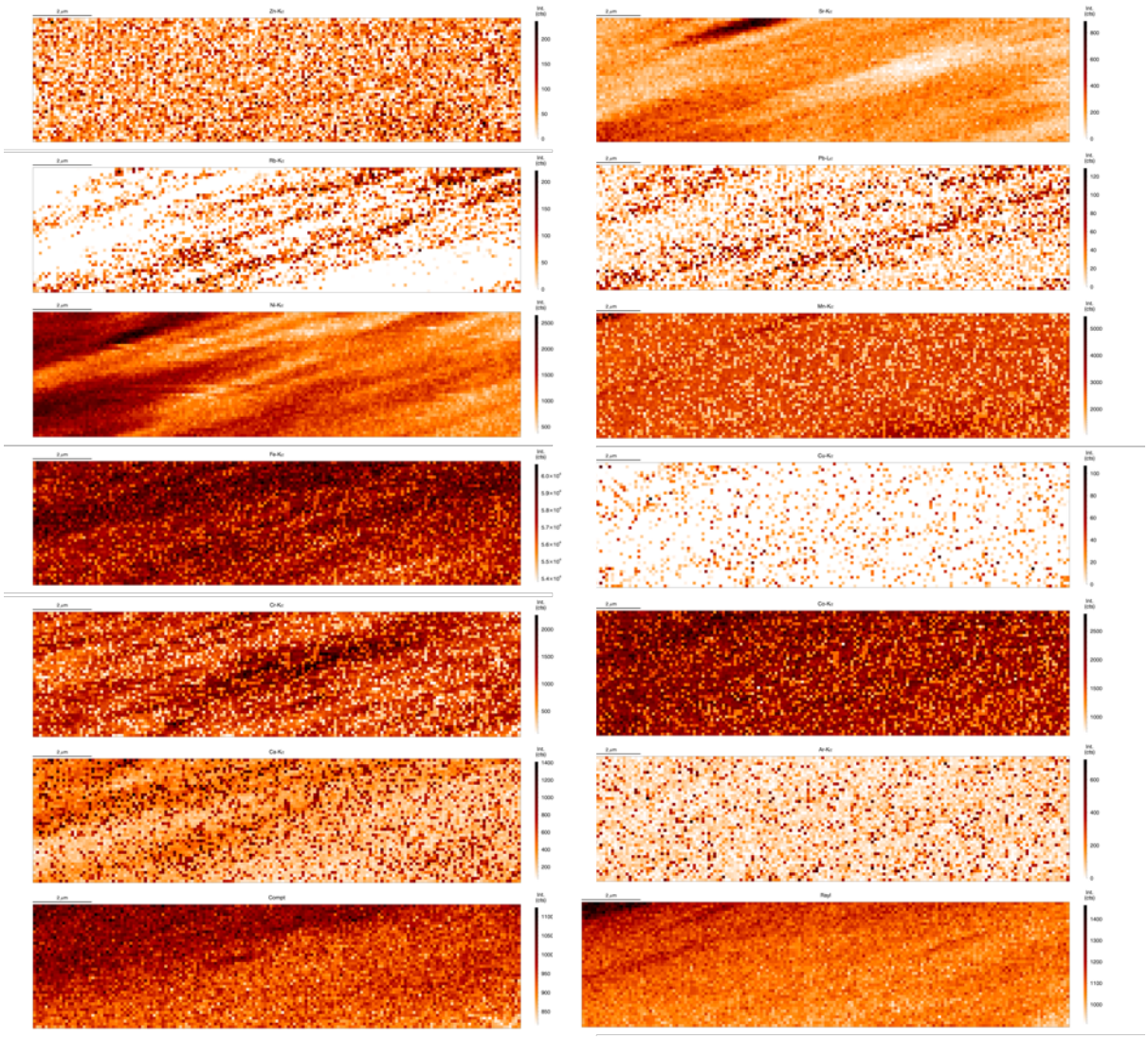

U1 detail 3_1

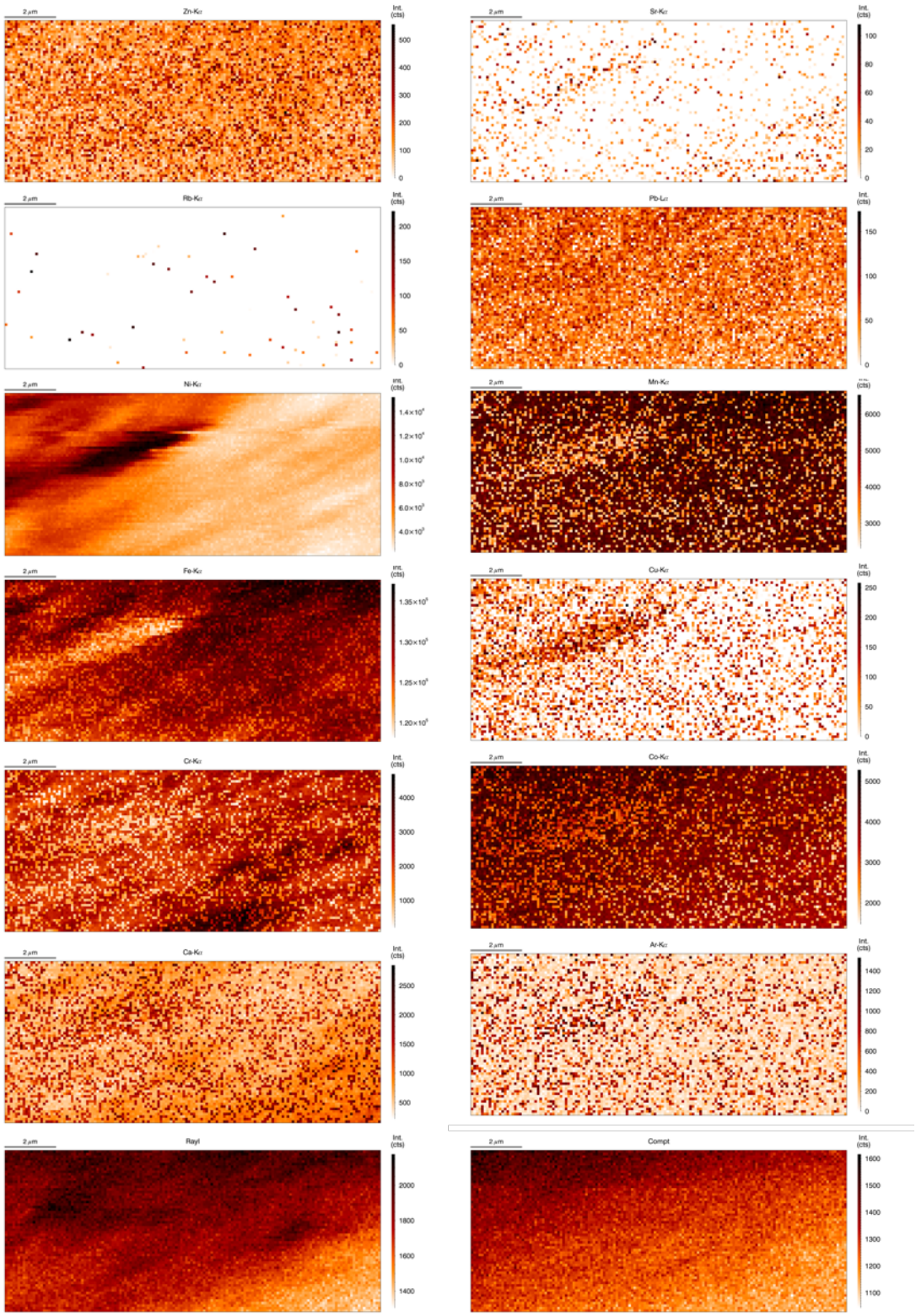
Zn-Kα
Sr-Kα
Rb-Kα
Pb-Lα
Ni-Kα
Mn-Kα
Fe-Kα
Cu-Kα
Cr-Kα
Co-Kα
Ca-Kα
Ar-Kα
Rayl
Compt

U1 detail 4_1

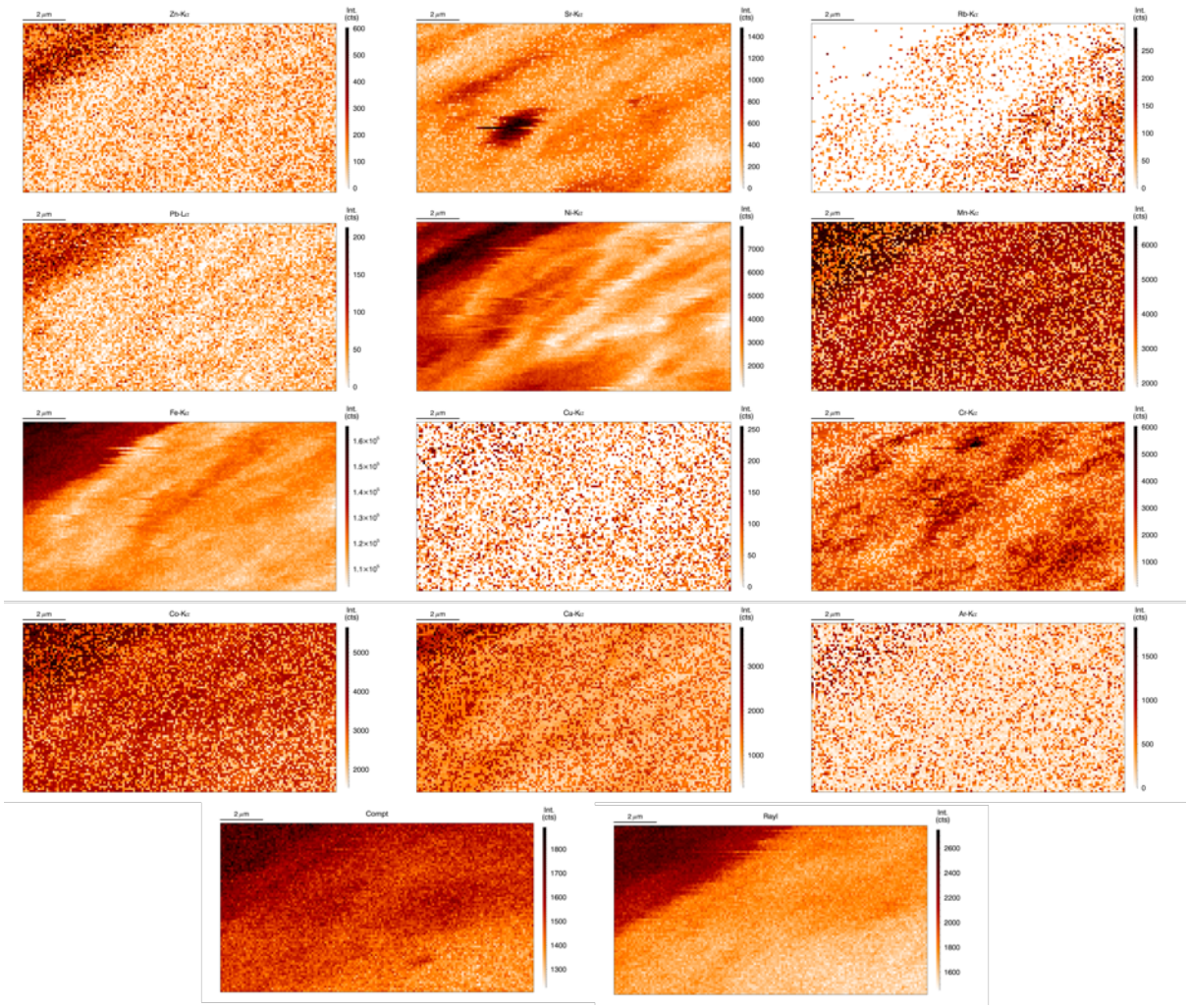

Uc2 overview

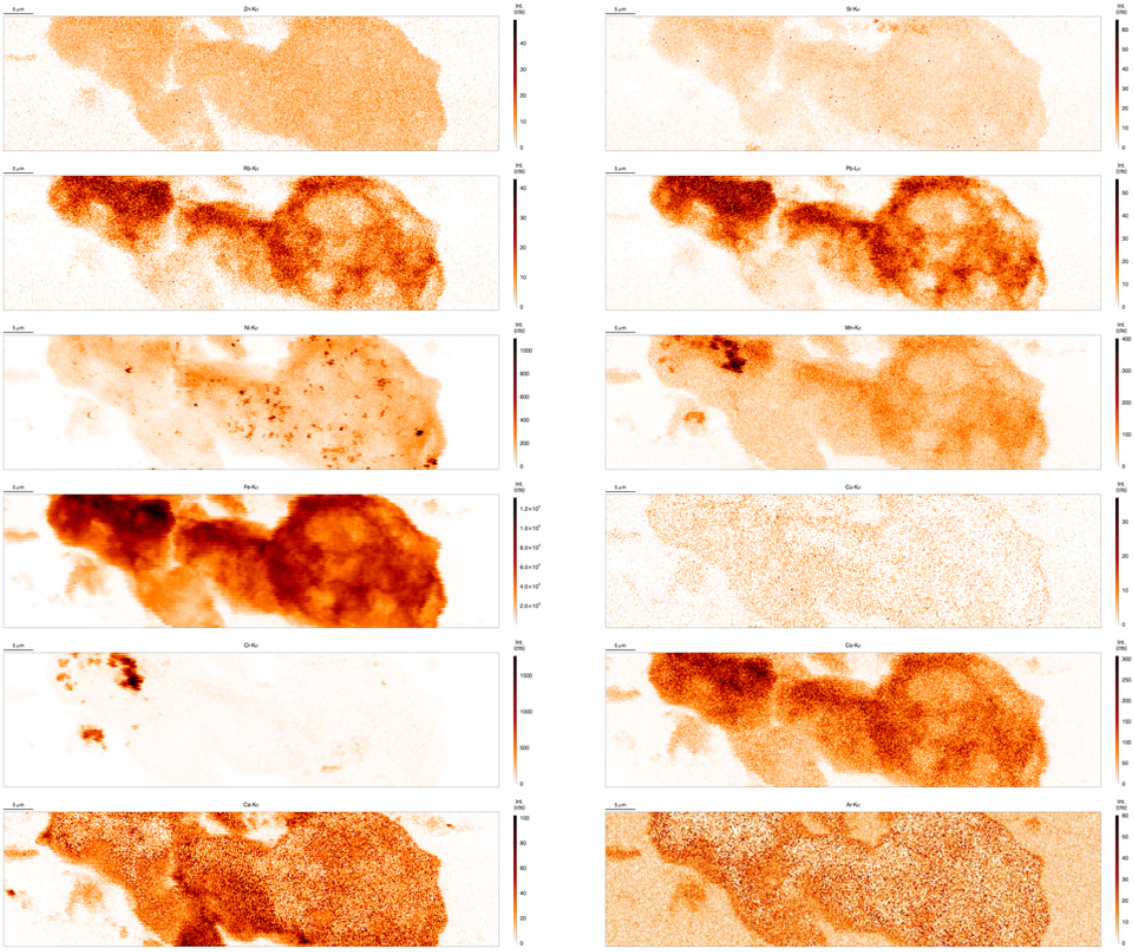

Uc3 overview

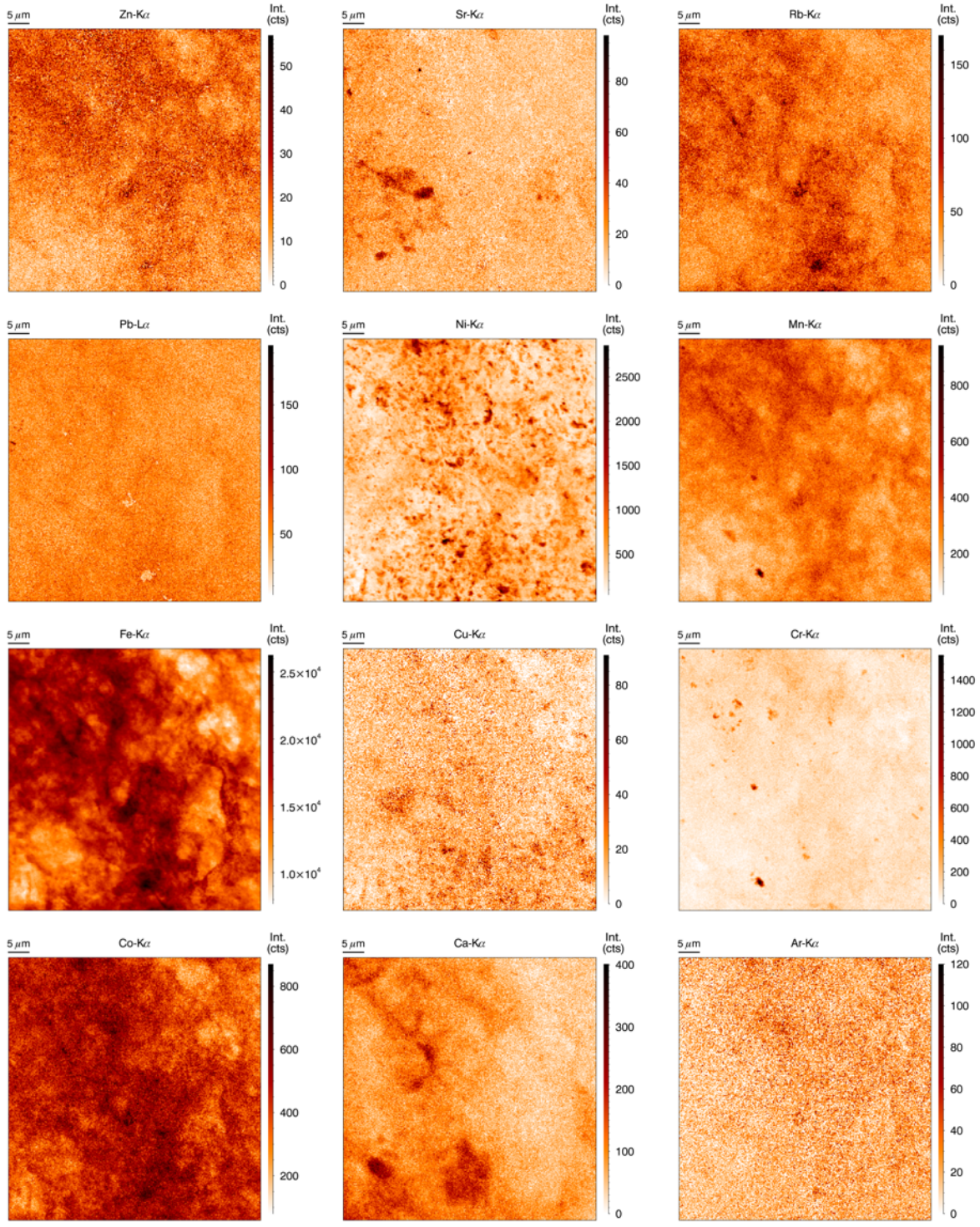

Uc3 detail d_2

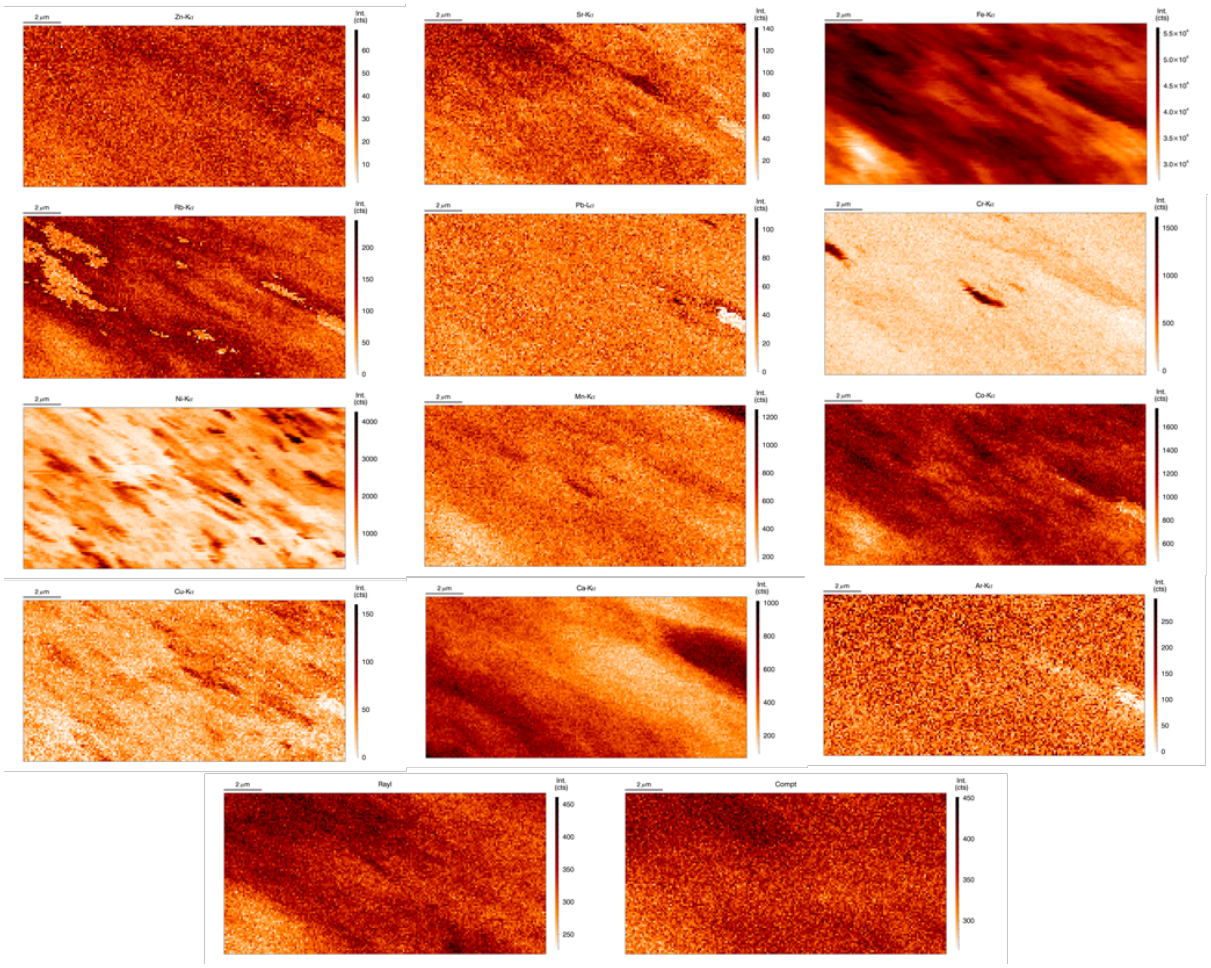

Uc3 detail d_3

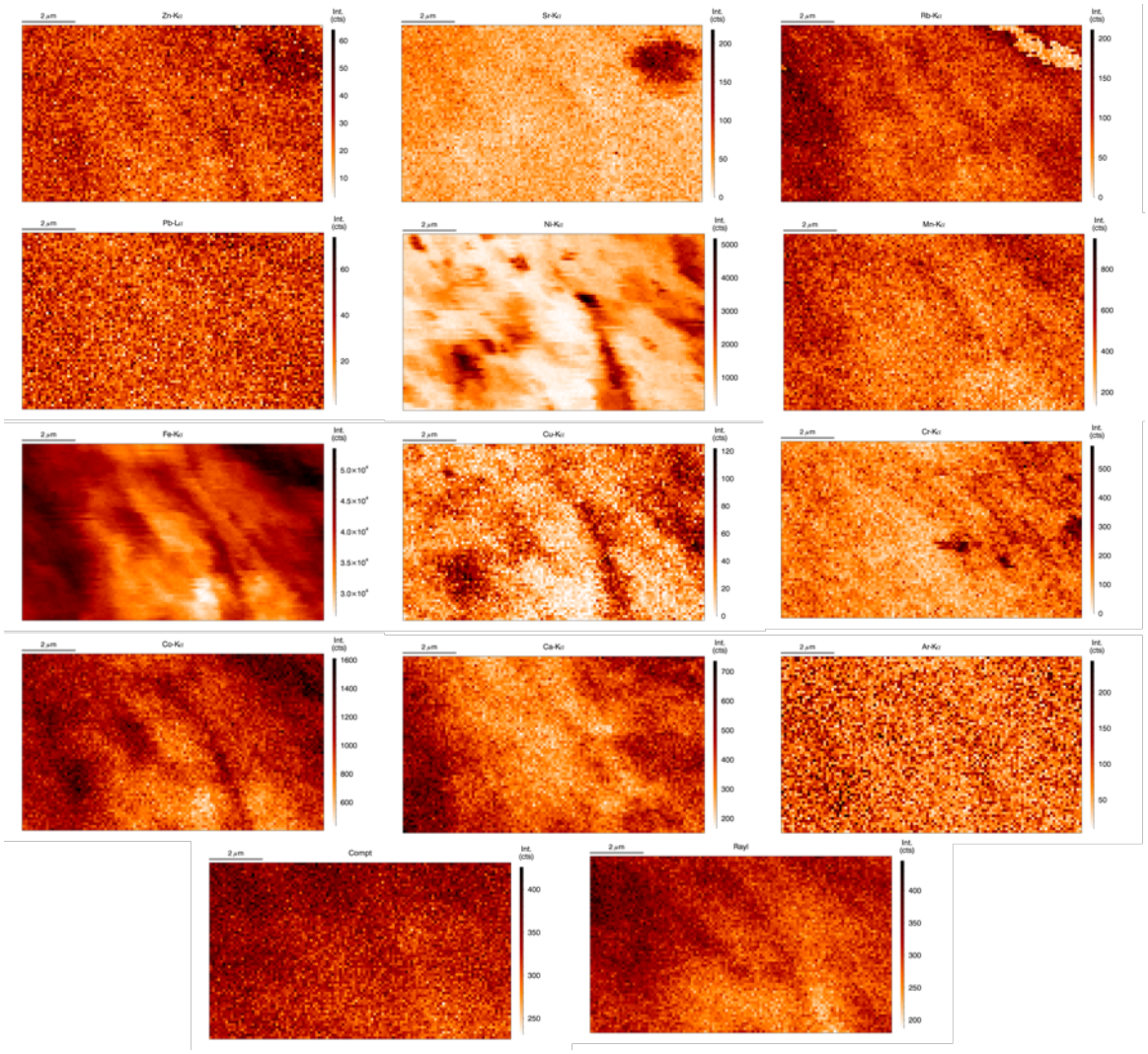

Uc3 detail d_4

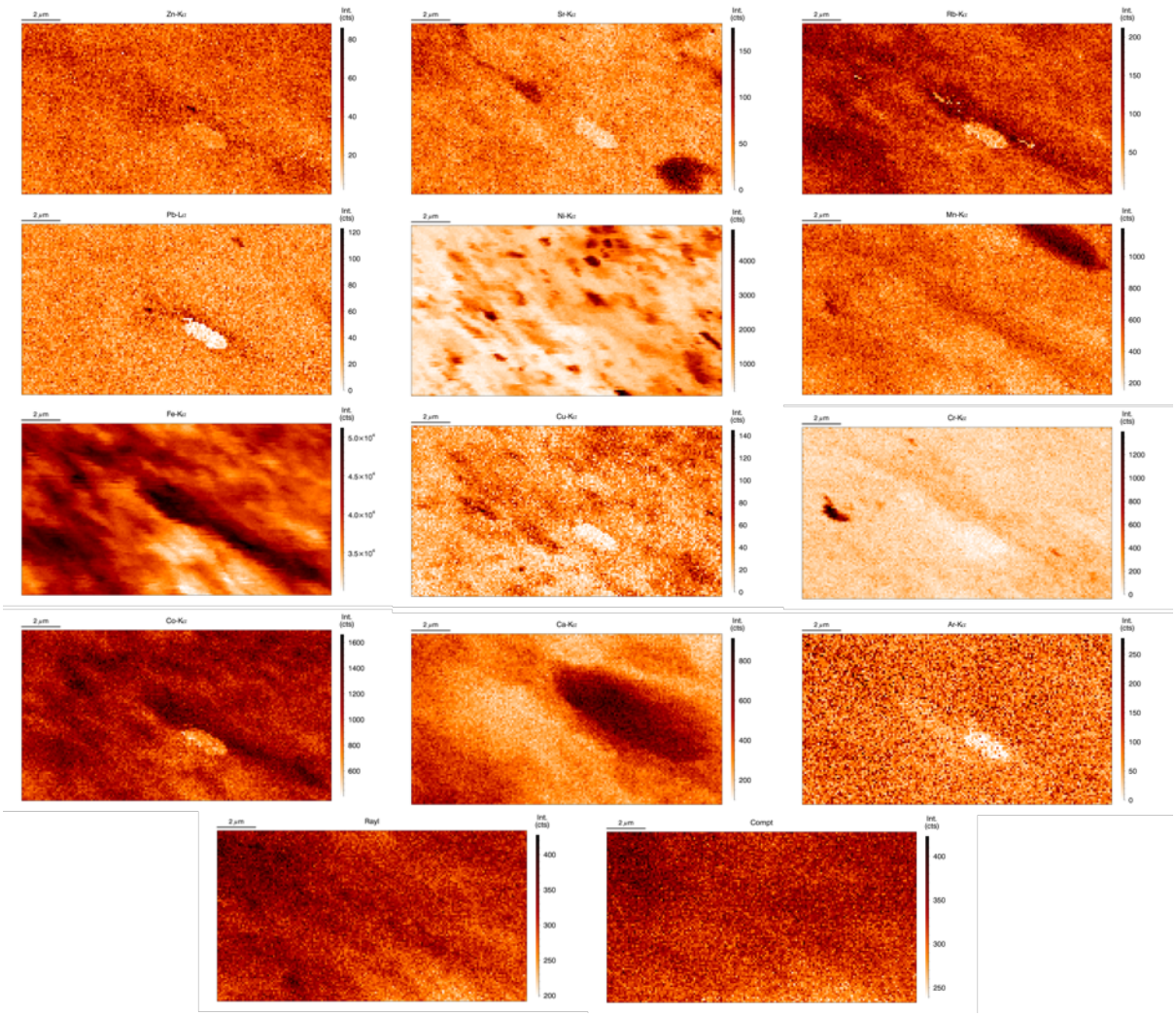

Uc3 detail d_5

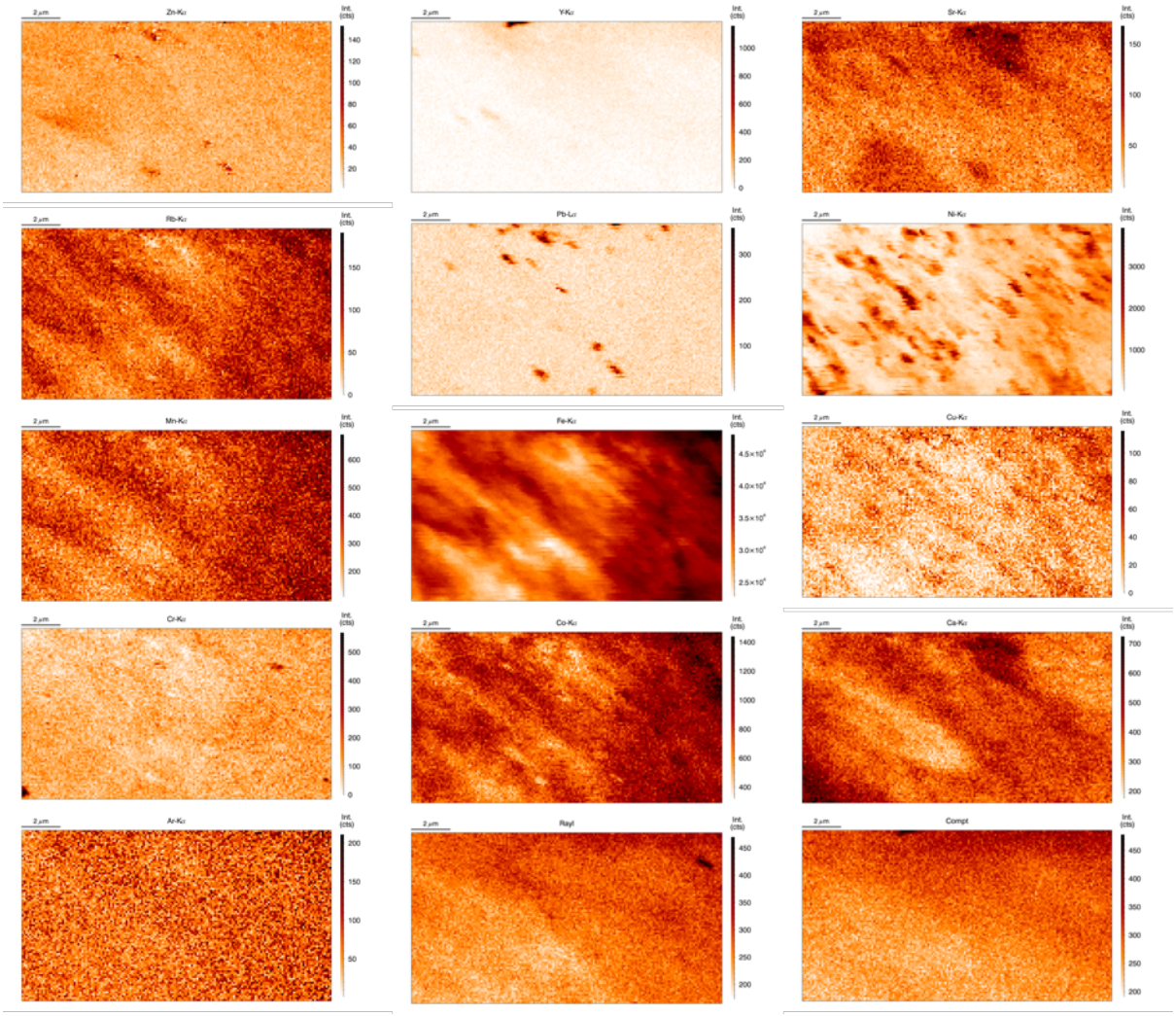

TAM1 overview

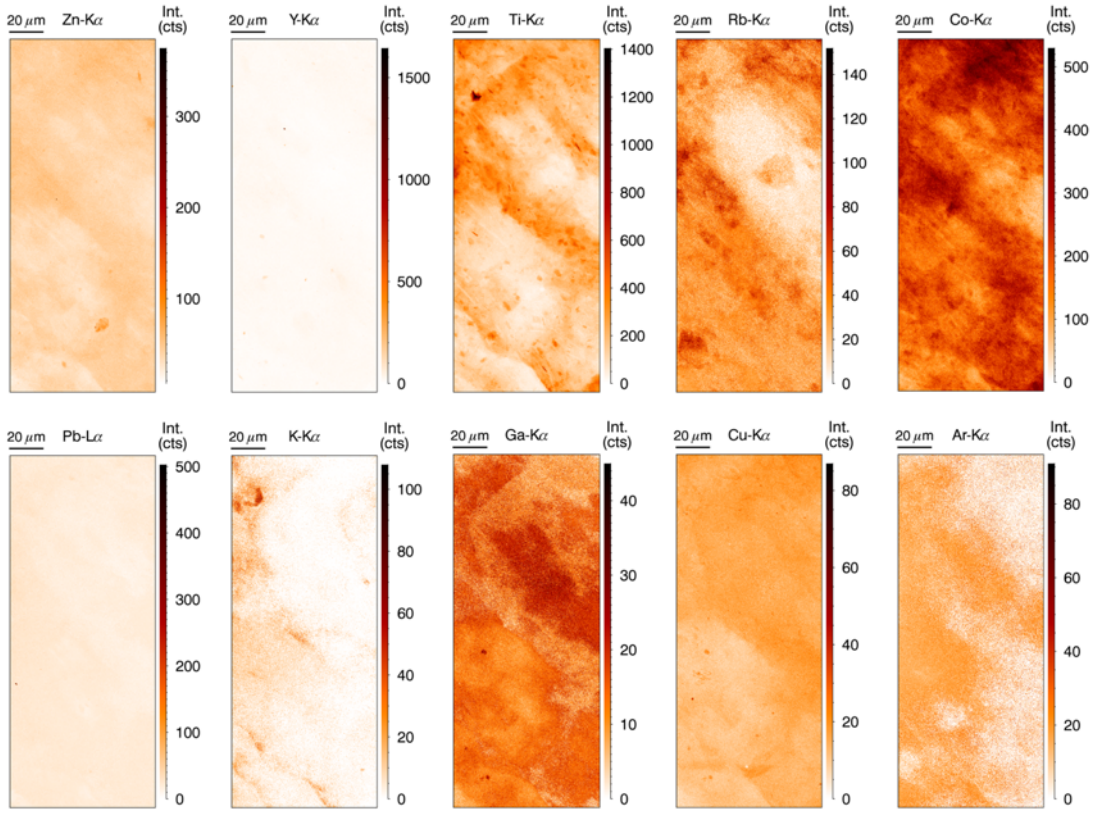

TAM2 overview

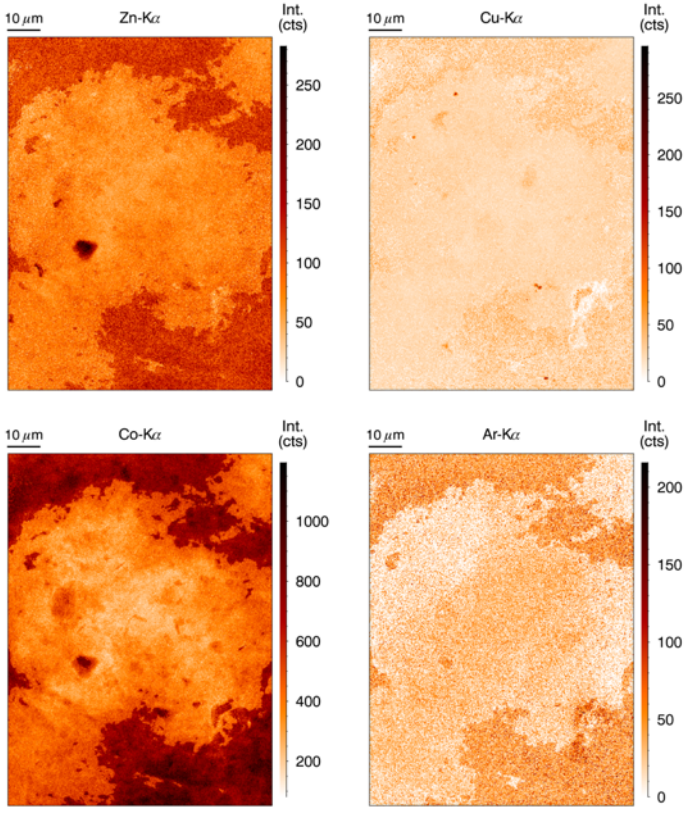

TAM2 detail d1_2

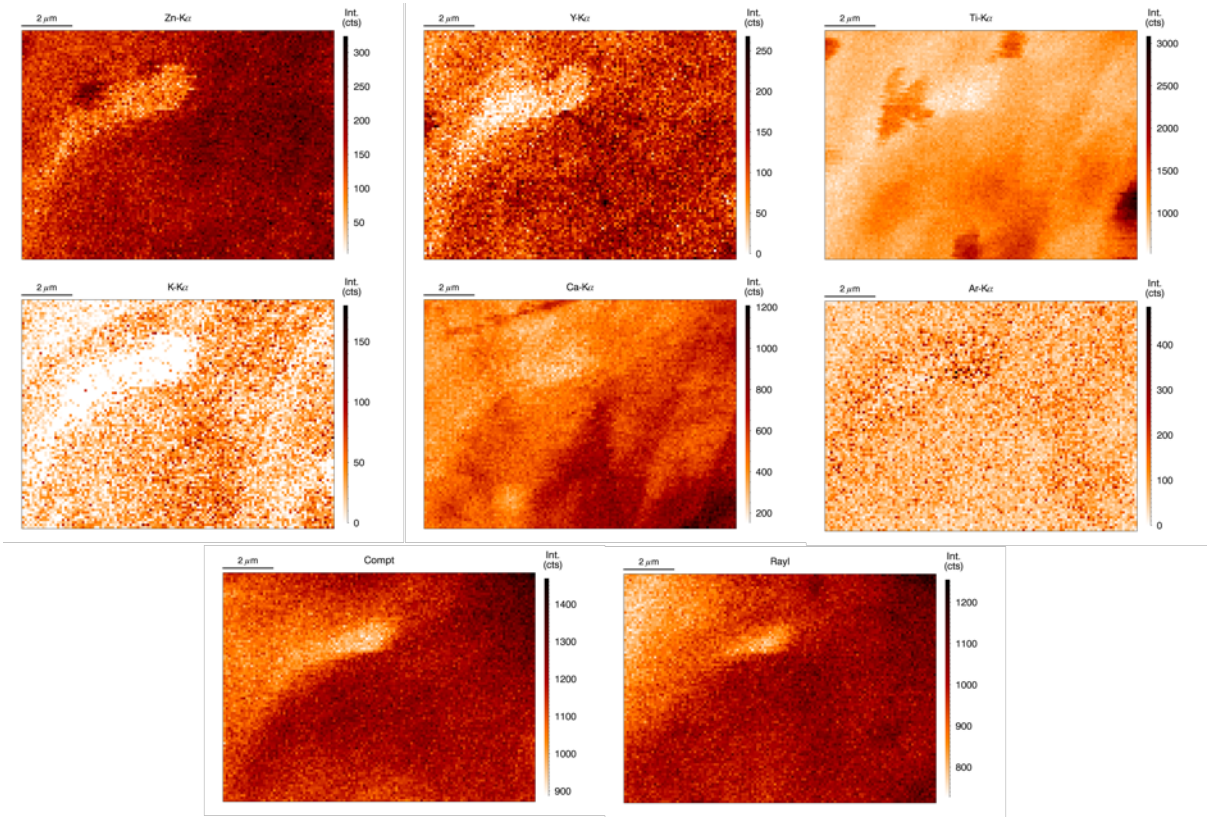

TAM2 detail d2_1

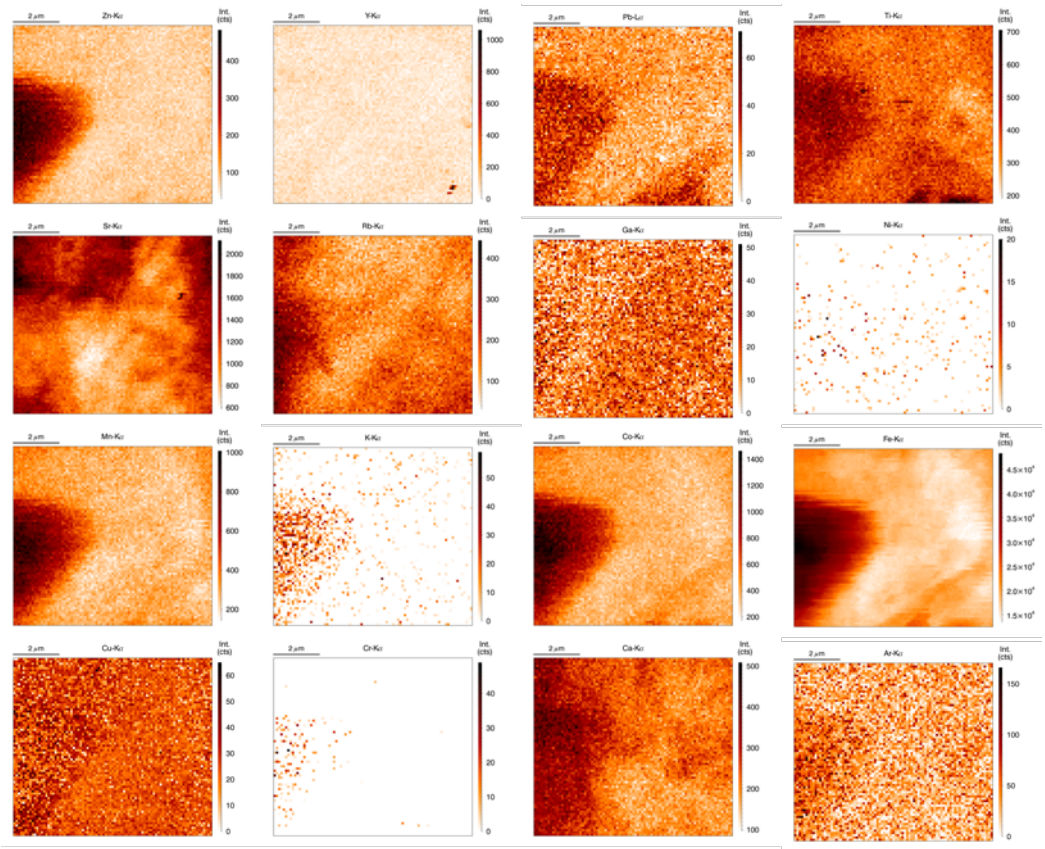

TAM2 detail d3_1